UNIVERSITY OF CALIFORNIA SAN DIEGO

Terrestrial and marine carbon cycling insights from models and measurement methods

A dissertation submitted in partial satisfaction of the requirements
for the degree Doctor of Philosophy

in

Earth Sciences

by

Julia L. Dohner

Committee in charge:

Professor Ralph F. Keeling, Chair
Professor Andreas J. Andersson
Professor Jennifer A. Burney
Professor Andrew G. Dickson
Professor Lisa A. Levin

2023

DISSERTATION APPROVAL PAGE

The Dissertation of Julia L. Dohner is approved, and it is acceptable in quality and form for publication on microfilm and electronically.

University of California San Diego

2023

DEDICATION

To my parents, for everything.

TABLE OF CONTENTS

LIST OF FIGURES

LIST OF TABLES

ACKNOWLEDGEMENTS

I am deeply grateful for the people whom I was able to learn from and work alongside during my time at Scripps. Thank you to Dr. Ralph F. Keeling, my advisor and committee chair, for your patient and empathetic mentoring and for creating an environment in which new questions are always met with eagerness and curiosity. Thank you to the members of my committee: Dr. Andreas J. Andersson, Dr. Jennifer A. Burney, Dr. Andrew G. Dickson, and Dr. Lisa A. Levin, as well as former committee member Dr. Armin Schwartzman. I feel incredibly fortunate to have access to and be mentored by scientists like you. Thank you to Dr. Tim Lueker for being so generous with your time and energy and for helping me become a more confident and mature scientist. Thank you to Dr. Benni Birner for your unfaltering support and for sharing your boundless intellect. I consider getting to work with the members of the Scripps CO_2 and O_2 groups as one of the greatest privileges of my time at Scripps. My questions have always been met with nothing but graciousness. Thank you for making the third floor of Vaughan Hall be one of the places where I am most happy.

Thank you to all the people I have encountered during my time in graduate school who have given my life such amazing texture. I have been helped through so many different challenges by so many people. With all my heart, thank you.

Chapter 1, in full, is a reprint of the material as it appears in *Global Change Biology*, 2022. Dohner, J.L., Birner, B., Schwartzman, A., Pongratz, J., and Keeling, R.F., 2022. The dissertation author was the primary investigator and author of this paper.

Thank you to the people in San Diego and Okinawa who helped make much of the work of Chapter 2 possible. To Hayashi-san, Yoshino-san, Inoha-san, and the members of the Mitarai Unit, thank you for your hospitality and patience during our field campaign in 2019. Thank you to the members of the Aluwihare lab for being so generous with your time and resources. Finally, thank you to Dr. Tim Lueker for helping with the analysis of 40+ seawater samples on the vacuum extraction line. Chapter 2 contains material currently being prepared for publication, coauthored with Andersson, A.J., Rintoul, M.S., Kekuewa, S.A., Courtney, T.A., Pezner, A.K., Mitarai, S, Page, H., Köster, I., DeCarlo, E., Nelson, C., Aluwihare, L., and Howins, N. The dissertation author was the primary researcher and author of this chapter.

Thank you to Guy Emanuele for your troubleshooting support and insights, Daniela Nestory for never hesitating to run additional alkalinity and salinity analyses, and George Anderson for ensuring I had access to the supplies I needed. A massive thank you is also owed to the members of the Scripps CO_2 and O_2 groups and Ross Beaudette for helping me past countless obstacles during the development of this method. Chapter 3 contains unpublished material coauthored with Keeling, R.F., Lueker, T.L., Paplawsky, W., Brooks, M., and Andersson, A.J. The dissertation author was the primary researcher and author of this paper.

VITA

2016 Bachelor of Arts in Chemistry, Pomona College

2017 Master of Science in Earth Sciences, University of California San Diego

2023 Doctor of Philosophy in Earth Sciences, University of California San Diego

ABSTRACT OF THE DISSERTATION

Terrestrial and marine carbon cycling insights from models and measurement methods

by

Julia L. Dohner

Doctor of Philosophy in Earth Sciences

University of California San Diego, 2023

Professor Ralph F. Keeling, Chair

Carbon in the earth system has gained immense relevance to modern society, and understanding the controls on and impacts of rising carbon dioxide (CO_2) in the atmosphere is central to humans' social well-being in the years to come. Predicting future changes requires both global-level knowledge of sources and sinks of CO_2 to the atmosphere and local-level information about individual ecosystems' responses to changes in environmental conditions thus far. This dissertation addresses three components of the greater effort to understand and predict impacts on the earth system

of rising CO_2. In the first chapter I explore whether the atmospheric CO_2 record since 1900 can be used to better estimate the source of CO_2 from land use and land cover change to the atmosphere when accounting for uncertainties in the other global sources of sinks of CO_2 (e.g., fossil fuel emissions, terrestrial and marine drawdown and release of CO_2) thus far. I show that the atmospheric CO_2 record favors land use and land cover change CO_2 flux estimates with lower decadal variability and can potentially highlight erroneous features in some published estimates. Further, this work resolves a downward correction to the land use flux mean since 1900 across 20 published estimates of 0.35 PgC $year^{-1}$ to 1.04 ± 0.57 PgC $year^{-1}$. The second chapter combines observations of seawater organic and inorganic carbon in two coral reef ecosystems to add resolution to our snapshot of coral reef ecosystems' biogeochemistry under current climatic conditions. The study presents the first inorganic carbon isotope measurements collected on a coral reef in Okinawa and finds that the reef has a community fractionation factor between -13.4 and -11 ‰ during organic matter fractionation. Finally, the third chapter presents the framework for a method to make fast and precise measurements of seawater dissolved inorganic carbon, which is one of the primary parameters used to quantify changes in the ocean stemming from marine biogeochemical processes and rising atmospheric CO_2. This chapter shows that the presented method is capable of achieving high-precision measurements and can be calibrated. The chapter also identifies possible limitations to overall measurement precision.

INTRODUCTION

The release of carbon dioxide (CO_2) into the atmosphere by human activity is increasing atmospheric CO_2 concentrations at an unprecedented rate. This rise in CO_2 has profound consequences for the climate and environmental conditions on Earth, including rising global temperatures, changes in weather patterns, rising sea levels, and changes in the makeup and functioning of ecosystems. Predicting and preparing for such changes necessitates an understanding of 1. the processes that impact atmospheric CO_2 levels, and 2. how the Earth system has responded to changes in atmospheric CO_2 thus far. This dissertation aims to contribute to the understanding of global sources and sinks of CO_2 to the atmosphere and ecosystem structure and function under current conditions.

The first chapter of this work concerns the major sources and sinks of carbon to the atmosphere, which together make up the global carbon budget. In addition to burning fossil fuels, humans have impacted atmospheric CO_2 levels through manipulation of land (e.g., clearing, conversion, and abandonment), activities which together are referred to as land use and land cover change (hereafter “land use”) (Pongratz et al., 2014). Land use adds a modest amount of CO_2 to the atmosphere annually (~1/8 of annual emissions from fossil fuel burning (Friedlingstein et al., 2022)) but made up a larger proportion of overall emissions in the 19th century and early 20th century (Houghton et al., 2012). CO_2 exchange from land use is difficult to quantify (Bastos et al., 2021), and estimates of early CO_2 fluxes have relied on an amalgamation of historical data on population and other social indices (Goldewijk et al., 2017a, 2017b).

In this work I combine estimates of atmospheric CO_2 levels, terrestrial and marine uptake of CO_2, and CO_2 emissions from fossil fuel burning to estimate the magnitude and variability of CO_2 exchange arising from land use since 1900. This work provides constraints on land use CO_2 flux estimates that are generated using process-based models and ultimately contributes to reducing uncertainty in the behavior of global sources and sinks of CO_2 to the atmosphere thus far.

The second chapter shifts to an ecosystem-based perspective of carbon cycling, using measurements of organic and inorganic carbon in seawater to understand aspects of the biogeochemistry of two coral reef ecosystems under current climatic conditions. Coral reef ecosystems play an outsized role in ocean biodiversity (Connell, 1978; Jackson, 1991) and are relied upon by communities for coastline protection and sustaining fishing and tourism economies (Ferrario et al., 2014). Coral reefs' ability to provide these ecosystem services may be hampered under climate change (Costanza et al., 2014), with changes such as rising atmospheric CO_2 and ocean temperatures expected to increase the concentration of algae inhabiting reefs and reduce that of calcium carbonate-building taxa (e.g., Agostini et al., 2018; Andersson and Gledhill, 2013). Tracking such changes requires detailed information about the current state of coral reefs' structure and function, part of which can be informed by observations of seawater carbon. This chapter combines measurements of organic and inorganic carbon in seawater in Okinawa, Japan and Hawai'i, USA to add resolution to our understanding of carbon cycling on these reefs. This information can add further detail to assessments of current ecosystem structure and function to better track any changes in coral reefs in response to rising CO_2 and ocean warming.

The final chapter of this dissertation presents the basis for a laboratory method to make high-precision measurements of dissolved inorganic carbon (DIC) in seawater. DIC is a fundamental marine parameter and is central to detecting the impacts of rising anthropogenic CO_2 on marine processes, including ocean uptake of CO_2 from the atmosphere (Peng et al., 1998) and marine metabolism (e.g., Chisholm and Gattuso, 1991; Cyronak et al., 2018). The ability to make high-precision measurements of DIC is particularly important for detecting subtle changes, such as those arising from ocean uptake of CO_2. Such changes occur on the order of tenths to a couple of μmol kg^{-1} per year (Keeling et al., 2004; Kouketsu et al., 2013), which is below the uncertainty level of many current measurement techniques (e.g., Hansen et al., 2013). Current techniques may limit our ability to detect yet-examined finer-scale variations arising from natural or anthropogenic changes. Finally, improved analytical precision may improve calibration and diagnosis of systematic errors in other measurement methods. I present a continuous flow-through DIC measurement method that is shown to be able to be calibrated and achieve a high level of precision. Though the system currently achieves a repeatability of 2.5 ‰ (equivalent to ± 5 μmol kg^{-1} for a sample with 2000 μmol kg^{-1} DIC), I show that under optimal conditions it can make measurements with a repeatability of 0.16 ‰. Issues currently limiting the performance of the measurement system, which include liquid and gas handling stability and CO_2 retention in polymeric materials, are identified and discussed with possible solutions.

The work of this dissertation is motivated by the fundamental importance of carbon cycling on this planet to humans' social well-being. Predicting and preparing for future environmental conditions requires accurate and abundant information about how

the earth system has and is responding to changes in atmospheric CO_2 levels. This information is acquired through the amalgamation of methods and efforts to understand global carbon cycling at different scales. This dissertation presents three such efforts.

References

Agostini, S., Harvey, B. P., Wada, S., Kon, K., Milazzo, M., Inaba, K. and Hall-Spencer, J. M.: Ocean acidification drives community shifts towards simplified non-calcified habitats in a subtropical−temperate transition zone, Sci. Rep., 8(1), 1–11, doi:10.1038/s41598-018-29251-7, 2018.

Andersson, A. J. and Gledhill, D.: Ocean acidification and coral reefs: effects on breakdown, dissolution, and net ecosystem calcification, Ann. Rev. Mar. Sci., 5, 321–348, 2013.

Bastos, A., Hartung, K., Nützel, T. B., Nabel, J. E. M. S., Houghton, R. A. and Pongratz, J.: Comparison of uncertainties in land-use change fluxes from bookkeeping model parameterization, Earth Syst. Dyn. Discuss., 1–24, 2021.

Chisholm, J. R. M. and Gattuso, J.-P.: Validation of the alkalinity anomaly technique for investigating calcification of photosynthesis in coral reef communities, Limnol. Oceanogr., 36(6), 1232–1239, 1991.

Connell, J. H.: Diversity in tropical rain forests and coral reefs: high diversity of trees and corals is maintained only in a nonequilibrium state., Science (80-.)., 199(4335), 1302–1310, 1978.

Costanza, R., de Groot, R., Sutton, P., der Ploeg, S., Anderson, S. J., Kubiszewski, I., Farber, S. and Turner, R. K.: Changes in the global value of ecosystem services, Glob. Environ. Chang., 26, 152–158, 2014.

Cyronak, T., Andersson, A. J., Langdon, C., Albright, R., Bates, N. R., Caldeira, K., Carlton, R., Corredor, J. E., Dunbar, R. B., Enochs, I., Erez, J., Eyre, B. D., Gattuso, J.-P., Gledhill, D., Kayanne, H., Kline, D. I., Koweek, D. A., Lantz, C., Lazar, B., Manzello, D., McMahon, A., Meléndez, M., Page, H. N., Santos, I. R., Schulz, K. G., Shaw, E., Silverman, J., Suzuki, A., Teneva, L., Watanabe, A. and Yamamoto, S.: Taking the metabolic pulse of the world's coral reefs, edited by C. R. Voolstra, PLoS One, 13(1), e0190872, doi:10.1371/journal.pone.0190872, 2018.

Ferrario, F., Beck, M. W., Storlazzi, C. D., Micheli, F., Shepard, C. C. and Airoldi, L.: The effectiveness of coral reefs for coastal hazard risk reduction and adaptation, Nat. Commun., 5, 3794, 2014.

Friedlingstein, P., Jones, M. W., O'Sullivan, M., Andrew, R. M., Bakker, D. C. E., Hauck, J., Le Quéré, C., Peters, G. P., Peters, W., Pongratz, J., Sitch, S., Canadell, J. G., Ciais, P., Jackson, R. B., Alin, S. R., Anthoni, P., Bates, N. R., Becker, M., Bellouin, N., Bopp, L., Chau, T. T. T., Chevallier, F., Chini, L. P., Cronin, M., Currie, K. I., Decharme, B., Djeutchouang, L. M., Dou, X., Evans, W., Feely, R. A., Feng, L., Gasser, T., Gilfillan, D., Gkritzalis, T., Grassi, G., Gregor, L., Gruber, N., Gürses, Ö., Harris, I., Houghton, R. A., Hurtt, G. C., Iida, Y., Ilyina, T., Luijkx, I. T., Jain, A., Jones, S. D., Kato, E., Kennedy, D., Goldewijk, K. K., Knauer, J., Korsbakken, J. I., Körtzinger, A., Landschützer, P., Lauvset, S. K., Lefèvre, N., Lienert, S., Liu, J., Marland, G., McGuire, P. C., Melton, J. R., Munro, D. R., Nabel, J. E. M. S., Nakaoka, S. I., Niwa, Y., Ono, T., Pierrot, D., Poulter, B., Rehder, G., Resplandy, L., Robertson, E., Rödenbeck, C., Rosan, T. M., Schwinger, J., Schwingshackl, C., Séférian, R., Sutton, A. J., Sweeney, C., Tanhua, T., Tans, P. P., Tian, H., Tilbrook, B., Tubiello, F., Van Der Werf, G. R., Vuichard, N., Wada, C., Wanninkhof, R., Watson, A. J., Willis, D., Wiltshire, A. J., Yuan, W., Yue, C., Yue, X., Zaehle, S. and Zeng, J.: Global Carbon Budget 2021, Earth Syst. Sci. Data, 14(4), 1917–2005, doi:10.5194/essd-14-1917-2022, 2022.

Goldewijk, K. K., Beusen, A., Doelman, J. and Stehfest, E.: Anthropogenic land use estimates for the Holocene--HYDE 3.2, Earth Syst. Sci. Data, 9(1), 927–953, 2017a.

Goldewijk, K. K., Dekker, S. C. and van Zanden, J. L.: Per-capita estimations of long-term historical land use and the consequences for global change research, J. Land Use Sci., 12(5), 313–337, 2017b.

Hansen, T., Gardeler, B. and Matthiessen, B.: Precise quantitative measurements of total dissolved inorganic carbon from small amounts of seawater using a gas chromatographic system, Biogeosciences, 10(10), 6601–6608, 2013.

Houghton, R. A., House, J. I., Pongratz, J., Van Der Werf, G. R., Defries, R. S., Hansen, M. C., Le Quéré, C. and Ramankutty, N.: Carbon emissions from land use and land-cover change, Biogeosciences, 9(12), 5125–5142, doi:10.5194/bg-9-5125-2012, 2012.

Jackson, J. B. C.: Adaptation and diversity of reef corals, Bioscience, 475–482, 1991.

Keeling, C. D., Brix, H. and Gruber, N.: Seasonal and long-term dynamics of the upper ocean carbon cycle at Station ALOHA near Hawaii, Global Biogeochem. Cycles, 18(4), 2004.

Kouketsu, S., Murata, A. and Doi, T.: Decadal changes in dissolved inorganic carbon in the Pacific Ocean, Global Biogeochem. Cycles, 27(1), 65–76, doi:10.1029/2012GB004413, 2013.

Peng, T. H., Wanninkhof, R., Bullister, J. L., Feely, R. A. and Takahashi, T.: Quantification of decadal anthropogenic CO2 uptake in the ocean based on dissolved inorganic carbon measurements, Nature, 396(6711), 560–563, doi:10.1038/25103, 1998.

Pongratz, J., Reick, C. H., Houghton, R. A. and House, J. I.: Terminology as a key uncertainty in net land use and land cover change carbon flux estimates, Earth Syst. Dyn., 5(1), 177–195, 2014.

CHAPTER 1: Using the atmospheric CO_2 growth rate to constrain the CO_2 flux from land use and land cover change since 1900

Dohner, J.L., Birner, B., Schwartzman, A., Pongratz, J., Keeling, R.F.

Received: 2 March 2022 | Accepted: 18 July 2022

DOI: 10.1111/gcb.16396

Global Change Biology WILEY

RESEARCH ARTICLE

Using the atmospheric CO_2 growth rate to constrain the CO_2 flux from land use and land cover change since 1900

Julia L. Dohner[1] | Benjamin Birner[1] | Armin Schwartzman[2,3] | Julia Pongratz[4,5] | Ralph F. Keeling[1]

[1]Scripps Institution of Oceanography, University of California, San Diego, California, USA

[2]Division of Biostatistics, University of California, San Diego, California, USA

[3]Halıcıoğlu Data Science Institute, University of California, San Diego, California, USA

[4]Department of Geography, Ludwig-Maximilians Universität, München, Germany

[5]Max Planck Institute for Meteorology, Hamburg, Germany

Correspondence
Julia L. Dohner, Scripps Institution of Oceanography, University of California, San Diego, CA, USA.
Email: jdohner@ucsd.edu

Funding information
Eric and Wendy Schmidt, Grant/Award Number: Schmidt Futures; National Aeronautics and Space Administration, Grant/Award Number: NNX17AE74G; National Science Foundation, Grant/Award Number: Graduate Research Fellowship Program

Abstract

We explore the ability of the atmospheric CO_2 record since 1900 to constrain the source of CO_2 from land use and land cover change (hereafter "land use"), taking account of uncertainties in other terms in the global carbon budget. We find that the atmospheric constraint favors land use CO_2 flux estimates with lower decadal variability and can identify potentially erroneous features, such as emission peaks around 1960 and after 2000, in some published estimates. Furthermore, we resolve an offset in the global carbon budget that is most plausibly attributed to the land use flux. This correction shifts the mean land use flux since 1900 across 20 published estimates down by 0.35 PgC year^{-1} to 1.04 ± 0.57 PgC year^{-1}, which is within the range but at the low end of these estimates. We show that the atmospheric CO_2 record can provide insights into the time history of the land use flux that may reduce uncertainty in this term and improve current understanding and projections of the global carbon cycle.

KEYWORDS
atmospheric CO_2, CO_2 growth rate, global carbon budget, global CO_2 fluxes, land use change, terrestrial CO_2 sink

1 | INTRODUCTION

The increase in atmospheric CO_2 since the turn of the 19th century has been driven by anthropogenic emissions from fossil fuel burning and industry (FF, hereafter "fossil emissions") and emissions and removals from land use change (LU, hereafter "land use flux"), including land management and related land cover changes (Friedlingstein et al., 2020). These emissions are offset by natural uptake of CO_2 by the terrestrial biosphere (*B*, hereafter referred to as the "terrestrial sink," for which "natural" is implied) and the ocean (*O*) (Broecker et al., 1979; Siegenthaler & Sarmiento, 1993). The balance of these sources and sinks determines the magnitude of the atmospheric growth rate (AGR):

$$\mathrm{AGR} = \mathrm{FF} + \mathrm{LU} - O - B \quad (1)$$

where all fluxes are in units of PgC year^{-1}, and positive values for each term indicate increasing strength of their source (FF, LU) or sink (*O*, *B*).

The atmospheric CO_2 growth rate is well known from contemporary observations and historical reconstructions (Conway &

Tans, 2009; Keeling et al., 2005; MacFarling Meure et al., 2006). As the best estimated term of Equation (1), the growth rate has been used to constrain the combined land and ocean sinks, treating fossil emissions and land use flux as known (Ballantyne et al., 2012; Joos et al., 1999). This process has also been reversed and used to verify fossil emissions (Francey et al., 2010; Peters et al., 2017). The terrestrial sink (B) has commonly been calculated as a residual (B_{res}, referred to as the "residual terrestrial sink") of the other terms of Equation (1) (Le Quéré et al., 2016). Finally, the AGR has also been used to quantify the land use flux occurring in the 19th century, a time when fossil emissions were small and growing atmospheric CO_2 levels supported the existence of significant emissions from land use (Siegenthaler & Oeschger, 1987; Wilson, 1978; Woodwell et al., 1983). However, the growth rate has not been previously used to constrain the land use flux in the 20th century and later.

The land use flux has been estimated using bookkeeping methods and dynamic global vegetation models (DGVMs) (Figure 1). The bookkeeping approach uses vegetation and soil carbon densities to estimate the flow of carbon between the land and atmosphere in response to inferred and historical occurrences of land use activities. DGVMs simulate effects of both natural and anthropogenic processes (including land use) on terrestrial carbon stocks and compare simulations with and without land use activity to calculate the land use CO_2 flux. At present, estimates of the land use flux vary substantially in magnitude and variability across models, and the flux is overall considered to be uncertain by ~50% (Friedlingstein et al., 2020).

The estimates of the land use flux vary widely across models related to differences in (i) underlying land use reconstructions, (ii) the degree of implementation of land use practices, (iii) definitions of the land use flux, and (iv) modeling parameterizations and process representation (Pongratz et al., 2018): (i) The source and implementation of information on changes in agricultural areas and forest management differ across studies (Friedlingstein et al., 2022) and substantially influence land use flux estimates (Gasser et al., 2020), as does uncertainty in the land use reconstructions themselves (Hartung et al., 2021). (ii) Land use practices (e.g., drainage, shifting cultivation, wood harvest) are implemented by the models to different extents (Arneth et al., 2017) and with varying complexity (Pongratz et al., 2018). (iii) DGVMs typically include synergistic effects between natural environmental changes and land use change in their land use flux estimates, while bookkeeping approaches leave them out (Gasser et al., 2020; Obermeier et al., 2021; Pongratz et al., 2014). (iv) Model parameterizations are often not well constrained by observational data, such that, for example, carbon densities differ substantially across bookkeeping models (Bastos et al., 2021); furthermore, the details of processes underlying a realistic land use description, such as vegetation demography, differ widely across DGVMs (Fisher et al., 2018). These model aspects continue to be improved (Blyth et al., 2021; Pongratz et al., 2018) and observations of proxies relevant to land use emissions, such as fires (van Marle et al., 2022), biomass changes (Xu et al., 2021), or forest loss (Feng et al., 2022) increasingly provide additional ways to evaluate the size and evolution at least of certain components of the land use flux. The AGR could provide an additional top-down, independent constraint on the plausibility of the complete land use flux.

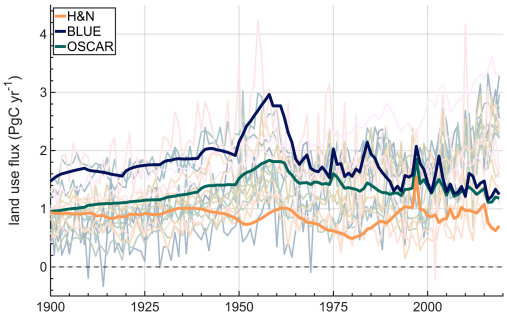

FIGURE 1 Estimates of land use flux via bookkeeping based (H&N, BLUE, OSCAR, in bold) and DGVM-based (17 estimates shown here faintly and separately in Figure S1; see Table S1 for references), all shown at annual resolution. We use the color map batlow (Crameri, 2021) in this study to prevent visual distortion of the data and to make this work accessible to readers with differing color vision (Crameri et al., 2020).

The land use flux has been difficult to characterize and is a primary source of uncertainty in global anthropogenic fluxes of CO_2 (Riahi et al., 2022). Current estimates of land use fluxes have means over 1900–2019 ranging from 0.76 (Vuichard et al., 2019) to 2.15 PgC year^{-1} (Yue & Unger, 2015), with Friedlingstein et al. (2022) reporting an average annual flux of 1.32 ± 0.7 PgC year^{-1} since 1900. Booth et al. (2017) show that reducing uncertainty in the land use flux can substantially narrow the range in projected future climate scenarios, which hinge on models tuned to match past fluxes. Additional constraints are needed to refine estimates of the land use flux and improve projections of the carbon cycle.

Here we examine whether the atmospheric CO_2 growth rate in Equation (1) can be used to constrain the land use flux since 1900. Recognizing that the overall uncertainty in the global carbon budget complicates analysis of land use fluxes on timescales shorter than decadal, we examine to what extent variations in the atmospheric CO_2 growth rate constrain the magnitude of decade-to-decade variability in the land use flux. We address this question by evaluating the compatibility of published estimates of the land use flux with the other terms in Equation (1) via linear regression fits. We examine the distributions of scalars and error in these fits to draw inferences about deficiencies in the prior estimates of the land use flux. In total, we find that the CO_2 growth rate favors land use flux estimates with lower decadal variability, and also find that the budget requires an additive adjustment, which we argue is most plausibly attributed to the land use flux.

2 | METHODS

2.1 | Model optimization

To evaluate the compatibility of various land use flux reconstructions (LU_j) with the AGR, we employ Equation (1) as a linear regression:

TABLE 1 Expressions for generating temporally autocorrelated noise to account for uncertainty in the model inputs CO_2 (atmospheric CO_2 record, used to calculate AGR), FF, and O

Term	AR1	AR2	σ	Source
CO_2	0.244	0.086	0.51 PgC	Ballantyne et al. (2012)
FF	0.95	-	5%	Ballantyne et al. (2015)
O	0.9	-	0.4 PgC year^{-1}	Anderegg et al. (2015)

Note: The standard deviation of the generated noise time series is normalized to match published values (σ). Noise in FF is scaled at each yearly value to a standard deviation of 5% of the emissions in that year.

$$\mathrm{AGR} + O - \mathrm{FF} = \mathrm{LU}_j + \alpha - \beta \cdot B_k + \mathrm{error} \quad (2)$$

where subscripts j and k refer to prior estimates of the land use flux and terrestrial sink, respectively, as compiled by the Global Carbon Project (Friedlingstein et al., 2020), and AGR, O, and FF are composite best estimates (Friedlingstein et al., 2020), with noise added, as discussed in Section 2.3. The parameters α and β are scalars fitted to minimize the mean squared error (MSE):

$$\mathrm{MSE} = \frac{1}{(t_1 - t_0) + 1} \sum_{t_0}^{t_1} \left(\overline{\mathrm{error}(t)}\right)^2 \quad (3)$$

where $\overline{\mathrm{error}}$ denotes the error smoothed with a 10-year moving average, and the MSE is calculated over the fitting period in which t_0 is either 1900 or 1959 and t_1 is 2019. The 1900 start was chosen, as opposed to, for example, 1800, to avoid the need to taper the fitted constant α (all terms in the budget were zero prior to the industrial revolution). The 1959 start was chosen to restrict the analysis to the period of direct atmospheric measurements (as opposed to including ice core measurements). The decadal smoothing ensures that emphasis is placed on the decadal and longer timescales that are resolved in the land use flux reconstructions. The decadal smoothing also has the effect of smoothing discontinuities and changes in interannual variability in datasets due to changes in sampling methodology (e.g., atmospheric CO_2 data). The optimized values for α and β depend on the selected prior estimates for the input terms, including LU and B (i.e., $\alpha = \alpha_{jk}$, $\beta = \beta_{jk}$). Below, we report the error alternately as MSE or as the root mean squared error (RMSE = $\sqrt{\mathrm{MSE}}$).

2.2 | Data description

We select LU_j from 20 published land use flux inputs and one hypothetical case of a constant LU. These include three bookkeeping-based estimates from Houghton and Nassikas (2017) (hereafter H&N), the Bookkeeping Land Use Emissions model (BLUE) (Hansis et al., 2015), and OSCAR (Gasser et al., 2020) (all in the updated versions as reported in Friedlingstein et al. (2022)), and 17 DGVM estimates included in Friedlingstein et al. (2020). We also explore a case in which the land use flux is held constant (CONST) over the entire 1900–2019 period, which is equivalent to setting $\mathrm{LU}_j = 0$ because Equation (2) already contains the additive constant α.

For the terrestrial CO_2 sink, we select B_k from 17 DGVM estimates included in Friedlingstein et al. (2020). For the atmospheric CO_2 growth rate, we calculate the growth rate from the monthly atmospheric CO_2 record compiled by Joos and Spahni (2008, updated), which combines atmospheric data from the NOAA/ESRL global network (1980–2019) and Mauna Loa, Hawaii (1958–1979), and ice core data from Law Dome, Antarctica (1600–1957). We use annual global estimates of the ocean sink and CO_2 emissions from fossil fuel burning and industry (including the cement carbonation sink) as put forth by Friedlingstein et al. (2020).

2.3 | Accounting for uncertainty in budget terms

In assessing each land use flux estimate via Equation (2), we apply randomly generated temporally autoregressive noise to the atmospheric CO_2 record (used to calculate AGR), FF, and O to allow for uncertainty in these inputs. The autoregressive noise $x_{(t)}$ is produced using the following construction:

$$x_{(t)} = \mathrm{AR1} \cdot x_{(t-1)} + \mathrm{AR2} \cdot x_{(t-2)} + C_1 \cdot \varepsilon_{(t)} \quad (4)$$

where AR1 and AR2 represent the lag 1 and lag 2 autoregressive coefficients, $C_1 = \sqrt{1 - \mathrm{AR1}^2 - \mathrm{AR2}^2}$ represents a scaling factor that normalizes the standard deviation of $x_{(t)}$ to 1, and ε is a Gaussian random variable with mean of 0 and standard deviation of 1. Once calculated, $x_{(t)}$ is scaled to have a standard deviation matching the published decadal uncertainty σ. The specific values used for each of the carbon budget terms are detailed in Table 1. This overall approach follows the "el camino" method described in Ballantyne et al. (2015). Autoregressive errors in FF and B are adopted directly from Ballantyne et al. (2015) and Anderegg et al. (2015). The autoregressive error in CO_2 after 1958 is based on Ballantyne et al. (2012).

To account for errors in the atmospheric CO_2 record before 1958, we construct 10,000 bootstrap simulations of the ice core CO_2 data between 1600 and 1957. To construct one bootstrapped time series, from the observed 79-point ice core record time series spanning 1600–1957 we randomly sample with replacement 79 data points with their associated timestamps. This process is repeated 10,000 times. The bootstrap simulations are then joined with the direct atmospheric CO_2 measurements for 1958–2019 and together fit with a smoothing spline. The time series are joined before the spline to ensure continuity between the ice core and atmospheric records. For each of the 10,000 time series, we use a smoothing spline with a cutoff period of 7.6 years for the ice core

data and 2 years for the atmospheric measurements (λ = 25.66, 1-month data spacing, weights of 1 and 0.069 for ice core and atmospheric data, respectively. Parameters are chosen to obtain the desired approximate cutoff periods) (Bruno & Joos, 1997; Enting, 1987). We opt for a relatively low cutoff period for the ice core data as a conservative application of uncertainty. Finally, we truncate each of the 10,000 bootstrapped and spline-fit time series to the years 1900–1957. One of each of these 10,000 time series is joined with one generation of the CO_2 record 1958 and later which includes random temporally autoregressive noise. We then differentiate this joined CO_2 record to calculate the annual AGR centered on July 1 for each model run. This process is repeated for each bootstrapped CO_2 simulation for data prior to 1958 to produce 10,000 instances of the AGR.

We allow for uncertainty in the terrestrial CO_2 sink via bootstrap by randomly choosing with replacement one of 17 DGVM estimates (B_k) in Friedlingstein et al. (2020) for each of the 10,000 ensemble runs. We include multiple formulations of the terrestrial sink rather than applying autoregressive random noise to a central estimate to better allow for systematic bias.

Finally, the distribution of error (Equation 2) for each land use flux estimate LU_j is modeled by creating a 10,000-member ensemble, each member of which includes one pick B_k and one rendering of each of the autoregressive functions and bootstraps. Each land use flux and each ensemble member therein yield a different estimate of the parameters α and β and quality of fit. No special significance is attached to pairs of LU_j and B_k taken from the same DGVM (i.e., $j = k$). The spread in the 17 inputs for B_k and 10,000 instances of AGR, FF, and O are shown in Figure S2.

3 | RESULTS AND DISCUSSION

3.1 | Constraints on decadal variability in land use flux

We find that land use flux estimates with greater decadal variability yield larger errors in Equation (2) for both the 1900–2019 and 1959–2019 timeframes (Figure 2). The model errors increase approximately linearly with the variance in the land use flux input. This relationship appears in both fitting timeframes, with the 1959–2019 period showing a tighter relationship and a greater increase in error per increase in variance than fits over 1900–2019.

To illustrate differences in quality of fit, we examine the RMSE across the 10,000-member ensembles for three land use cases: H&N, BLUE, and CONST. H&N and BLUE are chosen because they make up two of the three estimates that are averaged to report the global land use flux in the Global Carbon Project, and out of these three estimates represent the high- and low-variance endmembers (Figure 1). We also examine the constant land use flux scenario because of its consistently low errors.

As shown in Figure 3, we find that using CONST and H&N leads to similar distributions of RMSE with means of 0.50 and 0.52 PgC year^{-1} respectively, while BLUE yields a higher average

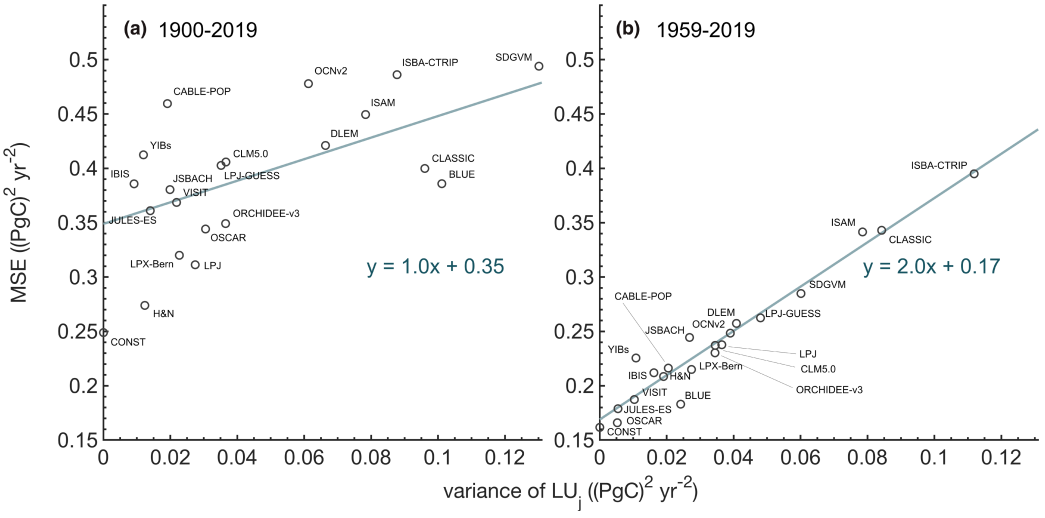

FIGURE 2 Relationship between regression errors in Equation (2) and decadal variability in the land use flux LU_j used as input, with separate analyses for the 1900–2019 (panel [a]) and 1959–2019 (panel [b]) timeframes. The decadal variability in the land use flux is represented as the variance of the decadally smoothed land use flux over each period after removing a linear trend, and the model errors are shown as the mean annual mean squared error (MSE) over the same period across each land use flux's 10,000-member ensemble. The lines and accompanying equations are a linear least-squares fit to the data excluding CONST. All reported data for the grouped land use fluxes hereafter exclude model runs for the CONST case.

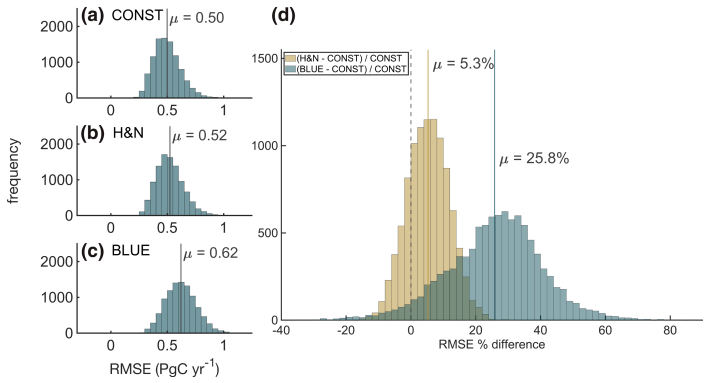

FIGURE 3 Panels (a-c) show the distributions of 10,000-member ensemble error (Equation 3) for runs using CONST, H&N, or BLUE as input for the land use flux over 1900–2019. Panel [d] shows the distributions of the percent differences in error from the 10,000-member ensembles using H&N or BLUE as input for the land use flux compared to the error when using CONST for each member of the ensemble. Ensemble errors are shown as the root mean squared error (RMSE). The interquartile range for the H&N distribution in panel (d) is 9.1% and for the BLUE distribution in panel (d) 18.3%. The dashed vertical line in panel [d] marks zero percent difference, and for all panels the solid vertical lines mark the mean (μ) of each distribution. We hereafter report and discuss results for the 1900–2019 fitting period by default unless otherwise specified.

error of 0.62 PgC year^{-1}. Figure 3d shows the same information, but after calculating the percent difference in RMSE between H&N and CONST or BLUE and CONST on a point-by-point basis through the ensemble (i.e., for identical picks for B_k and time series of noise in AGR, O, and FF). This shows that the RMSE for H&N and BLUE are both systematically higher than that for CONST, with a larger difference for BLUE. The RMSE for the CONST ensemble is lower than the RMSE for any of the published estimates. The model errors for all 21 land use flux cases are listed in Table S1.

The strong correlation between average regression error and decadal variability in land use fluxes can be understood by examining their time histories (Figure 4). We focus again on H&N, BLUE, CONST, and additionally ISBA-CTRIP as a representative high-variance DGVM estimate. The errors of BLUE and ISBA-CTRIP both show a prominent positive excursion in the late 1950s, which coincides with a large variation in the BLUE and ISBA-CTRIP fluxes over the same period. The model errors for CONST and H&N are smaller and generally similar to one another, showing an overestimation of atmospheric growth around 1950 and in the mid-2000s. The mid-2000s error also appears in the ISBA-CTRIP error time series.

The compatibility of land use fluxes with the atmospheric CO_2 growth rate can also be examined in relation to the residual terrestrial sink that is required to balance the global budget ($B_{res} = FF + LU_j - O - AGR$). As shown in Figure 5, the residual sink demanded by BLUE strengthens rapidly from 1920 to 1960, then reverses trajectory and weakens until 1980. This behavior deviates qualitatively from the multi-model mean (B_{GCP}) reported by Friedlingstein et al. (2020) (shown in pink), which increases more uniformly with time. In contrast to BLUE, the terrestrial sink calculated from CONST grows more uniformly after 1900 with smaller decadal variations, leading to a residual terrestrial sink that also grows relatively uniformly with time, in better agreement with models.

The features contributing to error in the higher variability land use flux estimates may be tied to known issues with the methodology used to produce these estimates. In the case of the BLUE and ISBA-CTRIP land use fluxes, for example, the strong land use flux peak around 1960 and the corresponding errors (Figure 4c,d) coincide with changes in the datasets used as inputs before and after 1961. The DGVMs, BLUE, and part of the simulations underlying OSCAR use the harmonized land use change data LUH2 (Chini et al., 2021; Hurtt et al., 2020), which is based on the HYDE population and land use dataset (Goldewijk, Beusen, et al., 2017; Goldewijk, Dekker, et al., 2017). HYDE transforms the country-level statistics on agricultural areas from the Forest and Agriculture Organization (FAO, FAOSTAT, 2021) into spatially explicit maps using ancillary data from satellite remote sensing and rules on how agricultural land is distributed at the sub-national level. Since the FAO estimates only begin in 1961, agricultural areas for earlier time periods are approximated by combining population estimates with per capita land use estimates that follow a curved trajectory based on the (limited) available historical sources. This switch in methodology in 1961 is the likely cause of the high land use flux prior to the 1960s and the subsequent drop (Bastos et al., 2021). The quickening growth in the land use flux between 1940 and 1960 may also be connected to a misrepresentation in the construction of these fluxes. There is evidence that LUH2, which underlies BLUE and DGVM-based estimates including ISBA-CTRIP, does not accurately capture the increase in terrestrial CO_2 uptake associated with land abandonment occurring in the former Soviet Union during the 1940s (Bastos et al., 2016), causing flux estimates to be artificially high during this period.

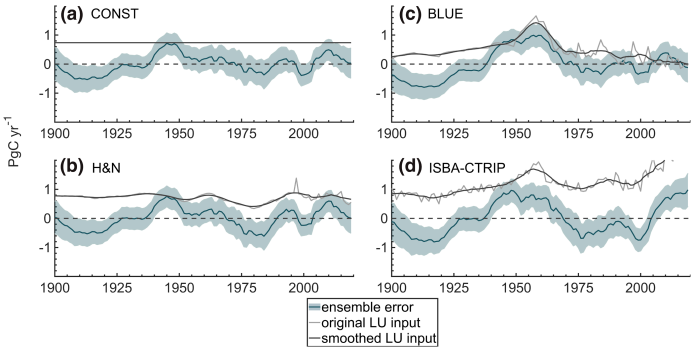

FIGURE 4 Comparison of averaged ensemble error (dark teal) for each land use flux ([a] CONST, [b] H&N, [c] BLUE, and [d] ISBA-CTRIP), shown with an error envelope ($\pm 1\sigma$) in lighter teal. The land use flux (LU), which has been adjusted by the ensemble-averaged fitting parameter α, is shown both in the 10-year smoothed (dark grey) and unsmoothed (light grey) forms.

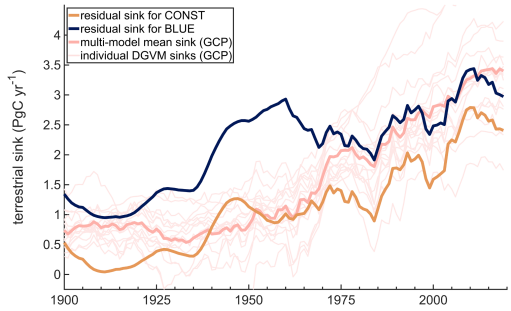

FIGURE 5 Comparisons of terrestrial sink estimates, including sinks inferred as the residual of Equation (1) (B_{res}) assuming different estimates for LU_j where $B_{res} = FF + LU_j - O - AGR$, where LU_j is either CONST or BLUE. Thin pink lines represent estimates of individual models of B per Friedlingstein et al. (2020). No adjustment is made to the means of the land use fluxes in this figure. All data have 10-year smoothing applied.

The upswing and corresponding errors in Figure 4 for ISBA-CTRIP in recent decades are probably unrelated to a concurrent switch in accounting in the underlying dataset HYDE. The HYDE dataset switches from using only decadal to using annual data in 2000, and the consequently higher interannual variability may have increased emissions due to the asymmetry of decay and regrowth (Friedlingstein et al., 2022) and may be a reason for the higher errors in the last decades. However, this switch in accounting applies also to BLUE, which relies on the HYDE dataset but does not show signs of greater error in recent decades, suggesting that the switch to annual data may not be responsible for the upswing seen in DGVMs.

The errors in Figure 4 for ISBA-CTRIP since 2000 may instead be explained by biases in deforestation rates in the LUH2 dataset (Bastos et al., 2020). These biases have been corrected in subsequent versions (Chini et al., 2021). Therefore, the ISBA-CTRIP estimate we use (from Friedlingstein et al. (2020)) is still subject to these biases, but the BLUE estimate (from Friedlingstein et al. (2022)) is not. The post-2000 increase in the ISBA-CTRIP land use flux estimate may also be exacerbated by the inclusion of "loss of additional sink capacity" (discussed in Section 3.2.1), which reinforces increases in the land use flux and is not represented in bookkeeping-based estimates. Overall, these connections between the errors in land use flux estimates and their methodologies illustrate the process by which the atmospheric CO_2 growth rate's constraint on decadal variability may be used to diagnose underlying issues in land use flux estimates.

3.2 | Constraint on the mean land use flux

3.2.1 | Additive parameter α

Information on model performance is also contained in the distribution of the parameter α. Figure 6 shows histograms of α across the full ensemble of land use models for both time periods. We find that the distributions span zero, with a mean value below zero for both time periods. We also find that α is strongly correlated with the time-averaged land use flux estimates used for each fit, with an especially strong correlation for the full 1900–2019 period (Figure 6a and Table 2).

What significance is implied by the distributions of α centering below zero? To address this question, we start with the hypothesis that the ensemble of estimates of the different budget terms, including the model-to-model variations in the published estimates of LU and B, reflect purely random variations around the unknown "true" historical evolution of each of those quantities. If this hypothesis were true, then the distribution of α values associated with the 20 LU model estimates would be expected to have a mean of zero. (This expectation is supported by additional runs using a hypothetical atmospheric record produced via forward runs driven by the ensemble mean estimates for the budget terms. Method and results are detailed in SI.) In contrast, the mean of α across the 20 models (histograms in Figure 6) differs from zero by ~2 times the standard error on both timeframes (SE = std(α)/sqrt(20-1) = 0.16 PgC year^{-1} for 1900–2019 and SE = 0.26 PgC year^{-1} for 1959–2019; distributions shown in Figure 6 histograms). We calculate the standard error using 19 degrees of freedom, conservatively treating the 20 different land use cases as the only varying parameters between runs.

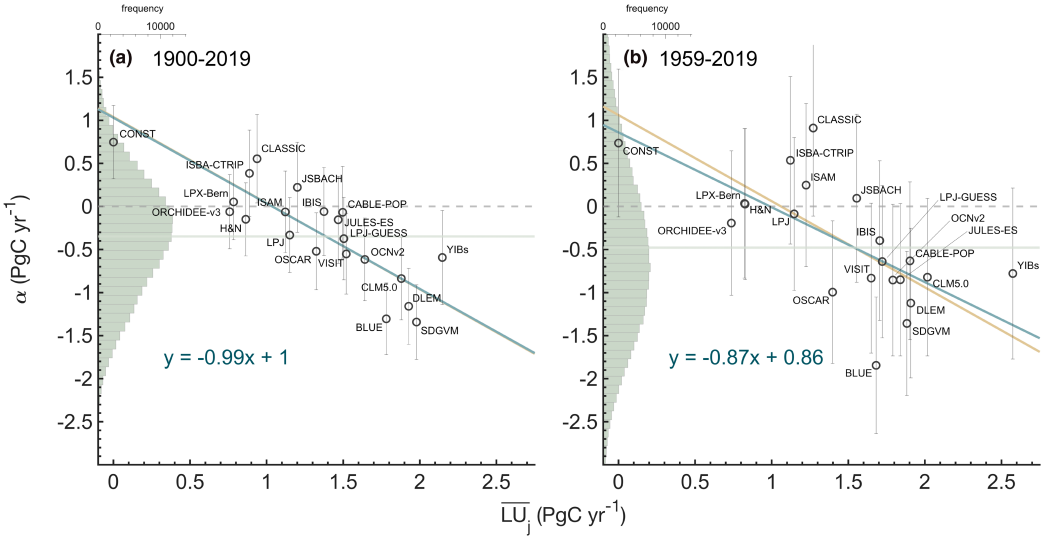

FIGURE 6 Comparison of the ensemble-averaged best fit of additive parameter α (Equation 2) and the time average of the land use flux specified in the ensemble (LU_j), fit and calculated over the 1900–2019 (panel [a]) and 1959–2019 (panel [b]) periods. Points are shown with ±1 standard deviation of the value for α in each LU_j ensemble. The time average of LU_j (denoted as $\overline{LU_j}$) is calculated after applying 10-year smoothing. The teal lines and accompanying equations are a linear least-squares fit to the data, whereas the gold lines are fits to the data with slopes equal to unity (the gold line is obscured by the teal line in panel [a]). Also shown are histograms of the model-fitted values of α across the 20×10,000 ensemble runs for each fitting period (panel [a]: $\mu = -0.35 \pm 0.70$; panel [b]: $\mu = -0.48 \pm 1.11$). Zero is marked with a dashed line and the histogram means are marked with a solid line that extends into the scatter. The ensemble means of $\overline{LU_j} + \alpha$ for each time period can be inferred from the projection onto the x-axis of the intersection point of the gold line (slope = 1, line of constant $\overline{LU_j} + \alpha$) and the zero line.

TABLE 2 Correlation coefficients and *p*-values of the relationship between (i) the means of fitting parameters α and β across ensemble runs specific to each model input and (ii) means of model inputs of the land use flux ($\overline{LU_j}$, where overbar denotes the time average) and terrestrial sink ($\overline{B_k}$)

		$\overline{LU_j}$		$\overline{B_k}$	
		1900–2019	1959–2019	1900–2019	1959–2019
α	Correlation coefficient	−0.80	−0.60	0.46	0.12
	p-value	2.5×10^{-5}	0.0049	0.060	0.64
β	Correlation coefficient	0.0071	0.11	−0.56	−0.62
	p-value	0.98	0.63	0.021	0.0083

Note: For example, values of α found when using each of the 20 inputs for LU are compared to the means of the respective LU, with the fits performed over the 1900–2019 fitting timeframe and $\overline{LU_j}$ calculated over 1900–2019, in the case of the 1900–2019 column. *p*-values are calculated using the MATLAB *corrcoef* function. Model inputs LU_j are assumed to be independent, as are B_k (discussed above). Scatterplots of these data are embedded in Figure 6 and displayed in isolation in SI (Figures S6 and S7).

Thus, we are able to falsify the hypothesis. Of course, one might argue that the hypothesis was anyway doubtful because the different models for LU and *B* share assumptions, methods and input datasets. Nevertheless, our ability to falsify the hypothesis using atmospheric data has broader implications, because it provides a means to identify a specific bias that was previously not recognized.

How should we interpret the strong correlation between α and the mean land use fluxes across the 20-model ensemble? We argue that this correlation suggests that α is best interpreted as a correction to the budget imbalance involving LU. This interpretation is supported by the following points: First, the range in α is larger than the uncertainties in AGR, FF, and O, so α cannot be significantly associated with errors in these terms. Second, a similarly strong correlation as that between α and the mean land use flux is not found between α and the mean land sink *B* over either the 1900–2019 or 1959–2019 periods (correlations shown in Table 2; Figures S6 and S7). Third,

TABLE 3 Average values of $\overline{LU_j} + \alpha$, where α is the ensemble-averaged best fit additive parameter and $\overline{LU_j}$ is the mean across all 20 land use flux cases

	$\overline{LU_j} + \alpha$	
	1900–2019	1959–2019
All LU cases, unweighted	1.04 ± 0.57	1.06 ± 1.04
All LU cases, weighted by 1/MSE	1.06 ± 0.56	0.98 ± 1.03
CONST	0.75 ± 0.43	0.74 ± 0.86
Average of 20 LU cases used in this study (Figure 1)	1.39 ± 0.7	1.54 ± 0.7
Friedlingstein et al. (2022)	1.32 ± 0.7	1.30 ± 0.7

Note: The averages comprise individual ensemble fits of $\overline{LU_j} + \alpha$ for each land use case in the grouping (e.g., 20 LU cases × 10,000 runs = 200,000 ensemble runs for "All LU cases"). "All LU cases" does not include the ensemble runs for the hypothetical constant land use case CONST. Average values of $\overline{LU_j} + \alpha$ are compared to published estimates (bottom two rows). All data are in PgC year^{-1}.

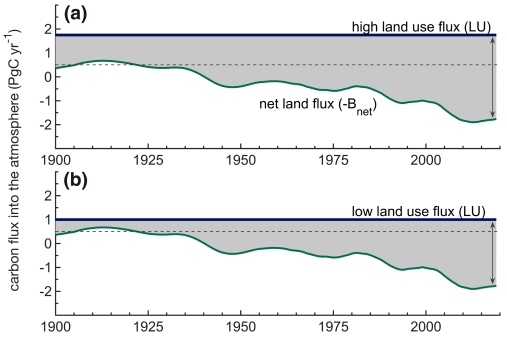

FIGURE 7 The residual terrestrial sink (shaded grey) given two land use flux scenarios with different 1900–2019 means. The residual sink is calculated as the difference between LU (blue line, 1.75 PgC year^{-1} in panel [a] and 1 PgC year^{-1} in panel [b]) and the budget-constrained sign-reversed residual net land flux B_{net} = FF − AGR − O (green curve). The mean 1900–1910 net land flux is marked with a dashed grey line to highlight the relative growth in B_{res} between 1900 and 2019.

interpreting α as a correction to B would significantly change the time evolution of B by reducing its relative growth since 1900 (discussed further below). However, adjusting LU by α does not have this effect, and the offset in α is similar in magnitude to differences in published mean values of LU.

We thus proceed with the assumption that $\overline{LU_j} + \alpha$ can be interpreted as an adjusted estimate of the land use flux mean $\overline{LU_j}$, and report the adjusted flux both for (i) values of α estimated for individual land use cases and (ii) when averaging $\overline{LU_j} + \alpha$ across the 20-model ensemble. For each land use flux case LU_j, we calculate α as the average value across the 10,000 model runs. The resulting $\overline{LU_j} + \alpha$ value for each land use flux case is lower than $\overline{LU_j}$ in the majority of cases (Figure 6 and Table S1). Averaging $\overline{LU_j} + \alpha$ across land use flux cases yields values that are consistently lower than the average of the 20 versions of $\overline{LU_j}$ as well as the Friedlingstein et al. (2022) estimate (Table 3), which is an average of the three bookkeeping estimates H&N, BLUE, and OSCAR. These adjusted land use flux estimates are robust to the details of averaging. An unweighted average of the adjusted land use flux across the 20-model ensemble (excluding CONST) yields 1.04 ± 0.57 PgC year^{-1} when optimizing over 1900–2019 and 1.06 ± 1.04 PgC year^{-1} when optimizing over 1959–2019 (Table 3). Weighting inversely with model error (MSE) yields 1.06 ± 0.56 PgC year^{-1} and 0.98 ± 1.03 PgC year^{-1} when optimizing over 1900–2019 and 1959–2019, respectively. The corresponding estimate for the CONST scenario (for which $\overline{LU_j} = 0$) yields 0.75 ± 0.43 PgC year^{-1} and 0.74 ± 0.86 PgC year^{-1} for 1900–2019 and 1959–2019, respectively. For the 1900–2019 period, the spread in $\overline{LU_j} + \alpha$ is reduced below the designated LU uncertainty of 0.7 PgC year^{-1} quoted in Friedlingstein et al. (2022). The 1959–2019 period does not show a reduced spread in $\overline{LU_j} + \alpha$ because the adjustment incorporates uncertainty in the other terms of the budget, particularly fossil fuel emission, which is a large source of uncertainty in recent years.

What aspects of the record yield this emergent constraint on the mean land use flux? To address this point, we consider the simplest case of a constant land use flux, which essentially contains the same constraint. The atmospheric budget tightly constrains the time history of the residual net land flux, B_{net} = FF − AGR − O. With this constraint, the relative growth in the terrestrial sink, calculated as the residual of the budget (B_{res}), is strongly dependent on the constant value assumed for LU. A high value for LU yields much lower relative growth in B_{res} than a low LU mean (Figure 7). A constraint on the relative growth in B, combined with the assumption that LU is relatively constant, is therefore sufficient to constrain LU.

Our ability to constrain the constant α and to interpret this as an adjustment to the mean land use flux is therefore strongly conditioned upon the published estimates of LU and B having distinct temporal patterns, with LU remaining relatively constant over the evaluation periods, and B growing strongly. This aspect of the published estimates is clearly rooted in mechanistic understanding. The land use flux is driven by competing influences that reduce its long-term trend. Although the global population grew fourfold from 1900 to 2019, the relative influence of population on land use is largely offset by changes in technology (Goldewijk, 2001; Meyer & Turner, 1992), such as the advent of industrialized agriculture in the post-war era (Pongratz et al., 2008). Hong et al. (2021) showed that after 1960 substantial growth in population and agricultural production per capita was largely balanced by decreases in land required per unit of agricultural production associated with agricultural intensification. And although rates of tropical deforestation have increased since 1900, their resulting CO_2 emissions have been largely offset by fire suppression and declining deforestation elsewhere along with the resulting drawdown of CO_2 from regrowth in abandoned deforested and agricultural areas (Houghton et al., 2012).

In contrast, the known drivers of the terrestrial sink have all accelerated since 1900. Gross primary production, water use efficiency of plants, and biomass production have, all with high confidence,

increased (Walker et al., 2020). Nitrogen deposition is also shown to have increased since 1900 (Ackerman et al., 2019; Galloway & Cowling, 2002), which has enhanced global net primary production (Magnani et al., 2007; Reay et al., 2008). Furthermore, fertilization of the terrestrial biosphere by increasing atmospheric CO_2 concentrations has been repeatedly shown to be a primary driver of the terrestrial CO_2 sink (Ciais et al., 2013; Huntzinger et al., 2017; Piao et al., 2013; Sitch et al., 2008; Walker et al., 2020). While the sensitivities of the terrestrial CO_2 sink to these processes remain uncertain, these processes have all clearly increased since 1900, supporting strong growth in the terrestrial CO_2 sink.

We are aware of at least one driver of LU that may have grown similarly to *B*, that is, the "loss of additional sink capacity" (Pongratz et al., 2014). This flux, which is included in DGVMs but not bookkeeping estimates of the land use flux, represents the lost capacity in the terrestrial sink due to land use and has similar drivers to the terrestrial sink. In our model, such a flux would be attributed to a decline in the strength of the terrestrial sink $\beta \cdot B_k$ (discussed in Section 3.2.2). Although we would expect such a decline to be reflected in our model's terrestrial sink, we do not see an obvious difference in $\beta \cdot B_k$ between models that do (DGVMs) and do not (bookkeeping) include lost sink capacity in the land use flux (Table S1). There is currently no consensus on how to incorporate the loss of additional sink capacity into land use models and this flux is sensitive to the details of the modeling approach (Pongratz et al., 2014).

An important question is whether the atmospheric budget can resolve changes in the land use flux on a broader range of timescales than explored here. Answering this remains difficult because of ambiguity in how to assign model error; while the residual errors in Figure 4 might be due to the land use flux, they might also be due to errors in other terms. In line with this reasoning, our model cannot be inverted to produce an optimized land use flux to a decadal precision better than the RMSE of the CONST land use flux case (±0.5 PgC $year^{-1}$); we take the RMSE of CONST as an optimistic (lower bound) estimate of decadal model error. Possible decadal changes in the land use flux highlighted in other studies, for example, wartime impacts on land use (Bastos et al., 2018) and interannual changes in deforestation rates (Hansen et al., 2013; Houghton et al., 2012), are therefore not challenged by our results.

3.2.2 | Implications for the terrestrial sink

Although we mainly focus on implications for the land use flux, our method also yields insights on the magnitude of the terrestrial sink, *B*. We interpret β as a corrective scaling factor on the terrestrial sink pick B_k. Across the 20-LU model grouped ensemble fit over 1959–2019, the average value of $\beta \cdot \overline{B_k}$ is 1.99 ± 1.05 PgC $year^{-1}$ over the same period, which is ~15% smaller than the multi-model mean terrestrial sink reported in Friedlingstein et al. (2020) of 2.35 ± 0.60 PgC $year^{-1}$ over the same time period (Table S2). We note, however, that the bias suggested by β is not as strong as that suggested by α. If *B* were unbiased, β would bracket unity. Our model finds values for β of 0.93 ± 0.39 for 1900–2019 and 0.89 ± 0.50 for 1959–2019, which are closer to unity within the standard error (DOF = 19).

3.2.3 | Implications for climate sensitivity

The mean land use flux since 1900 is relevant to metrics of climate sensitivity that hinge on the ratio of observed warming to cumulative emissions, such as the transient climate response to cumulative emissions (TCRE) (Millar & Friedlingstein, 2018). Millar and Friedlingstein use a combination of results by Houghton et al. (2012) and Van Der Werf et al. (2010) as reported by Le Quéré et al. (2016), including a land use flux with a 1900–2016 mean of 1.1 PgC $year^{-1}$ to estimate the TCRE. If we assume the true land use flux is relatively constant and has a 1900–2019 mean of 1.04 PgC $year^{-1}$, then the cumulative anthropogenic CO_2 emissions (FF + LU) 2016 and prior are reduced by ~4%, corresponding to a 4% increase in the TCRE, implying that future increases in global temperature are underpredicted.

3.2.4 | Implications for airborne fraction

The adjusted land use flux is also relevant to estimating trends in the airborne fraction (AF) of CO_2, defined as the annual increment in atmospheric CO_2 divided by the sum of fossil and land use emissions $\left(\mathrm{AF} = \frac{\mathrm{AGR}}{\mathrm{FF+LU}}\right)$. Canadell et al. (2007) used a land use flux updated from Houghton (2003) with a 1959–2006 mean of 1.15 PgC $year^{-1}$ to suggest that the AF increased by 2.5% per decade over the same period. However, calculating the AF trend across each $\overline{\mathrm{LU}_j} + \alpha$ in the 20-model grouping (fit over 1959–2019, with AF trend fit separately for every instance of LU, α and inputs [n = 200,000]) yields an average trend of −0.03 ± 1.52% per decade over 1959–2019. A diminished trend was supported by Knorr (2009), who noted the AFs sensitivity to the land use flux and estimated the trend at 0.7 ± 1.4% per decade after accounting for uncertainties in the global carbon budget, as well as by van Marle et al. (2022), who use visibility data in forest regions to estimate a new land use flux estimate and report a decrease in AF of 0.014 ± 0.010 $decade^{-1}$ since 1959.

4 | SUMMARY

We show that the observed atmospheric CO_2 growth rate can place meaningful constraints on both the decadal variability and mean of the land use CO_2 flux since 1900 when accounting for variations in the major sources and sinks of CO_2 to the atmosphere. We use estimates of the atmospheric CO_2 growth rate, fossil fuel emissions, ocean sink and natural terrestrial sink in a regression in which we alternately use 20 different estimates of the land use flux. We compare the magnitude and timing of the regression errors when using each land use flux input, as well as examine the significance of the regression fitting parameters.

We find that the observed atmospheric CO_2 growth rate since 1900 is better simulated using land use flux estimates with less decadal variability, and the error in simulating the AGR increases roughly in proportion to the amount of decadal variability in the land use flux. The land use flux estimates have coincident features of variability and error between mid-century that may be the result of issues in the underlying datasets. Most DGVM-based land use flux estimates include large errors after 2000, which also point to potential errors in the inputs common to these estimates. We find that a scenario that assumes the land use flux is constant after 1900 matches the atmospheric CO_2 growth rate better than any previously published estimate, even after allowing a constant additive adjustment to the published estimates.

Our model resolves a budget adjustment that is on average negative and which we interpret as a correction to the mean of published land use fluxes, one of the least well-known components of the global carbon budget. This interpretation is based on the additive correction being strongly correlated with the average land use flux over the last century from different LU estimates but not with the terrestrial sink or other terms in the carbon budget. If we alternately interpret the additive constant as a correction to the terrestrial sink, this greatly reduces the relative growth of the sink since 1900, which is inconsistent with the relative growth of published estimates, as rooted in mechanistic understanding.

Interpreting the additive constant as a correction to the mean land use flux yields an atmospherically adjusted mean land use flux of 1.04 ± 0.57 PgC year^{-1} over 1900–2019 and 1.06 ± 1.04 PgC year^{-1} over 1959–2019. These adjusted values are at the low end of the distribution of published estimates. The downward adjustment to the mean land use flux requires a ~15% reduction in the strength of the natural terrestrial sink over 1959–2019 compared to the multi-model mean published by GCP (Friedlingstein et al., 2020). In all, we find that the atmospheric CO_2 budget favors land use flux estimates with less decadal variability and may resolve an overall downward adjustment to the mean land use flux since 1900.

ACKNOWLEDGMENTS

This work was supported by the National Science Foundation Graduate Research Fellowship Program, by NASA under grant NNX17AE74G, and by Eric and Wendy Schmidt via recommendation of the Schmidt Futures program.

CONFLICT OF INTEREST

The authors declare no competing interests.

DATA AVAILABILITY STATEMENT

The data that support the findings of this study are available in the public domain: https://www.globalcarbonproject.org/, https://scripps.co2.ucsd.edu/, https://gml.noaa.gov/. Data used in this study that are not immediately available online are available at https://doi.org/10.6076/D11G6B.

ORCID

Julia L. Dohner https://orcid.org/0000-0002-6131-3938
Benjamin Birner https://orcid.org/0000-0003-3139-9897
Armin Schwartzman https://orcid.org/0000-0001-5335-1611
Julia Pongratz https://orcid.org/0000-0003-0372-3960
Ralph F. Keeling https://orcid.org/0000-0002-9749-2253

REFERENCES

Ackerman, D., Millet, D. B., & Chen, X. (2019). Global estimates of inorganic nitrogen deposition across four decades. *Global Biogeochemical Cycles*, *33*(1), 100–107. https://doi.org/10.1029/2018GB005990

Anderegg, W. R. L., Ballantyne, A. P., Smith, W. K., Majkut, J., Rabin, S., Beaulieu, C., Birdsey, R., Dunne, J. P., Houghton, R. A., Myneni, R. B., Pan, Y., Sarmiento, J. L., Serota, N., Shevliakova, E., Tans, P., & Pacala, S. W. (2015). Tropical nighttime warming as a dominant driver of variability in the terrestrial carbon sink. *Proceedings of the National Academy of Sciences of the United States of America*, *112*(51), 15591–15596. https://doi.org/10.1073/pnas.1521479112

Arneth, A., Sitch, S., Pongratz, J., Stocker, B. D., Ciais, P., Poulter, B., Bayer, A. D., Bondeau, A., Calle, L., Chini, L. P., Gasser, T., Fader, M., Friedlingstein, P., Kato, E., Li, W., Lindeskog, M., Nabel, J. E. M. S., Pugh, T. A. M., Robertson, E., … Zaehle, S. (2017). Historical carbon dioxide emissions caused by land-use changes are possibly larger than assumed. *Nature Geoscience*, *10*, 79–84. https://doi.org/10.1038/ngeo2882

Ballantyne, A. P., Alden, C. B., Miller, J. B., Tans, P. P., & White, J. W. C. (2012). Increase in observed net carbon dioxide uptake by land and oceans during the past 50 years. *Nature*, *488*, 70–72. https://doi.org/10.1038/nature11299

Ballantyne, A. P., Andres, R., Houghton, R., Stocker, B. D., Wanninkhof, R., Anderegg, W., Cooper, L. A., DeGrandpre, M., Tans, P. P., Miller, J. B., Alden, C., & White, J. W. C. (2015). Audit of the global carbon budget: Estimate errors and their impact on uptake uncertainty. *Biogeosciences*, *12*(8), 2565–2584. https://doi.org/10.5194/bg-12-2565-2015

Bastos, A., Ciais, P., Barichivich, J., Bopp, L., Brovkin, V., Gasser, T., Peng, S., Pongratz, J., Viovy, N., & Trudinger, C. M. (2016). Re-evaluating the 1940s CO_2 plateau. *Biogeosciences*, *13*(17), 4877–4897. https://doi.org/10.5194/bg-13-4877-2016

Bastos, A., Hartung, K., Nützel, T. B., Nabel, J. E. M. S., Houghton, R. A., & Pongratz, J. (2021). Comparison of uncertainties in land use change fluxes from bookkeeping model parameterisation. *Earth System Dynamics*, *12*(2), 745–762. https://doi.org/10.5194/esd-12-745-2021

Bastos, A., O'Sullivan, M., Ciais, P., Makowski, D., Sitch, S., Friedlingstein, P., Chevallier, F., Rödenbeck, C., Pongratz, J., Luijkx, I. T., Patra, P. K., Peylin, P., Canadell, J. G., Lauerwald, R., Li, W., Smith, N. E., Peters, W., Goll, D. S., Jain, A. K., … Zaehle, S. (2020). Sources of uncertainty in regional and global terrestrial CO_2 exchange estimates. *Global Biogeochemical Cycles*, *34*(2), Article e2019GB006393. https://doi.org/10.1029/2019GB006393

Bastos, A., Peregon, A., Gani, É. A., Khudyaev, S., Yue, C., Li, W., Gouveia, C. M., & Ciais, P. (2018). Influence of high-latitude warming and land use changes in the early 20th century northern Eurasian CO_2 sink. *Environmental Research Letters*, *13*, 065014. https://doi.org/10.1088/1748-9326/aac4d3

Blyth, E. M., Arora, V. K., Clark, D. B., Dadson, S. J., De Kauwe, M. G., Lawrence, D. M., Melton, J. R., Pongratz, J., Turton, R. H., Yoshimura, K., & Yuan, H. (2021). Advances in land surface modelling. *Current Climate Change Reports*, *7*, 45–71. https://doi.org/10.1007/s40641-021-00171-5

Booth, B. B. B., Harris, G. R., Murphy, J. M., House, J. I., Jones, C. D., Sexton, D., & Sitch, S. (2017). Narrowing the range of future climate projections

using historical observations of atmospheric CO_2. *Journal of Climate*, *30*(8), 3039–3053. https://doi.org/10.1175/jcli-d-16-0178.1

Broecker, W. S., Takahashi, T., Simpson, H. J., & Peng, T. H. (1979). Fate of fossil fuel carbon dioxide and the global carbon budget. *Science*, *206*(4417), 409–418. https://doi.org/10.1126/science.206.4417.409

Bruno, M., & Joos, F. (1997). Terrestrial carbon storage during the past 200 years: A Monte Carlo analysis of CO_2 data from ice core and atmospheric measurements. *Global Biogeochemical Cycles*, *11*(1), 111–124. https://doi.org/10.1029/96GB03611

Canadell, J. G., Le Quéré, C., Raupach, M. R., Field, C. B., Buitenhuis, E. T., Ciais, P., Conway, T. J., Gillett, N. P., Houghton, R. A., & Marland, G. (2007). Contributions to accelerating atmospheric CO_2 growth from economic activity, carbon intensity, and efficiency of natural sinks. *Proceedings of the National Academy of Sciences of the United States of America*, *104*(47), 18866–18870. https://doi.org/10.1073/pnas.0702737104

Chini, L., Hurtt, G., Sahajpal, R., Frolking, S., Klein Goldewijk, K., Sitch, S., Ganzenmüller, R., Ma, L., Ott, L., Pongratz, J., & Poulter, B. (2021). Land use harmonization datasets for annual global carbon budgets. *Earth System Science Data*, *13*(8), 4175–4189. https://doi.org/10.5194/essd-13-4175-2021

Ciais, P., Sabine, C., Bala, G., Bopp, L., Brovkin, V., Canadell, J., Chhabra, A., DeFries, R., Galloway, J., Heimann, M., Jones, C., Le Quéré, C., Myneni, R. B., Piao, S., & Thornton, P. (2013). Carbon and other biogeochemical cycles. In T. F. Stocker, D. Qin, G.-K. Plattner, M. Tignor, S. K. Allen, J. Boschung, A. Nauels, Y. Xia, V. Bex, & P. M. Midgley (Eds.), *Climate change 2013: The physical science basis. Contribution of Working Group I to the fifth assessment report of the Intergovernmental Panel on Climate Change* (pp. 465–570). Cambridge University Press.

Conway, T., & Tans, P. (2009). *Atmospheric carbon dioxide mixing ratios from the NOAA CMDL carbon cycle cooperative global air sampling network* (2009). (No. NDP-005). Environmental System Science Data Infrastructure for a Virtual Ecosystem (ESS-DIVE), Carbon Dioxide Information Analysis Center (CDIAC) & Oak Ridge National Laboratory (ORNL). https://doi.org/10.3334/CDIAC/ATG.NDP005

Crameri, F. (2021). Scientific colour maps, Version 7.0.1. *Zenodo*. https://doi.org/10.5281/zenodo.5501399

Crameri, F., Shephard, G. E., & Heron, P. J. (2020). The misuse of colour in science communication. *Nature Communications*, *11*, Article 5444. https://doi.org/10.1038/s41467-020-19160-7

Delire, C., Séférian, R., Decharme, B., Alkama, R., Calvet, J.-C., Carrer, D., Gibelin, A.-L., Joetzjer, E., Morel, X., Rocher, M., & Tzanos, D. (2020). The global land carbon cycle simulated with ISBA-CTRIP: Improvements over the last decade. *Journal of Advances in Modeling Earth Systems*, *12*(9), Article e2019MS001886. https://doi.org/10.1029/2019MS001886

Enting, I. G. (1987). On the use of smoothing splines to filter CO_2 data. *Journal of Geophysical Research*, *92*(D9), 10977–10984. https://doi.org/10.1029/JD092iD09p10977

FAOSTAT. (2021). Food and Agriculture Organization Statistics Division, http://faostat.fao.org/

Feng, Y., Zeng, Z., Searchinger, T. D., Ziegler, A. D., Wu, J., Wang, D., He, X., Elsen, P. R., Ciais, P., Xu, R., Guo, Z., Peng, L., Tao, Y., Spracklen, D. V., Holden, J., Liu, X., Zheng, Y., Xu, P., Chen, J., … Zheng, C. (2022). Doubling of annual forest carbon loss over the tropics during the early twenty-first century. *Nature Sustainability*, *5*, 444–451. https://doi.org/10.1038/s41893-022-00854-3

Fisher, R. A., Koven, C. D., Anderegg, W. R. L., Christoffersen, B. O., Dietze, M. C., Farrior, C. E., Holm, J. A., Hurtt, G. C., Knox, R. G., Lawrence, P. J., Lichstein, J. W., Longo, M., Matheny, A. M., Medvigy, D., Muller-Landau, H. C., Powell, T. L., Serbin, S. P., Sato, H., Shuman, J. K., … Moorcroft, P. R. (2018). Vegetation demographics in earth system models: A review of progress and priorities. *Global Change Biology*, *24*(1), 35–54. https://doi.org/10.1111/gcb.13910

Francey, R. J., Trudinger, C. M., Van Der Schoot, M., Krummel, P. B., Steele, L. P., & Langenfelds, R. L. (2010). Differences between trends in atmospheric CO_2 and the reported trends in anthropogenic CO_2 emissions. *Tellus B: Chemical and Physical Meteorology*, *62*(5), 316–328. https://doi.org/10.1111/j.1600-0889.2010.00472.x

Friedlingstein, P., Jones, M. W., O'Sullivan, M., Andrew, R. M., Bakker, D. C. E., Hauck, J., Le Quéré, C., Peters, G. P., Peters, W., Pongratz, J., Sitch, S., Canadell, J. G., Ciais, P., Jackson, R. B., Alin, S. R., Anthoni, P., Bates, N. R., Becker, M., Bellouin, N., … Zeng, J. (2022). Global carbon budget 2021. *Earth System Science Data*, *14*(4), 1917–2005. https://doi.org/10.5194/essd-14-1917-2022

Friedlingstein, P., O'Sullivan, M., Jones, M. W., Andrew, R. M., Hauck, J., Olsen, A., Peters, G. P., Peters, W., Pongratz, J., Sitch, S., Le Quéré, C., Canadell, J. G., Ciais, P., Jackson, R. B., Alin, S., Aragão, L. E. O. C., Arneth, A., Arora, V., Bates, N. R., … Zaehle, S. (2020). Global carbon budget 2020. *Earth System Science Data*, *12*(4), 3269–3340. https://doi.org/10.5194/essd-12-3269-2020

Galloway, J. N., & Cowling, E. B. (2002). Reactive nitrogen and the world: 200 years of change. *Ambio–A Journal of Environment and Society*, *31*(2), 64–71. https://doi.org/10.1579/0044-7447-31.2.64

Gasser, T., Crepin, L. L., Quilcaille, Y., Houghton, R. A., Ciais, P., & Obersteiner, M. (2020). Historical CO_2 emissions from land use and land cover change and their uncertainty. *Biogeosciences*, *17*(15), 4075–4101. https://doi.org/10.5194/bg-17-4075-2020

Goldewijk, K. K. (2001). Estimating global land use change over the past 300 years: The HYDE database. *Global Biogeochemical Cycles*, *15*(2), 417–433. https://doi.org/10.1029/1999GB001232

Goldewijk, K. K., Beusen, A., Doelman, J., & Stehfest, E. (2017). Anthropogenic land use estimates for the Holocene—HYDE 3.2. *Earth System Science Data*, *9*(2), 927–953. https://doi.org/10.5194/essd-9-927-2017

Goldewijk, K. K., Dekker, S. C., & Van Zanden, J. L. (2017). Per-capita estimations of long-term historical land use and the consequences for global change research. *Journal of Land Use Science*, *12*(5), 313–337. https://doi.org/10.1080/1747423X.2017.1354938

Hansen, M. C., Potapov, P. V., Moore, R., Hancher, M., Turubanova, S. A., Tyukavina, A., Thau, D., Stehman, S. V., Goetz, S. J., Loveland, T. R., Kommareddy, A., Egorov, A., Chini, L., Justice, C. O., & Townshend, J. R. G. (2013). High-resolution global maps of 21st-century forest cover change. *Science*, *342*(6160), 850–853. https://doi.org/10.1126/science.1244693

Hansis, E., Davis, S. J., & Pongratz, J. (2015). Relevance of methodological choices for accounting of land use change carbon fluxes. *Global Biogeochemical Cycles*, *29*(8), 1230–1246. https://doi.org/10.1002/2014GB004997

Hartung, K., Bastos, A., Chini, L., Ganzenmüller, R., Havermann, F., Hurtt, G. C., Loughran, T., Nabel, J. E. M. S., Nützel, T., Obermeier, W. A., & Pongratz, J. (2021). Bookkeeping estimates of the net land-use change flux—A sensitivity study with the CMIP6 land-use dataset. *Earth System Dynamics*, *12*(2), 763–782. https://doi.org/10.5194/esd-12-763-2021

Haverd, V., Smith, B., Nieradzik, L., Briggs, P. R., Woodgate, W., Trudinger, C. M., Canadell, J. G., & Cuntz, M. (2018). A new version of the CABLE land surface model (subversion revision r4601) incorporating land use and land cover change, woody vegetation demography, and a novel optimisation-based approach to plant coordination of photosynthesis. *Geoscientific Model Development*, *11*(7), 2995–3026. https://doi.org/10.5194/gmd-11-2995-2018

Hong, C., Burney, J. A., Pongratz, J., Nabel, J. E. M. S., Mueller, N. D., Jackson, R. B., & Davis, S. J. (2021). Global and regional drivers of land use emissions in 1961–2017. *Nature*, *589*, 554–561. https://doi.org/10.1038/s41586-020-03138-y

Houghton, R. A. (2003). Revised estimates of the annual net flux of carbon to the atmosphere from changes in land use and land management 1850–2000. *Tellus B*, *55*(2), 378–390. https://doi.org/10.1034/j.1600-0889.2003.01450.x

millennium. *Global Biogeochemical Cycles*, *22*(3), article GB3018. https://doi.org/10.1029/2007GB003153

Pongratz, J., Reick, C. H., Houghton, R. A., & House, J. I. (2014). Terminology as a key uncertainty in net land use and land cover change carbon flux estimates. *Earth System Dynamics*, *5*(1), 177–195. https://doi.org/10.5194/esd-5-177-2014

Poulter, B., Frank, D. C., Hodson, E. L., & Zimmermann, N. E. (2011). Impacts of land cover and climate data selection on understanding terrestrial carbon dynamics and the CO_2 airborne fraction. *Biogeosciences*, *8*(8), 2027–2036. https://doi.org/10.5194/bg-8-2027-2011

Reay, D. S., Dentener, F., Smith, P., Grace, J., & Feely, R. A. (2008). Global nitrogen deposition and carbon sinks. *Nature Geoscience*, *1*(7), 430–437. https://doi.org/10.1038/ngeo230

Riahi, K., Schaeffer, R., Arango, J., Calvin, K., Guivarch, C., Hasegawa, T., Jiang, K., Kriegler, E., Matthews, R., Peters, G. P., Rao, A., Robertson, S., Sebbit, A. M., Steinberger, J., Tavoni, M., & van Vuuren, D. P. (2022). Mitigation pathways compatible with long-term goals, in IPCC, 2022. In P. R. Shukla, J. Skea, R. Slade, A. Al Khourdajie, R. van Diemen, D. McCollum, M. Pathak, S. Some, P. Vyas, R. Fradera, M. Belkacemi, A. Hasija, G. Lisboa, S. Luz, & J. Malley (Eds.), *Climate change 2022: Mitigation of climate change. Contribution of Working Group III to the sixth assessment report of the Intergovernmental Panel on Climate Change*. Cambridge University Press. https://doi.org/10.1017/9781009157926.005

Sellar, A. A., Jones, C. G., Mulcahy, J. P., Tang, Y., Yool, A., Wiltshire, A., O'Connor, F. M., Stringer, M., Hill, R., Palmieri, J., Woodward, S., de Mora, L., Kuhlbrodt, T., Rumbold, S. T., Kelley, D. I., Ellis, R., Johnson, C. E., Walton, J., Abraham, N. L., … Zerroukat, M. (2019). UKESM1: Description and evaluation of the UK earth system model. *Journal of Advances in Modeling Earth Systems*, *11*(12), 4513–4558. https://doi.org/10.1029/2019MS001739

Siegenthaler, U., & Oeschger, H. (1987). Biospheric CO_2 emissions during the past 200 years reconstructed by deconvolution of ice core data. *Tellus B: Chemical and Physical Meteorology*, *39*(1–2), 140–154. https://doi.org/10.3402/tellusb.v39i1-2.15331

Siegenthaler, U., & Sarmiento, J. L. (1993). Atmospheric carbon dioxide and the ocean. *Nature*, *365*, 119–125. https://doi.org/10.1038/365119a0

Sitch, S., Huntingford, C., Gedney, N., Levy, P. E., Lomas, M., Piao, S. L., Betts, R., Ciais, P., Cox, P., Friedlingstein, P., Jones, C. D., Prentice, I. C., & Woodward, F. I. (2008). Evaluation of the terrestrial carbon cycle, future plant geography and climate-carbon cycle feedbacks using five dynamic global vegetation models (DGVMs). *Global Change Biology*, *14*(9), 2015–2039. https://doi.org/10.1111/j.1365-2486.2008.01626.x

Smith, B., Wårlind, D., Arneth, A., Hickler, T., Leadley, P., Siltberg, J., & Zaehle, S. (2014). Implications of incorporating N cycling and N limitations on primary production in an individual-based dynamic vegetation model. *Biogeosciences*, *11*(7), 2027–2054. https://doi.org/10.5194/bg-11-2027-2014

Tian, H., Chen, G., Lu, C., Xu, X., Hayes, D. J., Ren, W., Pan, S., Huntzinger, D. N., & Wofsy, S. C. (2015). North American terrestrial CO_2 uptake largely offset by CH_4 and N_2O emissions: Toward a full accounting of the greenhouse gas budget. *Climate Change*, *129*(3), 413–426. https://doi.org/10.1007/s10584-014-1072-9

Van Der Werf, G. R., Randerson, J. T., Giglio, L., Collatz, G. J., Mu, M., Kasibhatla, P. S., Morton, D. C., Defries, R. S., Jin, Y., & Van Leeuwen, T. T. (2010). Global fire emissions and the contribution of deforestation, savanna, forest, agricultural, and peat fires (1997–2009). *Atmospheric Chemistry and Physics*, *10*(23), 11707–11735. https://doi.org/10.5194/acp-10-11707-2010

van Marle, M. J. E., van Wees, D., Houghton, R. A., Field, R. D., Verbesselt, J., & van der Werf, G. R. (2022). New land-use-change emissions indicate a declining CO_2 airborne fraction. *Nature*, *603*, 450–454. https://doi.org/10.1038/s41586-021-04376-4

Vuichard, N., Messina, P., Luyssaert, S., Guenet, B., Zaehle, S., Ghattas, J., Bastrikov, V., & Peylin, P. (2019). Accounting for carbon and nitrogen interactions in the global terrestrial ecosystem model ORCHIDEE (trunk version, rev 4999): Multi-scale evaluation of gross primary production. *Geoscientific Model Development*, *12*(11), 4751–4779. https://doi.org/10.5194/gmd-12-4751-2019

Walker, A. P., De Kauwe, M. G., Bastos, A., Belmecheri, S., Georgiou, K., Keeling, R., McMahon, S. M., Medlyn, B. E., Moore, D. J. P., Norby, R. J., Zaehle, S., Anderson-Teixeira, K. J., Battipaglia, G., Brienen, R. J. W., Cabugao, K. G., Cailleret, M., Campbell, E., Canadell, J. G., Ciais, P., … Zuidema, P. A. (2020). Integrating the evidence for a terrestrial carbon sink caused by increasing atmospheric CO_2. *New Phytologist*, *229*(5), 2413–2445. https://doi.org/10.1111/nph.16866

Walker, A. P., Quaife, T., van Bodegom, P. M., De Kauwe, M. G., Keenan, T. F., Joiner, J., Lomas, M. R., MacBean, N., Xu, C., Yang, X., & Woodward, F. I. (2017). The impact of alternative trait-scaling hypotheses for the maximum photosynthetic carboxylation rate (V_{cmax}) on global gross primary production. *New Phytologist*, *215*(4), 1370–1386. https://doi.org/10.1111/nph.14623

Wilson, A. T. (1978). Pioneer agriculture explosion and CO_2 levels in the atmosphere. *Nature*, *273*(5657), 40–41.

Woodwell, G. M., Hobbie, J. E., Houghton, R. A., Melillo, J. M., Moore, B., Peterson, B. J., & Shaver, G. R. (1983). Global deforestation: Contribution to atmospheric carbon dioxide. *Science*, *222*(4628), 1081–1086. https://doi.org/10.1126/science.222.4628.1081

Xu, L., Saatchi, S. S., Yang, Y., Yu, Y., Pongratz, J., Bloom, A. A., Bowman, K., Worden, J., Liu, J., Yin, Y., Domke, G., McRoberts, R. E., Woodall, C., Nabuurs, G.-J., de Miguel, S., Keller, M., Harris, N., Maxwell, S., & Schimel, D. (2021). Changes in global terrestrial live biomass over the 21st century. *Science Advances*, *7*(27), Article eabe9829. https://doi.org/10.1126/sciadv.abe9829

Yuan, W. P., Liu, D., Dong, W. J., Liu, S. G., Zhou, G. S., Yu, G. R., Zhao, T. B., Feng, J. M., Ma, Z. G., Chen, J. Q., Chen, Y., Chen, S. P., Han, S. J., Huang, J. P., Li, L. H., Liu, H. Z., Liu, S. M., Ma, M. G., Wang, Y. F., … Zhao, L. (2014). Multiyear precipitation reduction strongly decrease carbon uptake over North China. *Journal of Geophysical Research: Biogeosciences*, *119*(5), 881–896. https://doi.org/10.1002/2014JG002608

Yue, X., & Unger, N. (2015). The Yale interactive terrestrial biosphere model version 1.0: Description, evaluation and implementation into NASA GISS ModelE2. *Geoscientific Model Development*, *8*(8), 2399–2417. https://doi.org/10.5194/gmd-8-2399-2015

Zaehle, S., & Friend, A. D. (2010). Carbon and nitrogen cycle dynamics in the O–CN land surface model: 1. Model description, site-scale evaluation, and sensitivity to parameter estimates. *Global Biogeochemical Cycles*, *24*(1), Article GB1005. https://doi.org/10.1029/2009GB003521

SUPPORTING INFORMATION

Additional supporting information can be found online in the Supporting Information section at the end of this article.

How to cite this article: Dohner, J. L., Birner, B., Schwartzman, A., Pongratz, J., & Keeling, R. F. (2022). Using the atmospheric CO_2 growth rate to constrain the CO_2 flux from land use and land cover change since 1900. *Global Change Biology*, *28*, 7327–7339. https://doi.org/10.1111/gcb.16396

Acknowledgements

This work was supported by the National Science Foundation Graduate Research Fellowship Program, by NASA under grant NNX17AE74B, and by Eric and Wendy Schmidt via recommendation of the Schmidt Futures program. Chapter 1, in full, is a reprint of the material as it appears in *Global Change Biology*, 2022. Dohner, J.L., Birner, B., Schwartzman, A., Pongratz, J., and Keeling, R.F., 2022. The dissertation author was the primary investigator and author of this paper.

Supplemental Information

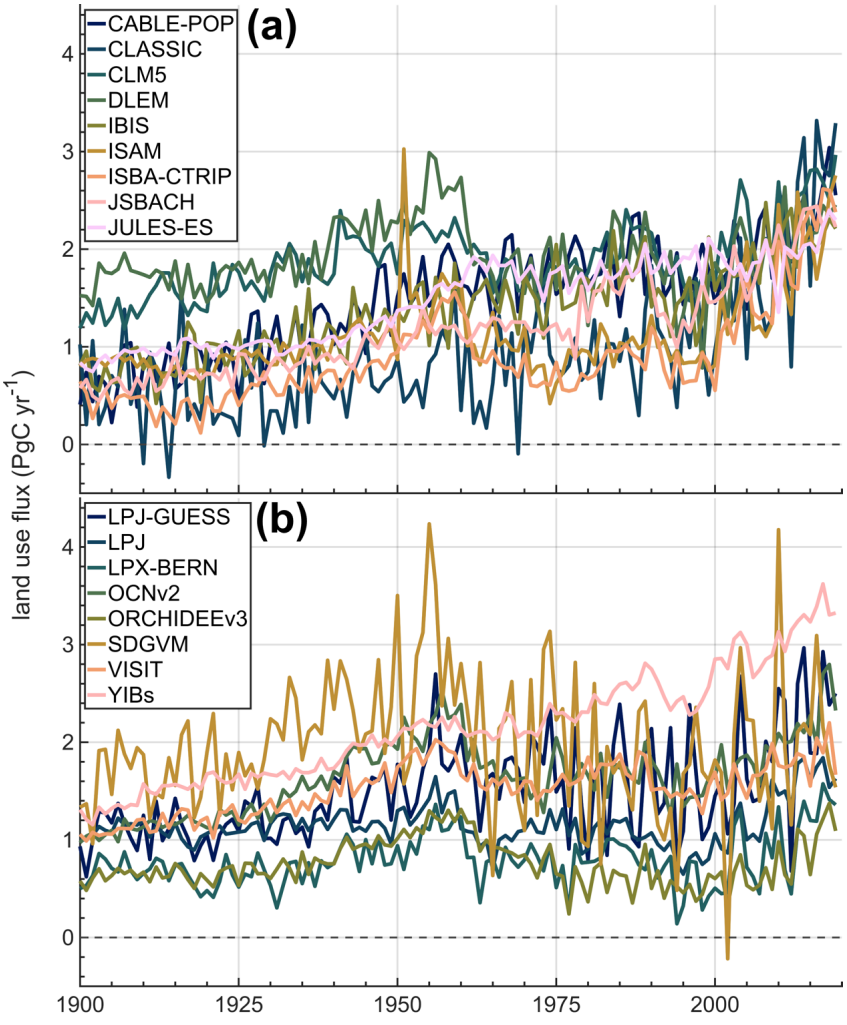

Figure S1. Estimates of land use flux via DGVMs (see Table S1 for references), all shown at annual resolution.

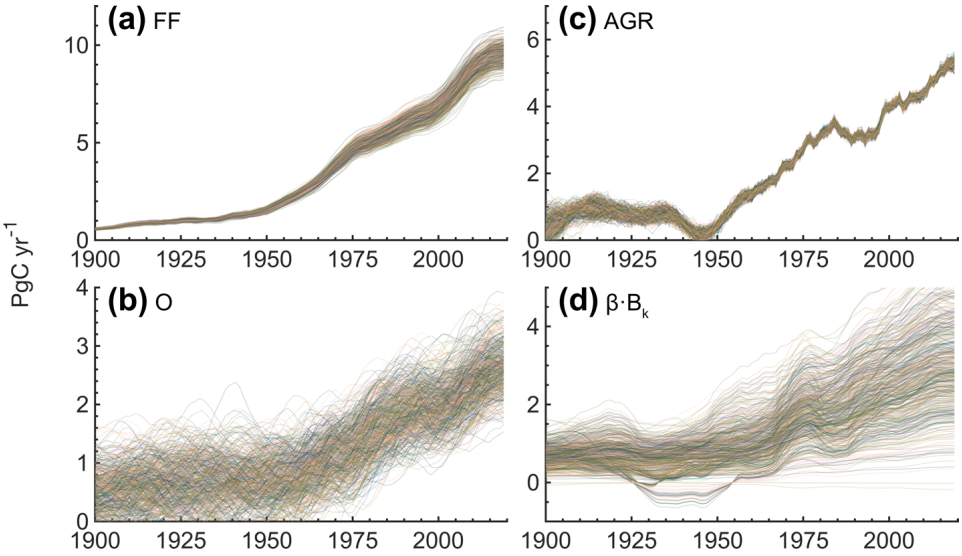

Figure S2. Randomly selected display of 500 of the 10,000 versions of inputs (fossil emissions (FF, includes cement carbonation sink), ocean sink (O), atmospheric CO_2 growth rate (AGR), and natural terrestrial sink ($\beta \cdot B_k$); see Section 2.3), all with 10-year smoothing applied. One of each of the time series that make up the 10,000 versions of each input is used per ensemble member. We show the spread in $\beta \cdot B_k$ rather than across the 17 estimates of B to show the full range that the B term can occupy in the Equation 2 regression.

Forward run method (from Section 3.2.1)

To confirm that fitting parameters α and β bracket zero and unity, respectively, in the circumstance that LU and B lacked any bias, we run the model using an atmospheric CO_2 growth rate calculated as the residual of the terms in Equation 1. This growth rate, hereafter AGR', treats all terms in the budget, after averaging across variations, as being perfectly compatible with the atmospheric CO_2 growth rate. We run the model 10,000 times for each of the 20 land use flux cases, each time using AGR' as input. Noise is applied to each of the input terms (e.g., AGR', FF, O, B) as in Section 2.3. In Figures S3 and S4 we display the spread in α and β across the 20-model ensemble (n = 200,000). Assuming that estimates for LU_j and B_k are independent, we report the standard errors of the distributions: for 1900-2019 and 1959-2019, α is -0.066 ± 0.69 (SE = 0.16) and -0.066 ± 1.14 PgC yr^{-1} (SE = 0.26), respectively, and β is 1.01 ± 0.39 (SE = 0.089) and 1.03 ± 0.53 (SE = 0.12), respectively. We conclude that across both timeframes, the means of the distributions of α and β when modeling with AGR' are not significantly different from zero and unity, respectively.

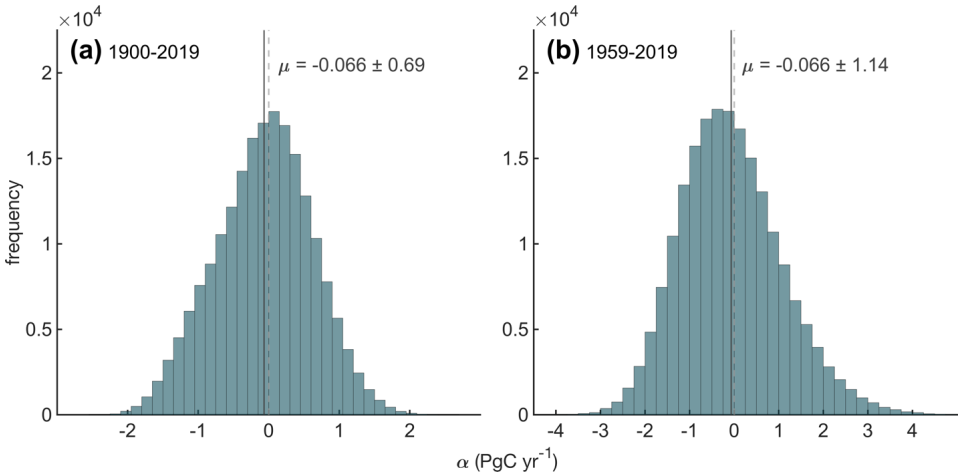

Figure S3. Spread in α across the 20 land use model ensembles (n = 200,000) when using as input an atmospheric growth rate calculated as the residual of the other input terms (including LU_j; Equation 1). The dashed grey vertical lines mark x = 0, and the mean (μ) of each distribution is marked with a solid grey vertical line with the standard deviation.

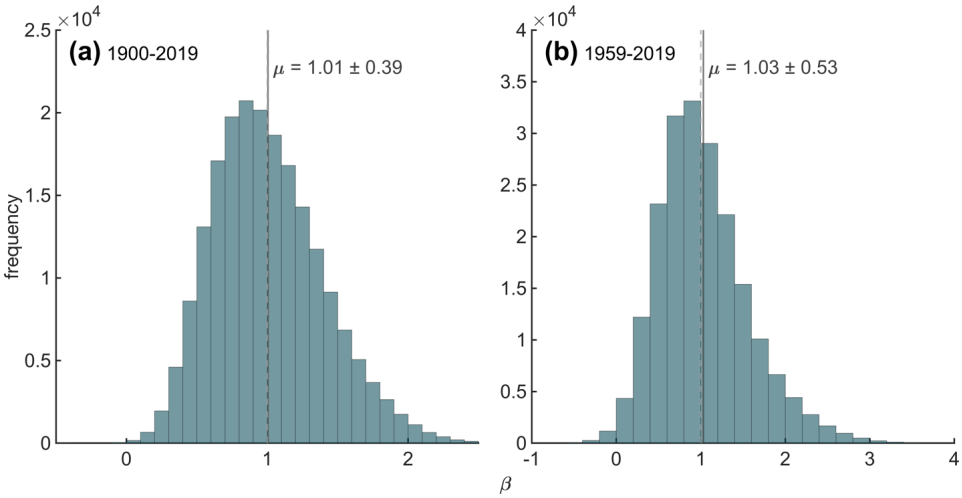

Figure S4. Same as Figure S3 but for spread in β. The dashed grey vertical lines mark x = 1, and the mean (μ) of each distribution is marked with a solid grey vertical line with the standard deviation.

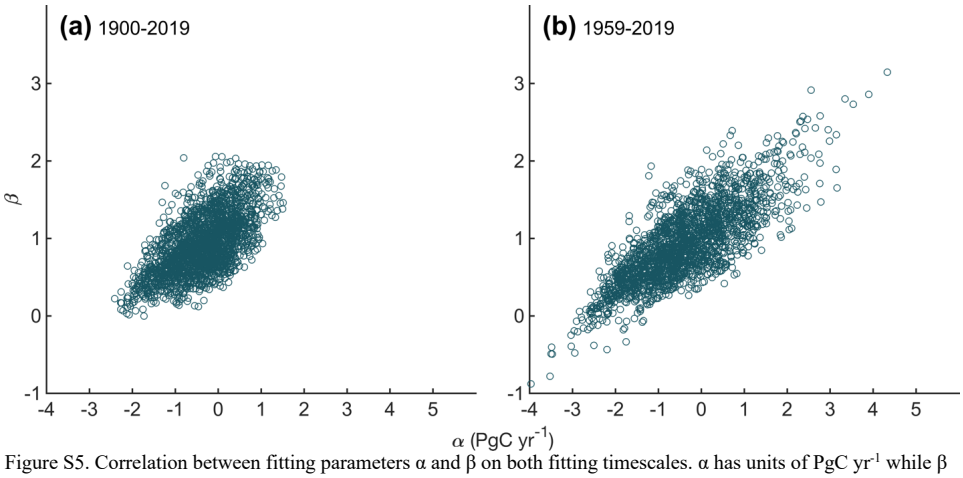

Figure S5. Correlation between fitting parameters α and β on both fitting timescales. α has units of PgC yr^{-1} while β is unitless.

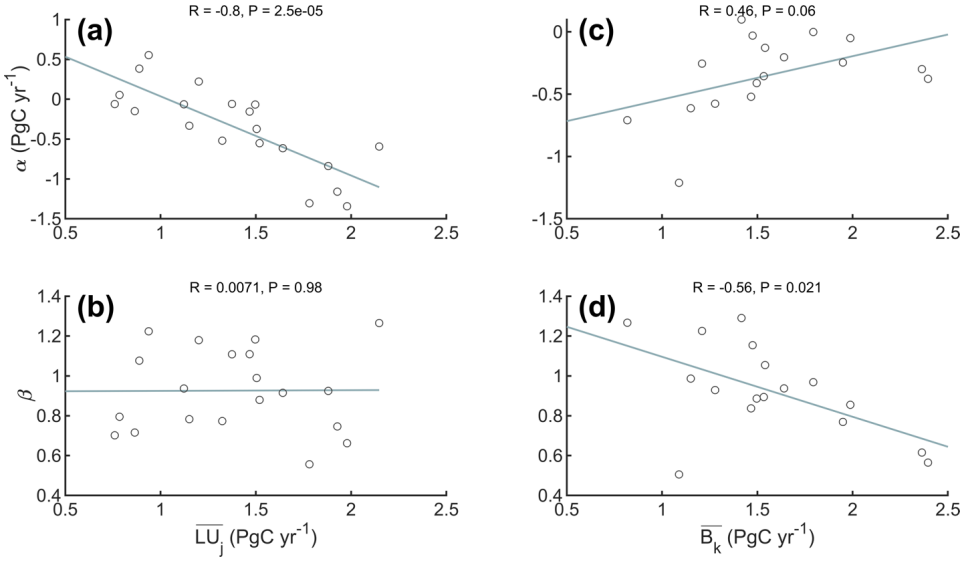

Figure S6. Relationship between i) the 1900-2019 means of LU_j or B_k chosen as input with ii) model-fitted parameters α and β when fit over the 1900-2019 period. R denotes the correlation coefficient and P denotes the p-value for testing the hypothesis that there is no relationship between the x and y variables. The correlation coefficients and p-values are calculated using the MATLAB function *corrcoef* and assume that the x variables in each plot (estimates of LU_j or B_k) are independent. Overbars on $\overline{LU_j}$ and $\overline{B_k}$ denote time averages of LU_j and B_k. Values of α and β are averaged across the 10,000-member ensembles for each choice of LU (no fixed B) or the ~11,000 runs for each choice of B (no fixed LU, B chosen randomly in runs hence inexact ensemble count). Correlation coefficients and p-values for each scatterplot are also listed in Table 2.

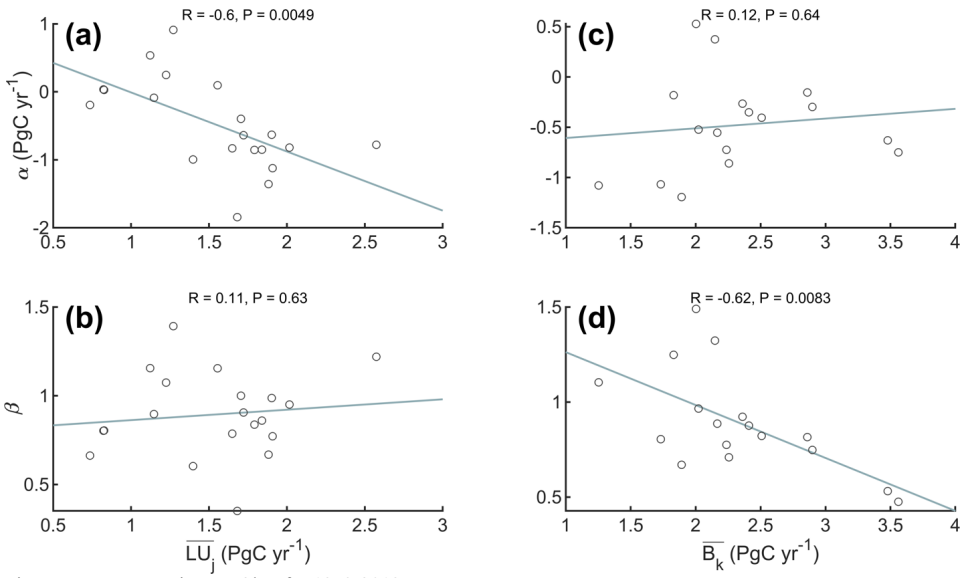

Figure S7. Same as Figure S6 but for 1959-2019.

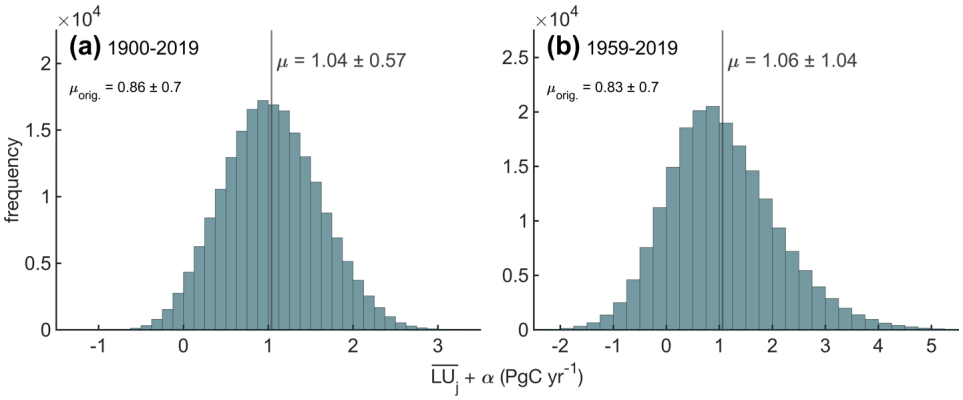

Figure S8. Distributions of $\overline{LU_j}$ + α across the 20-model grouped ensemble (n = 200,000) optimizing over the 1900-2019 (panel (a)) and 1959-2019 (panel (b)) periods. The mean (μ) of each distribution is marked with a grey vertical line with the standard deviation. The means of the original unadjusted land use flux estimates ($\mu_{orig.}$) are also shown.

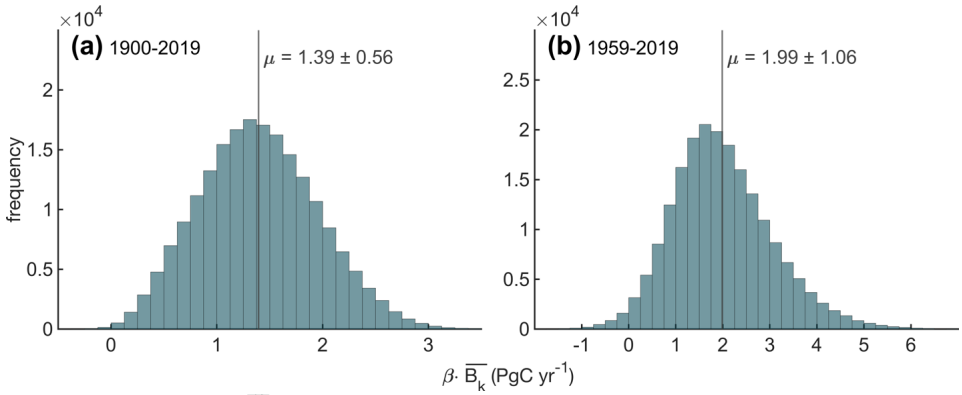

Figure S9. Distributions of $\beta \cdot \overline{B_k}$ across the 20-model grouped ensemble (n = 200,000), where $\beta \cdot B_k$ is optimized to the atmospheric CO_2 growth rate over 1900-2019 (panel (a)) or 1959-2019 (panel (b)). Runs are repeated allowing for variations in the other inputs to account for uncertainty, producing the distributions shown here. The mean (μ) of each distribution is marked with a grey vertical line and labeled with the standard deviation.

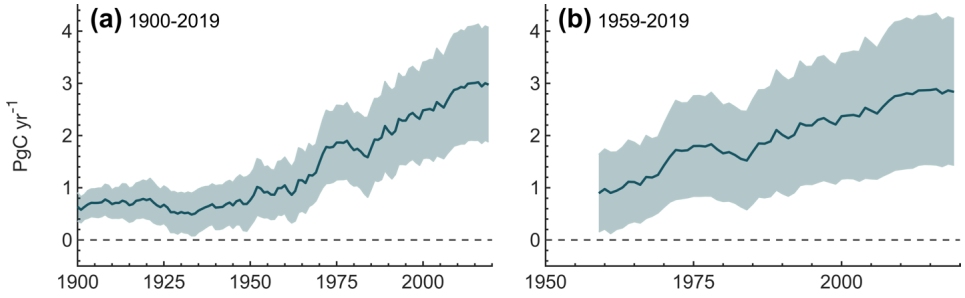

Figure S10. Spread of 200,000 versions of the terrestrial sink $\beta \cdot B_k$ for fitting scenarios of the 20-model grouped ensemble using different estimates of the land use flux as prior. We show the mean (dark teal) ± 1 standard deviation (teal shaded region) of the 200,000 instances of $\beta \cdot B_k$. Each instance of $\beta \cdot B_k$ is optimized to the atmospheric CO_2 growth rate over 1900-2019 (panel (a)) or 1959-2019 (panel (b)).

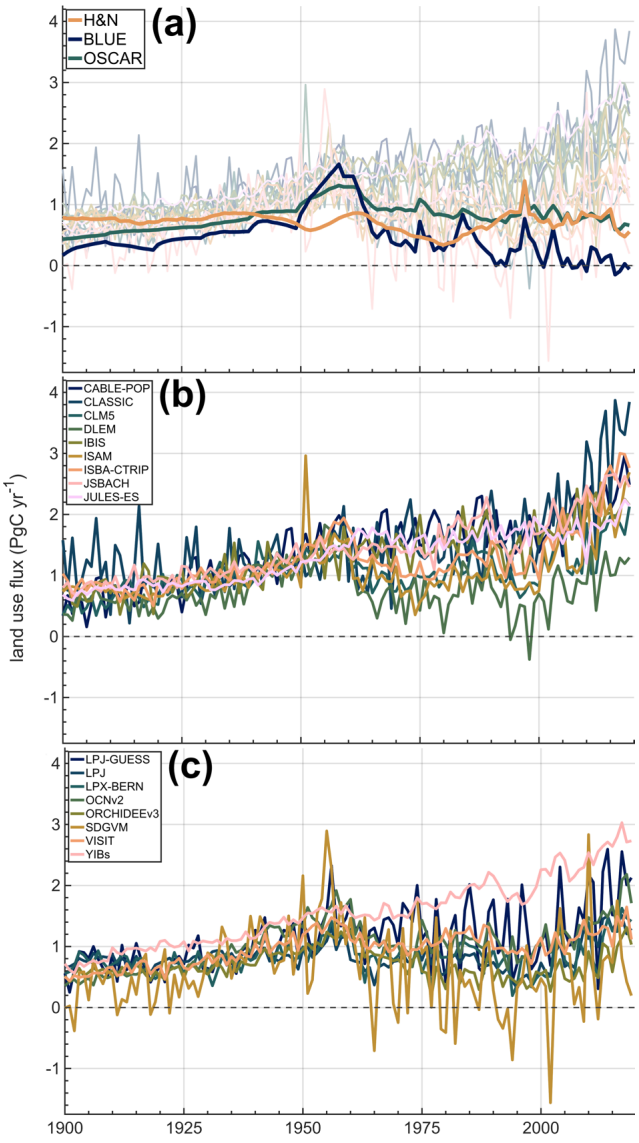

Figure S11. Each of the 20 land use flux estimates used as input with means adjusted to match the values optimized to the atmospheric CO_2 growth rate over 1900-2019 ($\overline{LU_j} + \alpha$). Panel (a) shows adjusted bookkeeping estimates with adjusted DGVM-based estimates shown faintly in the background; panels (b-c) show adjusted individual DGVM-based estimates. Original and optimized means are detailed in Table S1. All data are shown at annual resolution.

Table S1. Original ($\overline{LU_j}$) and optimized ($\overline{LU_j} + \alpha$) mean land use fluxes listed with ensemble average RMSE (Equation 3). $\overline{LU_j}$ is listed only for 1900-2019. Also shown is the ensemble average of the optimized scaling parameter β of each ensemble run multiplying the time average of terrestrial sink $\overline{B_k}$ used in the ensemble run when using each LU_j as input. $\overline{LU_j}$ and RMSE values are shown with ±1 standard deviation of the 10,000-member ensembles. All values are in PgC yr^{-1}.

	References	$\overline{LU_j}$	$\overline{LU_j} + \alpha$		Ensemble-averaged RMSE		$\beta \cdot \overline{B_k}$	
			1900-2019	1959-2019	1900-2019	1959-2019	1900-2019	1959-2019
CONST	N/A	N/A	0.75 ± 0.43	0.74 ± 0.86	0.50	0.40	1.11 ± 0.42	1.66 ± 0.88
H&N	Houghton and Nassikas (2017)	0.86	0.71 ± 0.42	0.85 ± 0.88	0.52	0.46	1.08 ± 0.42	1.78 ± 0.90
BLUE	Hansis et al. (2015)	1.78	0.48 ± 0.42	-0.16 ± 0.79	0.62	0.43	0.84 ± 0.41	0.78 ± 0.81
OSCAR	Gasser et al. (2020)	1.32	0.80 ± 0.45	0.40 ± 0.83	0.59	0.41	1.16 ± 0.44	1.34 ± 0.85
CABLE-POP	Haverd et al. (2018)	1.50	1.43 ± 0.53	1.27 ± 0.92	0.68	0.47	1.78 ± 0.52	2.19 ± 0.93
CLASSIC	Melton et al. (2020)	0.94	1.49 ± 0.51	2.18 ± 1.02	0.63	0.59	1.84 ± 0.50	3.09 ± 1.04
CLM5.0	Lawrence et al. (2019)	1.88	1.04 ± 0.48	1.20 ± 0.91	0.64	0.49	1.40 ± 0.47	2.12 ± 0.93
DLEM	Tian et al. (2015)	1.93	0.77 ± 0.44	0.79 ± 0.87	0.65	0.51	1.13 ± 0.43	1.72 ± 0.89
IBIS	Yuan et al. (2013)	1.38	1.31 ± 0.51	1.31 ± 0.93	0.62	0.46	1.67 ± 0.50	2.22 ± 0.95
ISAM	Meiyappan et al. (2015)	1.12	1.06 ± 0.47	1.47 ± 0.95	0.67	0.58	1.41 ± 0.47	2.39 ± 0.97
ISBA-CTRIP	Delire et al. (2020)	0.89	1.27 ± 0.50	1.66 ± 0.97	0.70	0.63	1.62 ± 0.49	2.58 ± 0.99
JSBACH	Mauritsen et al. (2019)	1.20	1.42 ± 0.52	1.65 ± 0.98	0.62	0.49	1.78 ± 0.51	2.57 ± 0.99
JULES-ES	Sellar et al. (2019)	1.47	1.31 ± 0.51	0.99 ± 0.88	0.60	0.42	1.67 ± 0.50	1.91 ± 0.90
LPJ-GUESS	Smith et al. (2014)	1.50	1.13 ± 0.48	1.08 ± 0.89	0.63	0.51	1.49 ± 0.47	2.01 ± 0.90
LPJ	Poulter et al. (2011)	1.15	0.82 ± 0.44	1.06 ± 0.89	0.56	0.49	1.18 ± 0.43	1.99 ± 0.91
LPX-Bern	Lienert and Joos (2018)	0.78	0.84 ± 0.44	0.86 ± 0.87	0.57	0.46	1.20 ± 0.43	1.78 ± 0.89
OCNv2	Zaehle and Friend (2010)	1.64	1.03 ± 0.48	0.94 ± 0.88	0.69	0.50	1.38 ± 0.47	1.86 ± 0.90
ORCHIDEE-v3	Vuichard et al. (2019)	0.76	0.70 ± 0.43	0.54 ± 0.84	0.59	0.48	1.06 ± 0.42	1.47 ± 0.86
SDGVM	Walker et al. (2017)	1.98	0.64 ± 0.43	0.52 ± 0.84	0.70	0.53	1.00 ± 0.42	1.47 ± 0.86
VISIT	Kato et al. (2013)	1.52	0.97 ± 0.47	0.82 ± 0.87	0.61	0.43	1.33 ± 0.46	1.75 ± 0.89
YIBs	Yue and Unger (2015)	2.15	1.55 ± 0.55	1.80 ± 0.99	0.64	0.47	1.91 ± 0.54	2.71 ± 1.01

Table S2. Average terrestrial CO_2 sink over two time frames, both directly estimated from models (B) and inferred as the residual of the global carbon budget (B_{res}). The GCP estimate of B is the 17-model mean terrestrial sink reported in Friedlingstein et al. (2020). The GCP estimate of B_{res} is calculated as the residual of the budget terms (AGR, FF, O, LU) reported in Friedlingstein et al. (2020). B estimated in this study is based on the average and standard deviation of $\beta \cdot B_k$ across the 20*10,000 ensemble runs (Section 2.3). B_{res} for this study is calculated as the residual across the same optimized ensembles. Estimates from 1900-2019 and 1959-2019 were calculated from fits over the same periods. All values are in PgC yr^{-1}.

		1900-2019	1959-2019
B	this study ($\beta \cdot \overline{B_k}$)	1.39 ± 0.56	1.99 ± 1.05
	GCP 2020 (multi-model mean)	1.57 ± 0.43	2.35 ± 0.60
B_{res}	this study	1.39 ± 0.56	1.99 ± 1.06
	GCP 2020	1.79 ± 0.36	2.34 ± 0.40

CHAPTER 2: Insights from seawater isotopic carbon observations into coral reef metabolism and community function

1 Introduction

As rising atmospheric CO_2 levels induce changes in ocean conditions, including rising temperatures and declining dissolved oxygen concentrations and pH, marine ecosystems around the world are expected to undergo shifts in community structure and diversity (Doney et al., 2009; Poloczanska et al., 2013). In coral reef ecosystems, a shift in community structure from calcifying taxa such as corals towards algal-dominance is expected under high-pCO_2 and low-pH conditions (Agostini et al., 2018; Andersson and Gledhill, 2013; Contreras-Silva et al., 2020; Enochs et al., 2015; Fabricius et al., 2011). Among other changes, an algae-dominant reef system will be depleted in habitat provided by calcium carbonate structures and will have major implications for the ecosystem services coral reefs provide, such as coastline protection and revenue generated through tourism and fishing (Costanza et al., 2014). Planning and adaptation to mitigate damage stemming from declines in these services will be required.

At present, the biogeochemical state of coral reef ecosystem function is frequently described using measurements of seawater dissolved inorganic carbon (DIC) and total alkalinity (TA) (Chisholm and Gattuso, 1991; Cyronak et al., 2018; Smith, 1973; Suzuki and Kawahata, 2003; Watanabe et al., 2006). These measurements provide insight into reef metabolism and signal shifts in the state of the ecosystem, for example between net calcification and net dissolution (Courtney et al., 2018; Cyronak et al., 2018; DeCarlo et al., 2017; Kayanne et al., 2005; Muehllehner et al., 2016; Suzuki and Kawahata, 2003). However, these measurements alone provide no information about which and how much the different major taxa on a reef (e.g., coral, coralline

algae, macroalgae, seagrass) contribute to the inorganic and organic carbon cycles as well as to the overall reef metabolism. Having additional chemical tracers that can elucidate coral reef ecosystem composition and function will be valuable for tracking reef-scale shifts in community function under changing ocean conditions.

Measurements of bulk seawater δ^{13}C-DIC may provide functional group-level information about reef metabolism. During photosynthesis, ^{12}C is more readily taken up by plants than the heavier ^{13}C isotope (Park and Epstein, 1961; Vogel, 1980), with the preferential uptake reported in per mil (‰) difference. This phenomenon, called isotopic fractionation, results in the generated organic material having a different ratio of heavy to light carbon isotopes than the source material and alters the isotopic composition of the source material in the process. The degree to which carbon is fractionated in such a process is represented by a fractionation factor α, defined as:

$$\alpha = \frac{R_A}{R_B}$$

where A is the reactants and B is the products and,

$$R = \frac{^{13}C}{^{12}C}$$

This expression can be rewritten to give the more commonly utilized “fractionation factor,” ε:

$$\varepsilon \approx (\alpha - 1) * 1000$$

Values of ε differ among major taxa and plant types depending on their pathways for carbon uptake and forms of inorganic carbon assimilated (Maslin and Thomas, 2003; O’Leary, 1988; Smith and Epstein, 1971; Vogel, 1993). DIC in seawater, which serves as the source of carbon to photosynthetic primary producers, has an isotopic

composition that typically ranges between -1 and 2 ‰ (Kroopnick, 1985). Relative to the isotopic composition of seawater DIC, photosynthetic taxa that rely on passive diffusion of CO_2 into cells produce organic matter that is ~10 to 40 ‰ depleted in the heavier ^{13}C isotope (Carvalho et al., 2015; Riebesell and Wolf-Gladrow, 1995). Some marine taxa have evolved to utilize carbon concentrating mechanisms, which allow for the use of HCO_3^- ions in photosynthesis, producing organic matter with an isotopic composition of carbon that is more similar to the source seawater (~0 to 30 ‰ depleted in ^{13}C relative to the surrounding seawater) (Sharkey and Berry, 1985). Many marine taxa employ a combination of CO_2 and HCO_3^- uptake during photosynthesis, resulting in an intermediate (~10 to 30 ‰) depletion in ^{13}C of produced organic carbon relative to the source material (Bidwell and McLachlan, 1985; Close and Henderson, 2020; Giordano et al., 2005; Hemminga and Mateo, 1996; Raven et al., 2002; Sand-Jensen and Gordon, 1984; Wilkes and Pearson, 2019). The isotopic signature of calcium carbonate structures in corals has been shown to be close to that of the surrounding seawater (Emrich et al., 1970; Gischler et al., 2009; Smith et al., 1985; Turner, 1982), indicating that the fractionation associated with carbon assimilation during calcification is low compared to that during marine photosynthesis.

Fractionation factors can be considered on an ecosystem-wide scale, summing the metabolic contributions of all taxa present. Koweek et al., (2019) used this principle to show that the community fractionation factor, hereafter "ε_{OM}", for different sections of a reef flat off the Great Barrier Reef reflected the composition of the underlying benthos. They estimated local ε_{OM} using the expression:

$$\varepsilon_{OM}\left(\Delta DIC - \frac{\Delta TA}{2}\right) = DIC_0 * \Delta\delta^{13}C_{DIC} - \left(\frac{\Delta TA}{2}\right) * \varepsilon_{CaCO3} \quad (1)$$

where DIC_0 is the DIC concentration of the water entering a reef section, Δ implying the change in each parameter from that of the incoming water (outside of the reef flat section being studied for Koweek et al. (2019), offshore for this study), $\delta^{13}C$-DIC is the carbon isotopic composition of seawater (notation described in Methods), and ε_{CaCO3} is the assumed fractionation factor associated with calcium carbonate precipitation. Koweek et al. (2019) showed that signals of benthic community composition could be detected in $\delta^{13}C$-DIC measurements, with greater changes in seawater $\delta^{13}C$-DIC occurring in a region of higher non-calcifying algae abundance compared to a region with a greater proportion of corals and calcifying algae, which in net (considering both organic matter and calcium carbonate production) fractionate carbon relatively weakly (Heikoop et al., 2000). As such, changes in ε_{OM} may illuminate shifts in the relative proportions of calcification and primary production contributing to overall reef metabolism. ε_{OM} may also be able to illuminate shifts in community structure not only relating to the balance of calcification and photosynthesis in overall reef metabolism but also among photosynthetic taxa employing different methods of inorganic carbon uptake.

The $\delta^{13}C$ of particulate organic carbon (POC) in reef seawater is another parameter that integrates the metabolic contributions from taxa on the reef while retaining links to the contributing major taxa. POC is technically defined as organic carbon that does not pass through a given filter (usually 0.5 to 0.7 microns) and can comprise phytoplankton, zooplankton bacteria, plant matter and other organic detritus (Close and Henderson, 2020; Volkman and Tanoue, 2002). In the case of reef ecosystems, POC can also come from external sources, such as oceanic inputs,

terrestrial runoff, or sewage (Lamb-Wozniak, 2008; Smith et al., 1981). Although the isotopic composition of the source material for POC is determined by a variety of factors including physiological differences among organisms (Laws et al., 1995; Popp et al., 1998) and ambient conditions (e.g., DIC (Popp et al., 1989; Rau et al., 1991a), temperature (Sackett et al., 1965; Sarmiento, 2013)), major taxa groupings tend to retain characteristic isotopic compositions (Parker, 1964; Rodelli et al., 1984; Sackett and Thompson, 1963; Shultz and Calder, 1976), such as terrestrially-derived POC spanning 20 to 30 ‰ depletion in ^{13}C (Fry, 2002; Haines and Montague, 1979; Smith et al., 1985; Williams and Gordon, 1970), marine phytoplankton 20 to 28 ‰ (Briand et al., 2015; France, 1995; Lamb-Wozniak, 2008; Sackett et al., 1965), macroalgae 10 to 20 ‰ (Lamb and Swart, 2008; Raven et al., 1995; Smith et al., 1985), and seagrass 3.5 to 15 ‰ (Briand et al., 2015; Ostrom and Fry, 1993). Thus observations of POC isotopic composition have been used to broadly characterize the sources and magnitude of organic matter input to reef ecosystems (Cao et al., 2015; Haines and Montague, 1979; Smith et al., 1985; Tuerena et al., 2019; Wissel et al., 2005; Zanden and Rasmussen, 2001).

In this study we present and combine $\delta^{13}C$-POC and $\delta^{13}C$-DIC measurements from spatial surveys with measurements of POC, dissolved organic carbon (DOC), total organic carbon (TOC), particulate organic nitrogen (PON), and $\delta^{15}N$-PON to characterize carbon cycling on a barrier reef in Kāne'ohe Bay, Hawai'i and a fringing reef in Okinawa, Japan. We explore the information about reef structure that can be derived from these observations and more broadly interpret these data in the context of carbon cycling on the reef. Observations of POC, PON, and $\delta^{15}N$-PON can provide

information about the influence of marine vs. terrestrial sources of organic matter to the reef, while TOC and DOC can further provide insights into organic carbon cycling in the reef ecosystems. We include DIC and TA data collected on these reefs, though we limit our discussion of these parameters to estimating a reef-wide organic matter production fractionation factor and quantifying the relative importance of primary production vs. that of calcification on these two reefs. More in-depth analysis of trends in DIC and TA are presented in other work (Kekuewa et al., *in prep.*). We also carry out measurements of seawater salinity, sea surface temperature, and dissolved oxygen concentrations, which we report here but do not discuss. The data we present and their subsequent discussion serve to illuminate the current metabolic landscape and provide data for tracking changes in the community function of these two reef ecosystems.

2 Methods

Seawater samples were collected on a barrier reef in Kāne'ohe Bay, Hawai'i, USA (21°27'46.9"N 157°48'58.8"W) on November 12, 2016 (Courtney et al., 2018) and on a fringing reef near Onna-son, Okinawa, Japan (26.449720°N, 127.794245°E) on October 17, 21, and 22, 2019 (Kekuewa, et al., *in prep*; Rintoul et al., 2022).

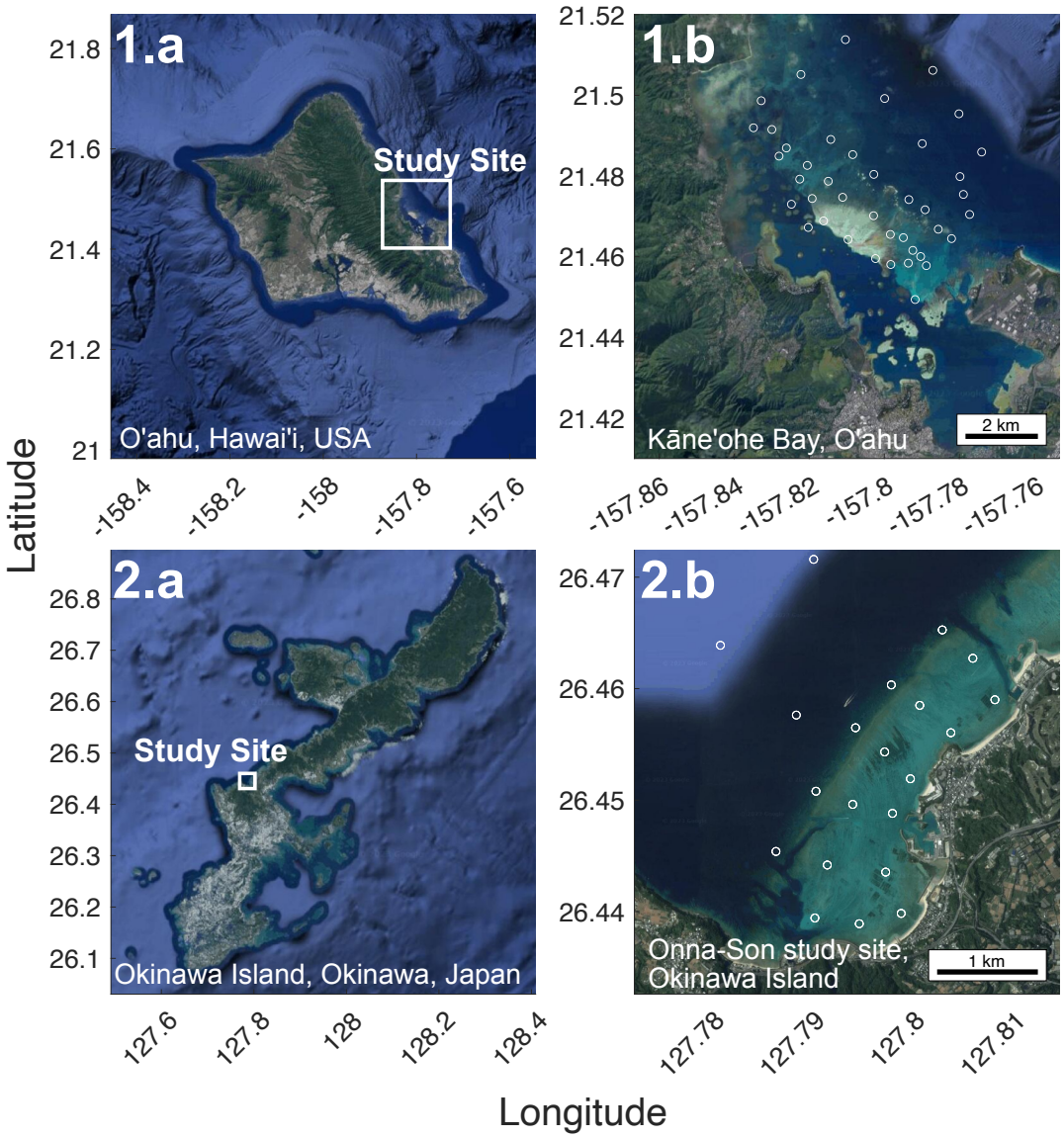

Figure 2.1 Study sites in Kāne'ohe Bay, Hawai'i (1.a, b) and Onna-Son, Okinawa, Japan (2.a, b) with sampling stations marked by white circles. Satellite images source: Google Earth.

2.1 Study site description

Okinawa

The Okinawa study site (Figure 2.1 (2.a, b)), which lies on the central western edge of the main island of Okinawa, encompasses a 3 km along-coast and 1.5 km wide fringing reef area consisting of a forereef, reef flat, and lagoon. The fore reef, characterized by steep spur and groove formations, crests at a pavement reef flat of approximately 2.8 km by 150 m and 1.3 m deep. Crustose coralline algae (CCA), sand, and small chunks of rubble and turf algae cover the reef flat pavement. The lagoon extends between the reef flat and the coastline, ranging from 750 m to 1.35 km in width and 3 to 4 m in depth. The shallow lagoon floor is mostly sand, with some coral rubble in the deep lagoon, and small patch reefs and “coral farms” (areas in which captive-raised corals are mounted on artificial structures) and are scattered across the deep lagoon.

The lagoon drains to the open ocean through several channels, the two largest of which frame the basin in the north and south. The northern channel is ~100 m wide and ~12-15 m deep, while the southern channel consists of a network of deeper channels (>20 m deep), with the network ranging from 200 to 500 m in width. A smaller, artificial channel (~5 m) crosses the center of the lagoon to allow boats in the Maeganeku fishing port to exit the reef. The residence time of seawater on this reef has not yet been quantified.

Kāne’ohe Bay

The Kāne’ohe Bay barrier reef study site (Figure 2.1 (1.a, b)), located on the eastern shore of O’ahu, Hawai’i, spans a 6.1 km by 2 km area consisting of a reef crest,

a highly productive hard-bottom reef flat, a sand reef flat and a lagoon. Coral covers 5-20% of the reef flat area (Franklin et al., 2013), with the remaining benthos comprising sand, coral rubble, and volcanic rock covered in benthic algae including CCA, *Halimeda* spp. and turf algae, interspersed between the coral (Jokiel, 1991; Smith et al., 1981). The shallow sandbar Ahu'olaka sits between the estuarine bay and the barrier reef. Low flow, or "quiet-water," corals make up a fringing reef that lines the shore and the patch reefs that dot the lagoon (Smith et al., 1981). Kāne'ohe Bay is subject to strong terrestrial inputs due to the deltas feeding the Bay and anthropogenic inputs from a population of nearly 40,000 to the south of the Bay (U.S. Census Bureau, 2020). Waves, with secondary effects from wind and tides, are the primary driver of water circulation in the bay, forcing flow toward shore over the barrier reef flat (Jokiel, 1991; Lowe et al., 2009; Smith et al., 1981). Two channels at the northern and southern termini of the reef flat (5-10 m and 10-20 m deep, respectively), of which the northern channel has been directly dredged for ship transit, allow for recirculation of water in the bay to the open ocean. The residence time of the water in Kāne'ohe Bay varies depending on the location, with residence time ranging between one to several days on the reef flat and over one month in the southern lagoon (Lowe et al., 2009).

2.2 Predominant environmental conditions during study

Okinawa

During the four surveys, daytime mean and maximum PAR (recorded by a sensor moored at 0.8 m depth on the reef flat) was 589.27 and 1538 μmol m^{-2} s^{-1} on

October 17, 717 and 1328 μmol m^{-2} s^{-1} on October 21, and 574 and 1562 μmol m^{-2} s^{-1} on October 22 (Rintoul et al., 2022).

Lateral circulation of seawater on the reef as captured by drifter and sensor measurements was <15 cm s^{-1} on October 17 and 22, and >15 cm s^{-1} on October 21 (Rintoul et al., 2022). On October 21, the drifter tracks followed the benthic pattern visible in satellite imagery (Figure 2.1 (2.b)), flowing from the reef crest towards shore and tracing the northern and southern circulation cells towards the channel outlets. On October 17 and 22, drifters deployed at the reef crest traversed a considerably lesser distance than on October 21 before turning back towards and over the reef crest (Rintoul et al., 2022).

Kāne'ohe Bay

On November 12, PAR as recorded by a sensor moored at Station 24 (Figure 2.5) at 1.8 m depth was moderate (maximum ~500 μmol m^{-2} s^{-1}) relative to brighter days that month (max 1206 μmol m^{-2} s^{-1}) (Page et al., 2019).

Current speed data show that water flowing from the ocean into the bay diverges at the southeast channel into southeast- and southwest-flowing currents, which was confirmed by nearby drifter deployments (Page et al., 2019). The strength of the currents in the southwest direction were generally weaker than the currents in the southeast direction over the course of the month in November 2016, with the current speeds varying mainly between 0 – 20 cm s^{-1} and never exceeding 30 cm s^{-1}.

2.3 Seawater sampling

In Okinawa, four spatial surveys were conducted across three days (Table 2.1). Seawater samples for DOC and TOC analysis were collected at all sampling stations, and samples for POM analysis were collected at five stations on each sampling day. Seawater samples for inorganic carbon analysis were also collected using a 5 L Niskin bottle (General Oceanics) at the sea surface (0.5 – 1.0 m depth) to fill 250 mL Pyrex glass bottles (Kekuewa, et al., *in prep*). 60 mL Pyrex glass bottles were also filled from the 5 L Niskin bottle deployment during the October 17 2019 spatial surveys for δ^{13}C-DIC analysis.

Table 2.1 Schedule of spatial surveys conducted in Kāne'ohe Bay and Okinawa.

Location	Date	Morning	Afternoon
Kāne'ohe Bay	November 12, 2016	9:33– 16:18	
Okinawa	October 17, 2019	8:50 – 11:25	14:29 – 16:23
Okinawa	October 21, 2019		13:44 – 15:27
Okinawa	October 22, 2019		12:52 – 14:42

In Kāne'ohe Bay, a single spatial survey was conducted on November 12, 2016 (Table 2.1). Seawater samples for DOC, TOC, and POM analysis were collected at 14 of the 41 stations. Seawater samples for inorganic carbon analysis were collected by submerging 250 mL sample bottles to 0.25 m depth (Courtney et al., 2018). No seawater samples were collected for δ^{13}C-DIC analysis.

Seawater samples for organic carbon analysis were collected using 5 L plastic carboys that had been prepared via acid-rinsing to remove organic carbon. For DOC and TOC collection, two 40 mL glass vials were filled from a carboy at each site. The

vial for TOC analysis was filled directly from the carboy while the vial for DOC analysis was filled with water that had passed through a pre-combusted 47 mm GF/F glass microfiber filter (WHA1825047, Whatman®) attached to the carboy spigot. Two drops of 31% Ultrapur™-grade hydrochloric acid (18078-1B, Kanto Chemical Co., Inc.) in Okinawa and trace metal-grade 37% p.a. hydrochloric acid (J.T.Baker®) at Kāne'ohe Bay was added to each sample. The GF/F filter was replaced every 10 samples. For particulate organic matter (POM) analysis, the carboys for organic matter analysis were filled each day and transported to a laboratory in a cooler for filtration. 3 L of water was passed through a pre-combusted 25 mm GF/F glass microfiber filter (WHA1825025, Whatman®) using a peristaltic pump. The filters were then folded, wrapped in aluminum foil, and stored in a -80˚C freezer before being transported to California on dry ice for analysis. At both sites, inorganic carbon seawater samples were immediately poisoned with 100 µL of a saturated $HgCl_2$ solution following (Dickson et al., 2007) for DIC and TA analysis. *In-situ* measurements of temperature, salinity, and dissolved oxygen (DO) were made using a YSI Professional Plus (± 0.28 ˚C, ± 1%, and ± 6.25 µmol L^{-1} accuracy for temperature, salinity, and DO, respectively) (YSI Inc. / Xylem Inc.) in In Kāne'ohe Bay and a YSI 556 Handheld Multiparameter Instrument (± 0.15˚C, ± 1%, and ± 6.25 µmol L^{-1} accuracy for temperature, salinity, and DO, respectively) (YSI Inc. / Xylem Inc.) in Okinawa.

2.4 Analytical methods

TOC and DOC sample vials were analyzed using a Shimadzu TOC-V_{WP} Wet Oxidation TOC Analyzer (Shimadzu Scientific Instruments) as described in (Koester et

al., 2022). POM samples were thawed, acid fumed, desiccated, baked at 60˚ C, weighed, and packaged before sending to the University of California, Davis Stable Isotope Facility for analysis (detailed preparation protocol can be found at cce.lternet.edu/research). POC concentration, δ^{13}C-POC, PON concentration, and δ^{15}-N-PON were quantified using an elemental analyzer interfaced with a continuous flow IRMS.

Analyses of seawater samples for DIC and TA are reported in (Courtney et al., 2018) and (Kekuewa, et al., *in prep*). Briefly, DIC was analyzed using an Automated Infra-Red Inorganic Carbon Analyzer (Marianda) with a LI-COR 7000 (LI-COR Biosciences) for carbon detection. TA was measured using an open-cell potentiometric acid titration system developed in the Dickson lab at Scripps (Dickson et al., 2007). For Kāne'ohe Bay and Okinawa samples, the accuracy was quantified as the mean offset (listed here ± 1 SD) from Certified Reference Materials bottles provided by the Dickson group. The accuracy for TA and DIC in Kāne'ohe Bay were 1.3 ± 1.3 μmol kg^{-1} and 1.6 ± 1.4 μmol kg^{-1}, respectively (n not available), and for Okinawa were 0.01 ± 2.06 μmol kg^{-1} (n = 14) and 0.7 ± 2.19 μmol kg^{-1} (n = 28), respectively.

Seawater samples in 60 mL bottles were prepared for δ^{13}C-DIC analysis using the gas vacuum-extraction system developed in the Scripps CO_2 group (Lueker et al., 2020). Delta notation (δ) refers to the ratio of abundant to rare isotope in a sample compared to in a standard, expressed as follows in units of per mil (‰), using the example of carbon isotopes:

$$\delta^{13}C(‰) = \left(\frac{\left({}^{13}C/{}_{12}C\right)_{sample}}{\left({}^{13}C/{}_{12}C\right)_{standard}} - 1 \right) * 1000$$

For nitrogen isotopes, ^{15}N content is compared to ^{14}N. For carbon delta notation, the standard Pee Dee Belemnite is used, for nitrogen isotopes, air, and for oxygen, Vienna Mean Standard Ocean Water. For stable isotope analysis of carbon and oxygen in DIC, a subsample of seawater is acidified to convert all DIC species to CO_2. The CO_2 is then isolated using cryogenic traps and transferred into a glass vial under vacuum for subsequent analysis. Stable isotope measurements of the isolated CO_2 were made using a dual-inlet Optima isotope ratio mass spectrometer (IRMS) (Optima Machinery Corporation).

2.5 Flagging $\delta^{13}C$-DIC data

Upon analysis, it was revealed that the seawater in 10 of the 40 total samples collected in 60 mL bottles in Okinawa may have been contaminated. The grease in the stoppers containing many of the bottles contained streaks that may have allowed the headspace in the sample bottle to exchange with ambient air. While most samples had DIC that differed from the duplicate 250 mL bottles (collected from the same Niskin fill) by 0 – 40 μmol kg^{-1} (with the 60 mL bottles having on average 10.5 ± 7.5 μmol kg^{-1} higher DIC than the 250 mL bottles), 10 60 mL samples showed deviations of 80 – 180 μmol kg^{-1} from the 250 mL bottle duplicates (Figure 2.2). Further, these 10 samples had relatively negative values of $\delta^{13}C$-DIC (-1.5 – -0.2 ‰, compared to 0 – 0.8 ‰ for the samples that more closely matched the 250 mL bottle DIC values). These 10 samples are excluded from the analysis in this study.

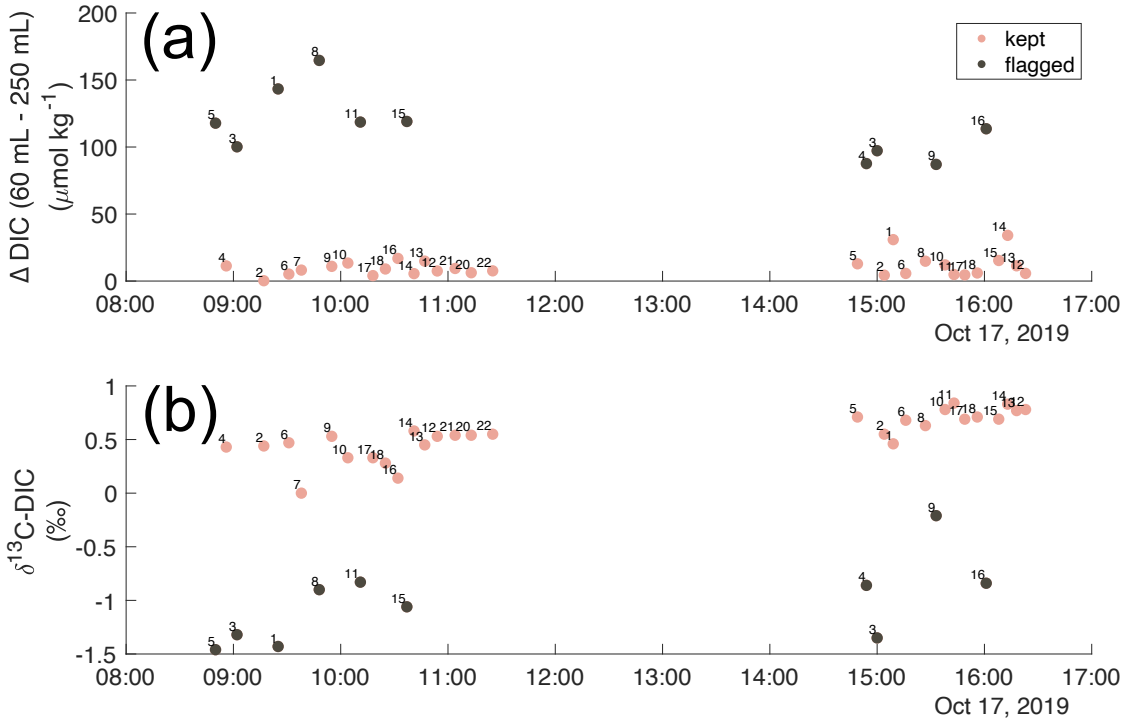

Figure 2.2 Indicators of contamination of 60 mL seawater samples collected in Okinawa on October 17; (a) the difference between the measured DIC for the 60 mL samples and the 250 mL samples collected in duplicate from the same Niskin bottle are plotted against the time of sample collection. (b) δ^{13}C-DIC of 60 mL seawater samples. Each marker is labeled with the number of the station at which the sample was collected (Figure 2.5). Marker color separates data that was included in the study (pink) and excluded (purple). We use the color map turku (Crameri, 2021) in this study to prevent visual distortion of the data and to make this work accessible to readers with differing color vision (Crameri et al., 2020).

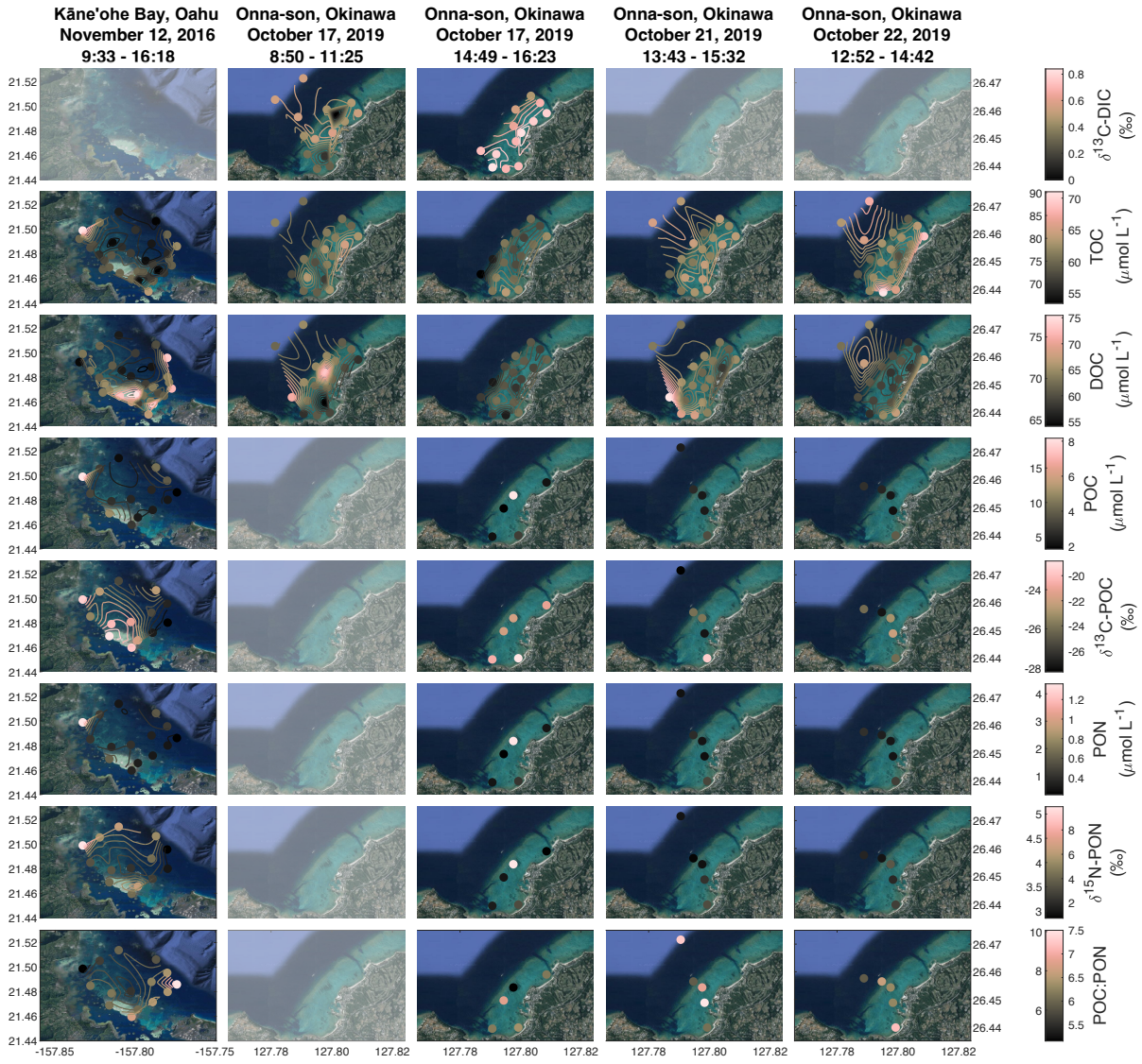

Figure 2.3 Spatial variability in δ^{13}C-DIC, TOC, DOC and POM parameters (POC, δ^{13}C-POC, PON, δ^{15}N-PON, POC:PON) in Kāne'ohe Bay for November 12, 2016, and Okinawa for October 17, 21, and 22, 2019. Tick labels on the left side of the color bar show color values for the Kāne'ohe Bay plot, and on the right side for the Okinawa plots. Color bar scaling is universal across the four Okinawa plots for a given parameter. Contour lines appear at intervals of 0.05 ‰ (δ^{13}C-DIC, Okinawa only), 2 and 1 μmol L^{-1} (TOC), 1.5 and 1 μmol L^{-1} (DOC), and 1.5 μmol L^{-1} (POC), for Kāne'ohe Bay and Okinawa, respectively. Contour lines appear at 0.5 ‰ (δ^{13}C-POC), 0.5 μmol L^{-1} (PON), 0.2 ‰ (δ^{15}N-PON), and 0.5 (POC:PON) for Kāne'ohe Bay.

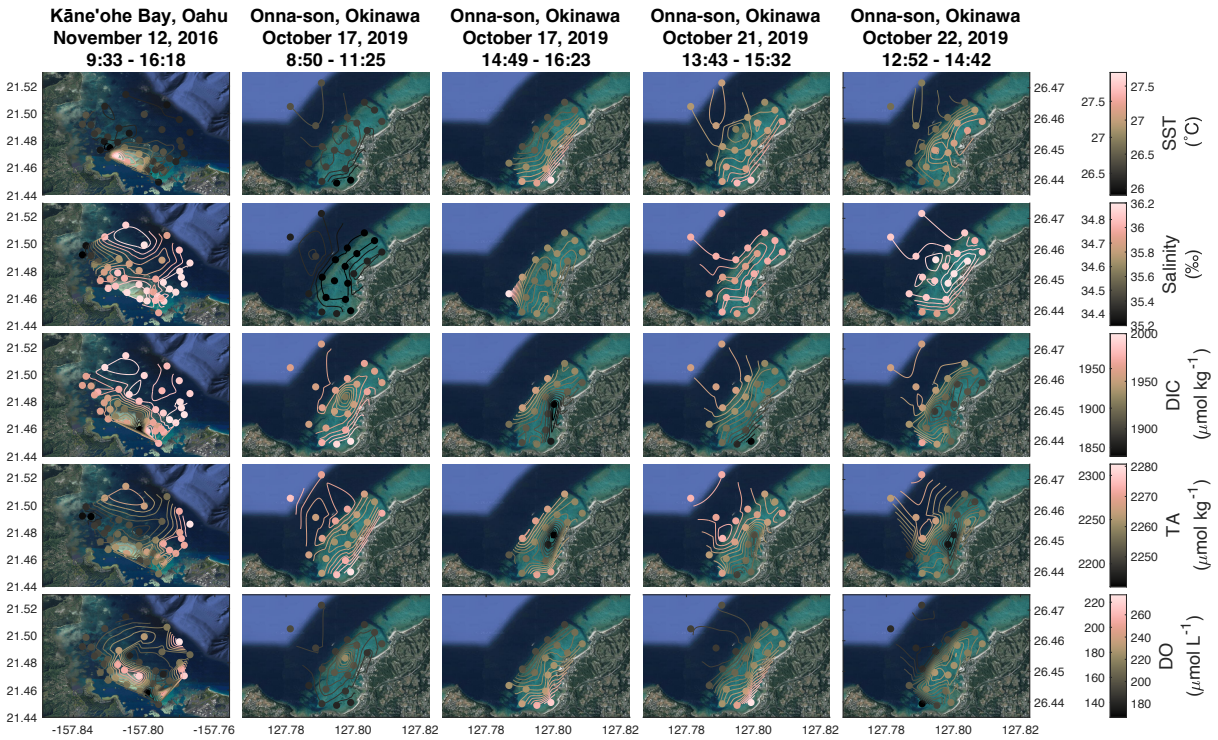

Figure 2.4 Spatial variability in SST, salinity, DIC, TA and DO in Kāne'ohe Bay for November 12, 2016 (Courtney et al., 2018) and Okinawa for October 17, 21, and 22, 2019 (Kekuewa, et al., *in prep*). Tick labels on the left side of the color bar show color values for the Kāne'ohe Bay plot and on the right side for the Okinawa plots. Color bar scaling is universal across the four Okinawa plots for a given parameter. Grid cells are tinted white for surveys in which the data of interest was not collected. Flagged $\delta^{13}C$-DIC data are not shown. Contour lines appear at intervals of 0.2 and 0.1 ˚C (SST), 0.05 and 0.05 ‰ (salinity), 15 and 7.5 μmol kg^{-1} (DIC), 15 and 2.5 μmol kg^{-1} (TA), and 10 and 5 μmol L^{-1} (DO), all for Kāne'ohe Bay and Okinawa, respectively.

3.1 Temperature and salinity conditions

Okinawa

Sea surface temperature (SST) ranged between 25.9 and 27.7 ˚C with an average temperature of 26.7 ˚C ± 0.4 ˚C across the four spatial surveys in Okinawa. The average SST was lowest during the morning survey on October 17 at an average of 26.23 ± 0.1 ˚C. The average temperatures during the October 17, 21, and 22 afternoon surveys were 26.8 ± 0.3 ˚C, 27 ± 0.2 ˚C, and 26.8 ± 0.2 ˚C, respectively. Across the four

surveys in Okinawa, salinity varied between 35.2 and 36.2 ‰ with a mean of 35.8 ± 0.3 ‰ (Figure 2.4). Salinity was lowest in the morning of Oct 17 and increased across the following three spatial surveys (means = 35.2 ± 0.1, 35.7 ± 0.14, 36.0 ± 0.1, 36.1 ± 0.1 ‰, respectively).

Kāne'ohe Bay

Sea surface temperature (SST) ranged between 26.2 and 27.9 ˚C in Kāne'ohe Bay on November 12, with an average SST of 26.6 ± 0.3 ˚C (Figure 2.4). The highest temperatures during the spatial survey were recorded in the shallowest, central part of the reef (with a depth of ~0.5 m, appearing as the central light patch in Figure 2.1 (1.b)), while temperatures elsewhere were lower and generally uniform. Salinity varied between 34.4 and 34.9 ‰, with a mean of 34.8 ± 0.1 ‰.

Table 2.2 Descriptive statistics (mean (± 1SD), range, minimum, and maximum) of observations collected during two of four total spatial surveys in Okinawa, Japan. Offshore values are excluded.

		October 17, 2019 08:50 – 11:25				October 17, 2019 14:29 – 16:23			
		Mean	Range	Min	Max	Mean	Range	Min	Max
δ^{13}C-DIC	(‰)	0.38 ± 0.17	0.58	0	0.58	0.7 ± 0.11	0.38	0.46	0.84
TOC	(μmol L^{-1})	60.8 ± 2.0	7.9	57.1	65.0	59.5 ± 2.6	10.2	53.5	63.7
DOC	(μmol L^{-1})	62.5 ± 4.5	18.9	54.2	73.1	59.8 ± 2.0	7.1	55.7	62.8
POC	(μmol L^{-1})					3.5 ± 2.7	6.3	1.9	8.2
δ^{13}C-POC	(‰)					-20.9 ± 1.3	3.1	-21.9	-18.8
PON	(μmol L^{-1})					0.5 ± 0.5	1.2	0.2	1.4
δ^{15}N-PON	(‰)					3.3 ± 3.8	9.1	0.8	9.9
POC:PON						6.1 ± 0.6	1.6	5.2	6.8
SST	(˚C)	26.3 ± 0.1	0.5	25.9	26.4	26.8 ± 0.3	1.3	26.4	27.7
Salinity	(‰)	35.2 ± 0.1	0.1	35.2	35.3	35.7 ± 0.1	0.6	35.6	36.2
		October 21, 2019 13:44 – 15:27				October 22, 2019 12:52 – 14:42			
		Mean	Range	Min	Max	Mean	Range	Min	Max
TOC	(μmol L^{-1})	62.7 ± 1.5	4.4	60.1	64.5	62.5 ± 3.2	12.6	58.4	71.0
DOC	(μmol L^{-1})	64.6 ± 3.7	17.5	58.0	75.5	60.4 ± 2.9	9.6	57.6	67.2
POC	(μmol L^{-1})	2.7 ± 0.6	1.2	2.3	3.5	2.7 ± 0.8	1.8	2.1	3.9
δ^{13}C-POC	(‰)	-23.7 ± 3.1	7.6	-27.2	-19.6	-24.1 ± 2.2	5.1	-27.2	-22.1
PON	(μmol L^{-1})	0.4 ± 0.1	0.2	0.3	0.5	0.35 ± 0.1	0.2	0.3	0.5
δ^{15}N-PON	(‰)	1.9 ± 1.1	2.3	0.9	3.2	2.4 ± 1.0	2.4	1.2	3.6
POC:PON		6.6 ± 0.7	1.6	5.9	7.5	6.6 ± 0.4	0.9	6.3	7.2
SST	(˚C)	27.0 ± 0.2	0.8	26.7	27.5	26.8 ± 0.2	0.7	26.5	27.2
Salinity	(‰)	36.0 ± 0.1	0.1	35.9	36.0	36.1 ± 0.1	0.3	35.9	36.2

Table 2.3 Descriptive statistics (mean (± 1SD), range, minimum, and maximum) of observations collected during a single spatial survey in Kāne'ohe Bay, Hawai'i, USA.

		November 12, 2016 13:44 – 15:27			
		Mean	Min	Max	Range
TOC	(μmol L^{-1})	72.2 ± 4.7	65.8	90.2	24.4
DOC	(μmol L^{-1})	69.8 ± 3.7	64.8	77.6	12.8
POC	(μmol L^{-1})	7.0 ± 4.1	3.3	19.3	16
δ^{13}C-POC	(‰)	-25.2 ± 1.9	-28.2	-22.5	5.7
PON	(μmol L^{-1})	1.1 ± 1.0	0.3	4.4	4.1
δ^{15}N-PON	(‰)	3.8 ± 0.6	2.9	5.2	2.3
POC:PON		6.8 ± 1.3	4.4	10.1	5.7
SST	(˚C)	26.6 ± 0.3	26.2	27.9	1.7
Salinity	(‰)	34.8 ± 0.1	34.4	34.9	0.5

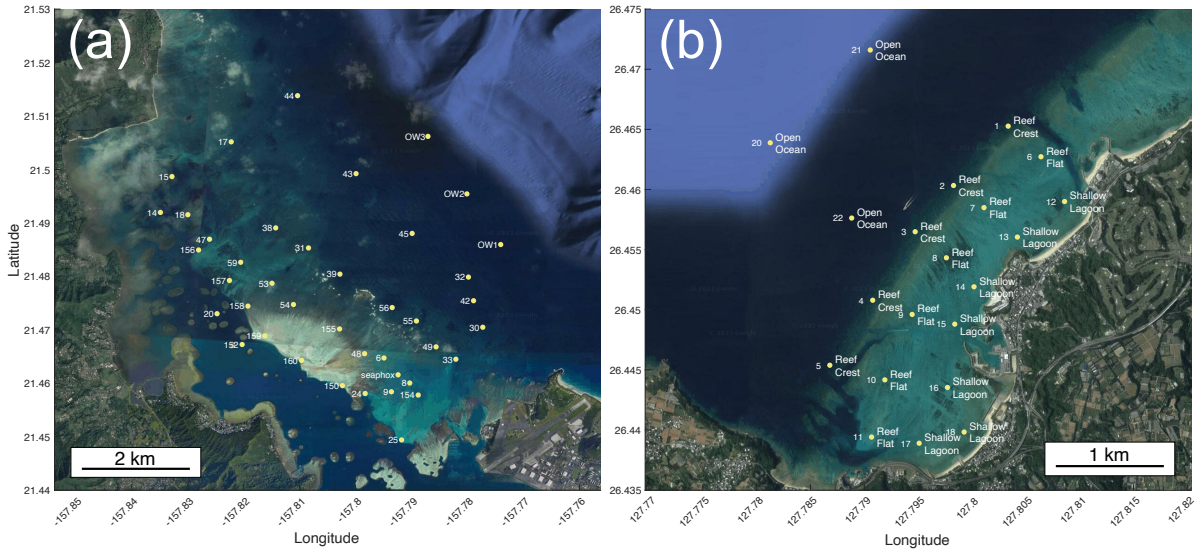

Figure 2.5 Study sites labeled with station number for Kāne'ohe Bay (a) and Okinawa (b). Okinawa stations are also labeled with benthic groupings assignments. Sample stations are grouped according to Kennedy et al. (2021) based on wave exposure, depth, and benthic cover.

3.2 Variability in isotopic and organic matter parameters

Okinawa

Seawater δ^{13}C-DIC was significantly more enriched (two-sample t-test, $p < 0.05$) in the afternoon survey (mean = 0.7 ± 0.11 ‰) than in the morning survey (mean = 0.38 ± 0.17 ‰) on October 17 (Figure 2.3). Within surveys, δ^{13}C-DIC show a gradient between the open ocean and inshore. In the morning survey, δ^{13}C-DIC is the most depleted over the reef flat and deep lagoon (means of 0.33 ± 0.29 ‰ and 0.33 ± 0 ‰ (n = 1) for the reef flat and deep lagoon, respectively), and in the afternoon the deep lagoon and shallow lagoon regions were the most enriched with respect to δ^{13}C (means of 0.81 ± 0.04 ‰ and 0.75 ± 0.06 ‰, respectively).

TOC levels were greatest in the October 21 and 22 surveys (means of 62.7 ± 1.5 μmol L^{-1} and 62.5 ± 3.2 μmol L^{-1}, respectively), although DOC was greater than TOC on October 21 (64.6 ± 3.7 μmol L^{-1} and 62.7 ± 1.5 μmol L^{-1}, respectively) (as well as the October 17 morning survey), suggesting possible contamination of the samples (possible sources of contamination include boat exhaust fumes and engine leakage). The means of the morning and afternoon October 17 DOC observations differ significantly, with the mean DOC being lower in the afternoon survey (means of 62.5 ± 4.5 μmol L^{-1} and 59.8 ± 2.0 μmol L^{-1} for morning and afternoon, respectively), again the morning data were possibly impacted by contamination. The means of the morning and afternoon October 17 TOC observations are not significantly different.

DOC possibly decreases from the open ocean to the shoreline sites in the October 17 and 21 afternoon surveys, but the trend is not obvious. TOC may also show a faint spatial gradient from the open ocean to the shallow lagoon on the same days,

where TOC increases away from the open ocean, but this trend is even less clear than that of DOC and is not consistent across surveys.

δ^{13}C-POC was a maximum in the October 17 afternoon survey (mean = -20.9 ± 1.3 ‰) compared to the October 21 (mean = -23.7 ± 3.1 ‰) and October 22 (mean = -24.1 ± 2.2 ‰). Mean daily PAR was greatest on October 17 out of the survey days, and the October 17 afternoon survey occurred later in the day than the other afternoon surveys. Though the day-to-day differences in δ^{13}C-POC were small, the high irradiance paired with slower circulation time on October 17 likely contributed to greater overall productivity and positive δ^{13}C-POC observations. These observations also coincided with the greatest offshore to inshore decreases in DIC and TA of all the spatial surveys (Kekuewa, et al., *in prep*).

POC and δ^{15}N-PON were also greatest in the October 17 afternoon survey (mean = 3.5 ± 2.7 μmol L and 3.3 ± 3.8 ‰, respectively) but with high variance in both parameters for that day. POC:PON was lower in the October 17 afternoon survey (mean = 6.1 ± 0.6) compared to the other surveys (mean = 6.6 ± 0.7 and 6.6 ± 0.4 for October 21 and 22, respectively).

While POC measurements show no clear spatial trend, δ^{13}C-POC appears to be more negative towards the open ocean (mean of -26 ± 2.4 ‰ across afternoon open ocean observations). PON and δ^{15}N-PON generally increase as the water circulates through the reef, though this gradient is disrupted by an anomalously high-PON high-δ^{15}N-PON measurement (1.4 μmol L^{-1} and 9.9 ‰, respectively) on October 17 in the central shallow lagoon.

Kāne'ohe Bay

Organic carbon and nitrogen observations (DOC, TOC, POC, δ^{13}C-POC, PON, δ^{15}N-PON) in Kāne'ohe Bay tended to have local extrema over the shallowest part of the reef and the northwest end of the reef (Figure 2.3). DOC, POC, and δ^{13}C-POC were largest over the shallowest part of the reef, and TOC, POC, PON, and δ^{15}N-PON were elevated towards the northwest end of the reef. POC:PON was at a minimum in the northwest end of the reef. The largest offshore to onshore changes in DIC appeared to occur over the shallowest portion of the reef (Figure 2.4, (Courtney et al., 2018)).

3.3 Estimation of ε_{OM} in Okinawa

We use δ^{13}C-DIC observations combined with observations of DIC and TA collected in Okinawa (Kekuewa, et al., *in prep*) to estimate the community fractionation factor ε_{OM} (Equation 1). We use the Koweek et al. (2019) mass balance expression and plot $(DIC_0 * \Delta\delta^{13}C_{DIC}) - \left(\frac{\Delta TA}{2}\right) * \epsilon_{CaCO3}$ against $(\Delta DIC - \frac{\Delta TA}{2})$ to obtain ε_{OM} from the slope (Figure 2.6). Using this method, we find ε_{OM} to be between -13.4 and -11 ‰ for the range of ε_{CaCO3} values between -5 and 5 ‰ (per Koweek et al. (2019)). If we divide the data into reef region-based groupings (Figure 2.5) and calculate ε_{OM} for each region assuming 0‰ for ε_{CaCO3}, we find an ε_{OM} of -9.1 ‰ over the reef crest, -7.6 ‰ over the reef flat (excluding an outlier, see Figure 2.6), -16.5 over the deep lagoon and -10 over the shallow lagoon. The slope of data collected over the deep lagoon region shown in Figure 2.6 differs significantly from that of the reef flat and of the shallow lagoon ($p < 0.05$). Otherwise, there are no significant differences between slopes. Including a low

value (marked with a triangle in Figure 2.6) changes the Reef Flat ε_{OM} from -7.6 ‰ to -23.7 ‰.

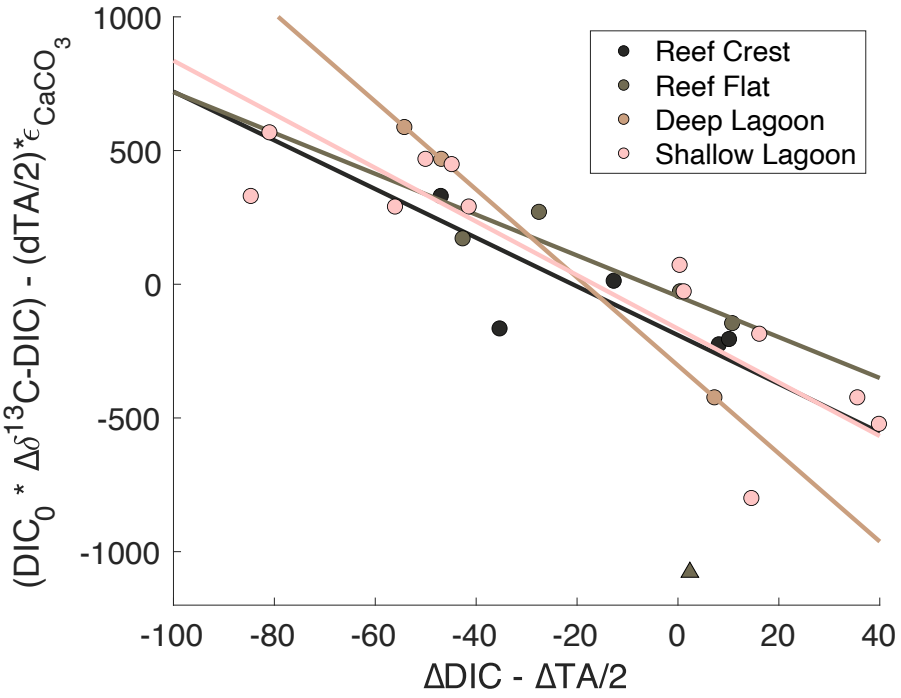

Figure 2.6 Regressions ($DIC_0 * \Delta\delta^{13}C_{DIC}$) – ($\Delta TA/2$) against ($\Delta DIC$-$\Delta TA/2$) per Koweek et al. (2019) for observations in Okinawa separated by region. The slope of each regression provides an estimate of the local community fractionation factor ε_{OM}. The Reef Flat triangle marker datum is excluded from the regression. The community calcification fractionation factor ε_{CaCO3} is assumed to be 0 ‰.

4 Discussion

4.1 Insights from organic matter in Okinawa

Observations of organic carbon and nitrogen in Okinawa can add resolution to the metabolic landscape as described by δ^{13}C-DIC observations. The southernmost δ^{13}C-POC observation collected closest to shore is -18.8, -19.6 and -24.3 ‰ on October 17, 21, and 22, respectively; the relatively depleted δ^{13}C-POC observation on October 22

suggests that terrestrial inputs (δ^{13}C-POC of < -25 ‰) (Lamb-Wozniak, 2008; McNevin et al., 2007; Roeske and O'Leary, 1984; Williams and Gordon, 1970) may be present. This possibility is supported by the anomalous values of DOC, salinity, DIC, and dissolved oxygen observations when compared to the same location in other afternoon surveys (Kekuewa, et al., *in prep*). The POC:PON ratio in the same station is also relatively high, further supporting this theory, as terrestrial organic matter has a characteristically higher ratio of organic C:N than does marine organic matter (~30 to 50 for terrestrial organic matter, ~4 to 10 for marine POM) (Cao et al., 2015; Ertel and Hedges, 1985; Lamb-Wozniak, 2008; Libes, 2011; Redfield, 1963; Thorp et al., 1998)). Reef seawater DOC and TOC levels have been shown to rise in accordance with rates of primary production (Haas et al., 2011; Ziegler and Benner, 1999) and are also associated with the presence of bacterioplankton, which consume DOC and DO (Haas et al., 2011, 2013; Ziegler and Benner, 1999). While some studies report a net consumption of DOC in coral reef ecosystems by microbial communities (Haas et al., 2013; Nelson et al., 2011), spatial trends in DOC and TOC in our surveys are generally too weak to draw conclusions about net production or loss of DOC or TOC.

We also note that δ^{13}C-POC showed a strong negative relationship with DIC in both Okinawa and Kāne'ohe Bay (Figure 2.7 (b,d)). One possible explanation of this relationship is DIC-dependence of fractionation, in which organisms fractionate carbon less in carbon-limited environments (Freeman and Hayes, 1992; Jasper and Hayes, 1994; McCabe, 1985; Popp et al., 1989; Rau et al., 1991a, 1991b). Another possible explanation is that this relationship occurs due to the addition of POC by reef taxa that produce organic matter that is enriched with respect to ^{13}C compared to the initial

seawater entering the reef. Spatial plots of δ^{13}C-POC in Figure 2.3 suggest that seawater δ^{13}C-POC becomes enriched in ^{13}C as seawater transits the reef. As water entering the reef is successively exposed to POC-producing taxa that produce relatively enriched organic carbon, DIC decreases while POC increases (Figure 2.7 (a,b)), and the overall δ^{13}C-POC signature of the seawater will steadily increase. For the Okinawa data, using a community fractionation factor of -12.1 ‰ (assuming ε_{CaCO3} = 0 ‰) and assuming the water entering the reef has a δ^{13}C-POC of -27.5, the seawater with the lowest DIC and δ^{13}C-POC of -19 ‰ comprises ~55% POC produced on the reef and ~44% POC produced outside the reef. The slope of the δ^{13}C-POC vs. DIC relationship is less steep for Kāne'ohe Bay than for Okinawa, suggesting that the POC-producing processes in Kāne'ohe Bay fractionate more strongly than do those in Okinawa, resulting in a lesser overall change in δ^{13}C-POC per unit change in DIC. This interpretation aligns with the notion that organic matter production, which fractionates less strongly than calcification, makes up a larger fraction of overall reef metabolism in Okinawa than in Kāne'ohe Bay. At the least, the systematic change in δ^{13}C-POC with changing DIC clearly indicates that POC is actively being produced on both the Okinawa and Kāne'ohe Bay reefs.

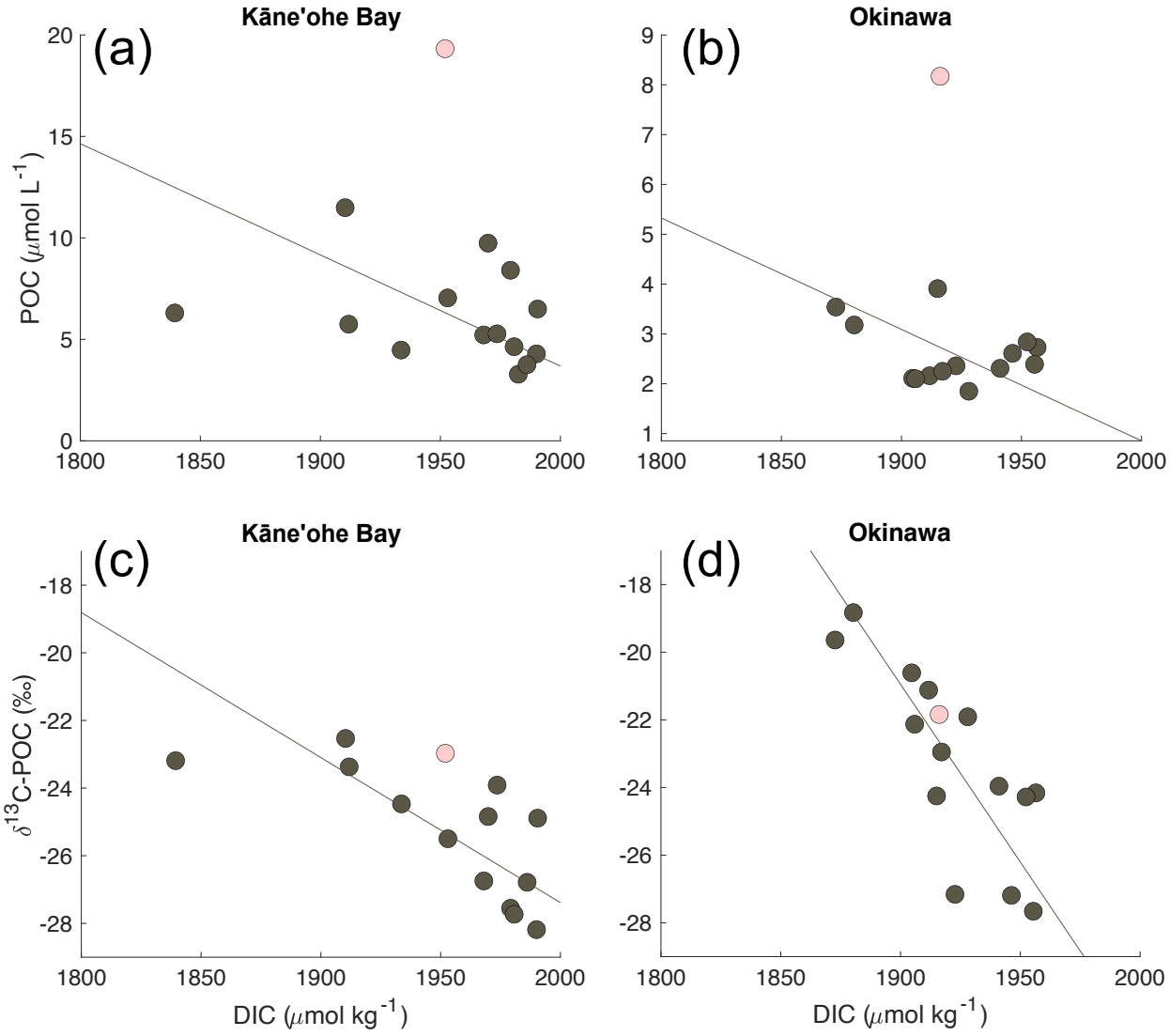

Figure 2.7 Property-property plots of POC vs. DIC and δ^{13}C-POC vs. DIC data from Kāne'ohe Bay (a,c) and Okinawa (b,d). One high-POC outlier in the Kāne'ohe Bay and Okinawa data is marked in pink and excluded from the model-II geometric mean regression fits to each survey's data across all plots. The regressions yield (a) POC = -0.055*DIC + 113 (R^2 = 0.62), (b) POC = -0.022*DIC + 45.6 (R^2 = 0.1), (c) δ^{13}C-POC = -0.043*DIC + 58.4 (R^2 = 0.51), and (d) δ^{13}C-POC = -0.11*DIC + 179 (R^2 = 0.62).

4.2 Insights from organic matter in Kāne'ohe Bay

Although no δ^{13}C-DIC data that would allow characterization of community ε_{OM} was collected in Kāne'ohe Bay, observations of particulate organic matter and their isotopic content can help characterize sources of carbon to the reef and provide broad

information about major taxa metabolism. δ^{13}C-POC is most enriched (~ -22 to -19 ‰) over the shallowest portion of the bay, indicating a strong local influence of marine productivity. DOC, which is linked to production, and TOC are both high in this region, further implying high local production. These signals agree with the high degree of DIC drawdown occurring over this shallow region (Figure 2.4, (Courtney et al., 2018)). Conversely, mean δ^{13}C-POC (-25.2 ± 1.9 ‰) on the reef overall is low compared to offshore values (~ -22 to -20 ‰) (Bauer, 2002; Druffel et al., 1992), suggesting inputs of terrestrial organic carbon, which is in agreement with a previous study of sources of organic matter in Kāne'ohe Bay based on isotopic measurements (Smith et al., 1985).

Observations from a single sampling station in the northwest region of the bay (Station 15) exhibit the maximum values of TOC, POC, δ^{13}C-POC, PON, δ^{15}N-PON and minimum values of C:N of POM, salinity, and TA (Courtney et al., 2018) for the entire spatial survey. Microbial data indicate that this station was the site of a bloom of the photosynthetic prokaryote *Synechococcus* (Köster, personal communication). An excess of *Synechococcus* can explain the high local TOC and POC signals. Regarding δ^{13}C-POC, laboratory studies have suggested differing values of maximum carbon fractionation achieved by *Synechococcus* during photosynthesis during $CO_{2(aq)}$-replete scenarios, including -33 ‰ (Erez et al., 1998), -18 ‰ (Popp et al., 1998) and -17 ‰ (Wilkes and Pearson, 2019). However, another study in which *Synechococcus* was collected off the Scripps Pier (Bertilsson et al., 2003) reported a δ^{13}C-OM of -25 ‰ for the collected *Synechococcus*. According to these studies, fractionation by *Synechococcus* depends on a variety of factors including cell growth rates, surface area, and volume as well as seawater temperature and $CO_{2(aq)}$ concentrations. The

fractionation of carbon by *Synechococcus* appears to be too variable to confidently relate the enriched δ^{13}C-POC signal at this site to the *Synechococcus* bloom. A study of organic nitrogen in marine phytoplankton indicates that nitrogen in *Synechococcus* has a δ^{15}N signature of 5.4 ‰ (Needoba et al., 2003), just above the maximum signal across the survey at this site of 5.15 ‰, supporting the contribution of *Synechococcus* to local organic matter cycling. However, the organic C:N in *Synechococcus* of 7.3 (Bertilsson et al., 2003) is inconsistent with the anomalously low POC:PON observation (4.43) at this site. The low local POC:PON also cannot be explained by terrestrial input, which tends to have a high POC:PON (Lamb-Wozniak, 2008; Sampei and Matsumoto, 2001). However, the low local salinity and high δ^{15}N-PON observations suggest that the bloom is concurrent with terrestrial input to the bay at this site. Inputs to reef systems with relatively low δ^{15}N-PON include nitrogen assimilation and fixation and atmospheric dinitrogen (1 to 3, 0 to 1, and 0 ‰, respectively), while sewage, upwelling, and especially human and animal waste have relatively high signatures (2 to 8, 4 to 7, and 10 to 21‰, respectively) (Cao et al., 2015; Lamb-Wozniak, 2008). The relatively high δ^{15}N-PON suggests that anthropogenic and agricultural waste may be part of the input. The hypothesized terrestrial input in the northwest region of the bay is supported by the finding in Smith et al. (1981) that 60% of the freshwater inputs occurred in the northwest region of the bay. They also found that such inputs can carry elevated levels of particulate organic matter.

δ^{13}C-POC is generally more depleted towards the southeast end of the bay and aligns with higher C:N ratios in the same region, which are indicative of a terrestrial source. On the other hand, δ^{15}N-PON over the southeast region is relatively depleted

compared to the rest of the reef. The observations of low δ^{15}N-PON towards the southeastern end of the bay suggest a diminished influence of urban runoff, which contrasts with the observations of high POC:PON and low δ^{13}C-POC. However, it is possible that terrestrial runoff in the southeastern end is generally low in sewage and waste content such that the runoff imparts a mostly terrestrial but non-urban or agricultural signature in the bay water. The Smith et al. (1981) study on Kāne'ohe Bay after decades of sewage input to the bay was diverted in 1977 showed that overall particulate organic matter content decreased because of the runoff diversion. They recorded that POC fell from over 20 μmol $kg^{-1}$to between 14 and 17 μmol kg^{-1}, and bay-wide PON fell from 2.8 to 2.1 μmol kg^{-1}. Observations in our study of POC (mean of 7.0 ± 4.1 μmol L^{-1}) and PON (mean of 1.1 ± 1.0 μmol L^{-1}) based on a single day of data are both lower than these post-diversion values, possibly indicating that the bay may have continued to recover since the diversion.

Compared to observations collected in Okinawa, observations in Kāne'ohe Bay of POC, PON, and POC:PON are elevated, δ^{13}C-POC relatively depleted and δ^{15}N-PON relatively enriched. These differences suggest that Kāne'ohe Bay receives a greater input from terrestrial runoff, which elevates particulate organic matter and raises the POC:PON ratio further from the Redfield value of 6.6. Such increased runoff also explains the depleted δ^{13}C-POC and enriched δ^{15}N-PON, both of which are characteristic of terrestrial input.

4.3 Insights from ε_{OM} in Okinawa

Estimation of ε_{OM} on the Okinawa (-13.4 to -11 ‰ in this study) reef suggests that primary production on this reef is associated with relatively weak fractionation when compared to regions studied by Smith and Kroopnick (1981) or Koweek et al. (2019) (-16 ‰ to -14 ‰ for the region with lesser calcifier abundance). The relation of changes in TA and DIC (Figure 2.8 (a), Kekuewa, et al., *in prep*)) suggest that metabolism in the Okinawa study site is dominated by primary production, requiring a ~75% contribution to overall metabolism from primary production and a ~25% contribution from calcification. The taxa that contribute to primary production and inhabit the Okinawa reef benthos include corals, brown algae (*Phaeophyceae*), green algae (*Ulvophyceae*), and eelgrass (*Zostera marina).* Eelgrass and other seagrasses fractionate carbon to a lesser degree (their tissues comprising carbon with a $\delta^{13}C$ of -13.5 to -3.5‰ (Bj and Fry, 1987; Briand et al., 2015; Hemminga and Mateo, 1996; Ostrom and Fry, 1993; Smith and Epstein, 1970; Yamamuro, 1999)) than other reef producers. Fractionation in benthic macroalgae is more variable but on average greater, the $\delta^{13}C$ of their tissues ranging between -25 to -7 ‰ (Briand et al., 2015; Lamb-Wozniak, 2008; Ostrom and Fry, 1993; Raven et al., 1995). Marine phytoplankton fractionate to an even greater degree on average, with $\delta^{13}C$ of tissues ranging from -28 to -16 ‰ (Briand et al., 2015; France, 1995; Lamb-Wozniak, 2008).

Coral metabolism includes both calcification by coral polyps and primary production by the mutualistic zooxanthellae symbionts; while calcification is associated with relatively weak fractionation, organic matter production by zooxanthellae produces organic carbon with an isotopic signature of between -16 and -10 ‰ (Heikoop et al.,

2000; Land et al., 1975; Swart et al., 2005). Organic matter production in corals is understood to be largely concurrent with and closely tied to calcification in corals (Cohen et al., 2016; Gattuso et al., 1999; Mallon et al., 2022). Because calcification accounts for only ~25% of overall reef metabolism, we assume that the magnitude of organic matter production in corals is limited to a comparable proportion of overall reef primary production. We thus rule out the possibility that organic matter production by zooxanthellae strongly influences the overall reef ε_{OM}. In all, a more positive overall ε_{OM} is indicative of a large contribution to reef primary production by weakly fractionating organic matter-producing taxa. Thus, we suspect that weakly-fractionating (and non-coral) producers, ones that utilize a greater proportion of HCO_3^-, are responsible for a larger share of primary production on the reef than taxa that use a greater share of CO_2 during photosynthesis.

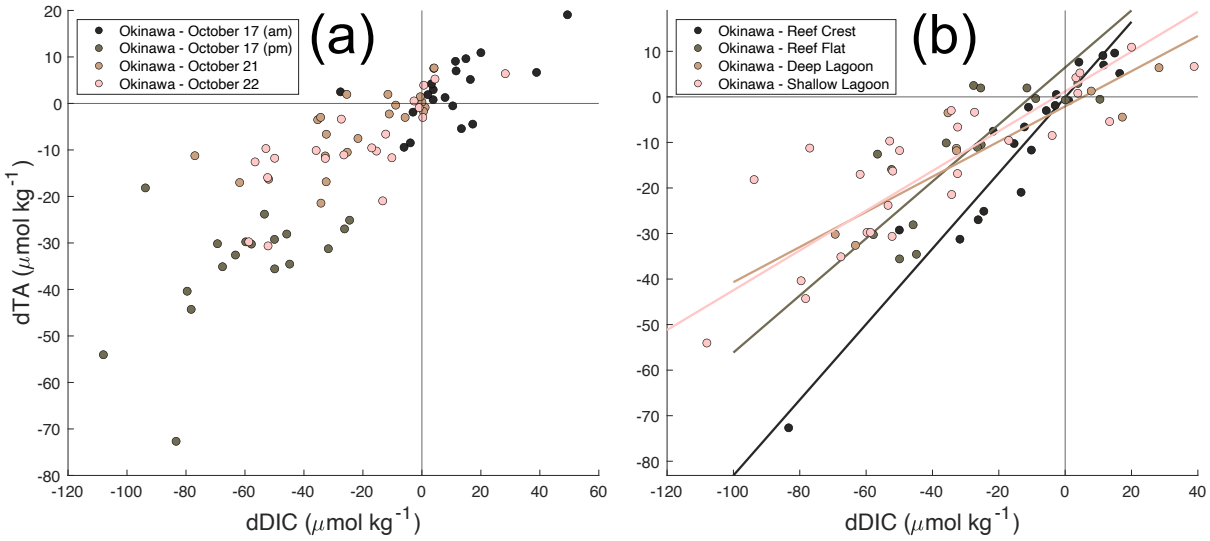

Figure 2.8 Differences between offshore and sample station values for salinity-normalized dTA vs. dDIC (Kekuewa, et al., *in prep*). Model-II geometric mean regressions are fit across the four surveys (dTA = 0.51dDIC + 1 (R^2 = 0.7) and to data grouped by region (slopes = 0.83, 0.63, 0.39, and 0.44 for Reef Crest, Reef Flat, Deep Lagoon, and Shallow Lagoon, respectively). The slope of 0.51 across all data suggest that net primary production was responsible for ~75% of the overall reef metabolism.

We also calculated ε_{OM} for specific regions of the reef to investigate whether more localized signals of production could be observed. We expect production in the shallow lagoon to be dominated by eelgrass. This expectation is reflected in the lower slope of dTA:dDIC (0.44), therefore higher production to calcification ratio, in the shallow lagoon relative to the overall reef (Figure 2.8). Indeed, the local ε_{OM} of -10 ‰ falls between the estimated ranges based on the $\delta^{13}C$ of organic tissue in seagrasses and benthic macroalgae. From photographs not shown, the deep lagoon appears to have a greater abundance of benthic macroalgae and a lesser abundance of eelgrass than the shallow lagoon region. Assuming the same fractionation factors for benthic macroalgae and seagrasses as before, the ε_{OM} of -16.5 ‰ again agrees with the increase in benthic macroalgae and therefore stronger fractionation of carbon during production.

The ε_{OM} of -9.1 ‰ over the reef crest and ε_{OM} of -7.6 ‰ over the reef flat fall just above the range of estimated fractionation by zooxanthellae, though other photosynthesizing taxa are presumably important as well. We can see in Figure 2.3 that the spatial coverage of $\delta^{13}C$-DIC observations over the reef crest is generally sparse, and including more observations could have added greater confidence to the ε_{OM} we calculate for the reef crest.

We note that while our calculated ε_{OM} fall within reasonable ranges, these estimations are based on few data from a single day, and in most cases our estimated values of ε_{OM} do not differ significantly between regions. Further, changes in local seawater chemistry include imprints of biogeochemistry from other parts of the reef ecosystem and are influenced by several factors, such as residence time and flow

speed, which need to be constrained before assigning greater confidence to our estimates of local ε_{OM}.

5 Summary

In this study, we report observations of organic and inorganic carbon isotopes in seawater on a fringing reef in Okinawa, Japan, and a barrier reef in Kāne'ohe Bay, Hawai'i. With coral reef ecosystems' composition and function expected to transform under multiple anthropogenic stressors, the data we present provide snapshots of the state of each ecosystem as a reference for future observations to signal changes in community function. In Okinawa, these isotopic observations suggest a strong influence of benthic macroalgae and seagrasses on overall ecosystem metabolism. In Kāne'ohe Bay, organic matter observations reveal terrestrial inputs to bulk organic matter on the reef and imply high production over the shallowest region of the reef. We note that the data we present represent limited spatial coverage and affirm that greater coverage in future surveys would increase confidence in characterizing reef composition and function. Observations of organic and inorganic carbon isotope data offer a useful means of monitoring changes in coral reef ecosystems and should be included in reef seawater surveys when possible.

Acknowledgements

Thank you to Dr. Andreas J. Andersson for your mentoring on this project. Thank you to the people in San Diego and Okinawa who helped make much of the work of Chapter 2 possible. To Hayashi-san, Yoshino-san, Inoha-san, and the members of the Mitarai Unit, thank you for your hospitality and patience during our whirlwind field

campaign in 2019. Thank you to the members of the Aluwihare lab for being so generous with your time and resources in making the organic carbon measurements possible. Finally, thank you to Dr. Tim Lueker for helping with the analysis of 40+ seawater samples on the vacuum extraction line. Chapter 2 contains material currently being prepared for publication, coauthored with Andersson, A.J., Rintoul, M.S., Kekuewa, S.A., Courtney, T.A., Pezner, A.K., Mitarai, S, Page, H., Köster, I., DeCarlo, E., Nelson, C., Aluwihare, L., and Howins, N. The dissertation author was the primary researcher and author of this chapter.

References

Agostini, S., Harvey, B. P., Wada, S., Kon, K., Milazzo, M., Inaba, K. and Hall-Spencer, J. M.: Ocean acidification drives community shifts towards simplified non-calcified habitats in a subtropical−temperate transition zone, Sci. Rep., 8(1), 1–11, doi:10.1038/s41598-018-29251-7, 2018.

Andersson, A. J. and Gledhill, D.: Ocean acidification and coral reefs: effects on breakdown, dissolution, and net ecosystem calcification, Ann. Rev. Mar. Sci., 5, 321–348, 2013.

Bauer, J. E.: Carbon isotopic composition of DOM, Biogeochem. Mar. dissolved Org. matter, 405–453, 2002.

Bertilsson, S., Berglund, O., Karl, D. M. and Chisholm, S. W.: Elemental composition of marine Prochlorococcus and Synechococcus: Implications for the ecological stoichiometry of the sea, Limnol. Oceanogr., 48(5), 1721–1731, 2003.

Bidwell, R. G. S. and McLachlan, J.: Carbon nutrition of seaweeds: photosynthesis, photorespiration and respiration, J. Exp. Mar. Bio. Ecol., 86(1), 15–46, 1985.

Bj, P. and Fry, B.: Stable isotopes in ecosystem studies, Annu. Rev. Ecol. Syst., 18, 293–320, 1987.

Briand, M. J., Bonnet, X., Goiran, C., Guillou, G. and Letourneur, Y.: Major sources of organic matter in a complex coral reef lagoon: identification from isotopic signatures ($\delta^{13}C$ and $\delta^{15}N$), PLoS One, 10(7), e0131555, 2015.

Cao, W., Huang, Z., Zhai, W., Li, Y. and Hong, H.: Isotopic evidence on multiple sources of nitrogen in the northern Jiulong River, Southeast China, Estuar. Coast. Shelf Sci., 163, 37–43, 2015.

Carvalho, M. C., Santos, I. R., Maher, D. T., Cyronak, T., McMahon, A., Schulz, K. G. and Eyre, B. D.: Drivers of carbon isotopic fractionation in a coral reef lagoon: Predominance of demand over supply, Geochim. Cosmochim. Acta, 153, 105–115, 2015.

Chisholm, J. R. M. and Gattuso, J.-P.: Validation of the alkalinity anomaly technique for investigating calcification of photosynthesis in coral reef communities, Limnol. Oceanogr., 36(6), 1232–1239, 1991.

Close, H. G. and Henderson, L. C.: Open-ocean minima in $\delta^{13}C$ values of particulate organic carbon in the lower euphotic zone, Front. Mar. Sci., 7, 540165, 2020.

Cohen, I., Dubinsky, Z. and Erez, J.: Light enhanced calcification in hermatypic corals: new insights from light spectral responses, Front. Mar. Sci., 2, 122, 2016.

Contreras-Silva, A. I., Tilstra, A., Migani, V., Thiel, A., Pérez-Cervantes, E., Estrada-Saldívar, N., Elias-Ilosvay, X., Mott, C., Alvarez-Filip, L. and Wild, C.: A meta-analysis to assess long-term spatiotemporal changes of benthic coral and macroalgae cover in the Mexican Caribbean, Sci. Rep., 10(1), 1–12, doi:10.1038/s41598-020-65801-8, 2020.

Costanza, R., de Groot, R., Sutton, P., der Ploeg, S., Anderson, S. J., Kubiszewski, I., Farber, S. and Turner, R. K.: Changes in the global value of ecosystem services, Glob. Environ. Chang., 26, 152–158, 2014.

Courtney, T. A., De Carlo, E. H., Page, H. N., Bahr, K. D., Barro, A., Howins, N., Tabata, R., Terlouw, G., Rodgers, K. S. and Andersson, A. J.: Recovery of reef-scale calcification following a bleaching event in K{\=a}ne'ohe Bay, Hawai'i, Limnol. Oceanogr. Lett., 3(1), 1–9, 2018.

Cyronak, T., Andersson, A. J., Langdon, C., Albright, R., Bates, N. R., Caldeira, K., Carlton, R., Corredor, J. E., Dunbar, R. B., Enochs, I., Erez, J., Eyre, B. D., Gattuso, J.-P., Gledhill, D., Kayanne, H., Kline, D. I., Koweek, D. A., Lantz, C., Lazar, B., Manzello, D., McMahon, A., Meléndez, M., Page, H. N., Santos, I. R., Schulz, K. G., Shaw, E., Silverman, J., Suzuki, A., Teneva, L., Watanabe, A. and Yamamoto, S.: Taking the metabolic pulse of the world's coral reefs, edited by C. R. Voolstra, PLoS One, 13(1), e0190872, doi:10.1371/journal.pone.0190872, 2018.

DeCarlo, T. M., Cohen, A. L., Wong, G. T. F., Shiah, F., Lentz, S. J., Davis, K. A., Shamberger, K. E. F. and Lohmann, P.: Community production modulates coral reef pH and the sensitivity of ecosystem calcification to ocean acidification, J. Geophys. Res. Ocean., 122(1), 745–761, doi:10.1002/2016JC012326, 2017.

Dickson, A. G., Sabine, C. L. and Christian, J. R.: Guide to best practices for ocean CO_2 measurements., North Pacific Marine Science Organization., 2007. Doney, S. C., Fabry, V. J., Feely, R. A. and Kleypas, J. A.: Ocean acidification: the other CO_2 problem, 2009.

Druffel, E. R. M., Williams, P. M., Bauer, J. E. and Ertel, J. R.: Cycling of dissolved and particulate organic matter in the open ocean, J. Geophys. Res., 97(C10), 15639–15659, doi:10.1029/92jc01511, 1992.

Emrich, K., Ehhalt, D. H. and Vogel, J. C.: Carbon isotope fractionation during the precipitation of calcium carbonate, Earth Planet. Sci. Lett., 8(5), 363–371, 1970.

Enochs, I. C., Manzello, D. P., Donham, E. M., Kolodziej, G., Okano, R., Johnston, L., Young, C., Iguel, J., Edwards, C. B., Fox, M. D., Valentino, L., Johnson, S., Benavente, D., Clark, S. J., Carlton, R., Burton, T., Eynaud, Y. and Price, N. N.: Shift from coral to macroalgae dominance on a volcanically acidified reef, Nat. Clim. Chang., 5(12), 1083–1088, doi:10.1038/nclimate2758, 2015.

Erez, J., Bouevitch, A. and Kaplan, A.: Carbon isotope fractionation by photosynthetic aquatic microorganisms: experiments with Synechococcus PCC7942, and a simple carbon flux model, Can. J. Bot., 76(6), 1109–1118, 1998.

Ertel, J. R. and Hedges, J. I.: Sources of sedimentary humic substances: vascular plant debris, Geochim. Cosmochim. Acta, 49(10), 2097–2107, 1985.

Fabricius, K. E., Langdon, C., Uthicke, S., Humphrey, C., Noonan, S., De'ath, G., Okazaki, R., Muehllehner, N., Glas, M. S. and Lough, J. M.: Losers and winners in coral reefs acclimatized to elevated carbon dioxide concentrations, Nat. Clim. Chang., 1(3), 165–169, doi:10.1038/nclimate1122, 2011.

France, R. L.: Carbon-13 enrichment in benthic compared to planktonic algae: foodweb implications, Mar. Ecol. Prog. Ser., 124, 307–312, 1995.

Franklin, E. C., Jokiel, P. L. and Donahue, M. J.: Predictive modeling of coral distribution and abundance in the Hawaiian Islands, Mar. Ecol. Prog. Ser., 481, 121–132, 2013.

Freeman, K. H. and Hayes, J. M.: Fractionation of carbon isotopes by phytoplankton and estimates of ancient CO_2 levels, Global Biogeochem. Cycles, 6(2), 185–198, 1992.

Fry, B.: Conservative mixing of stable isotopes across estuarine salinity gradients: a conceptual framework for monitoring watershed influences on downstream fisheries production, Estuaries, 25(2), 264–271, 2002.

Gattuso, J.-P., Allemand, D. and Frankignoulle, M.: Levels in Coral Reefs: A Review on Interactions and Control by Carbonate Chemistry (1)., Am. Zool., 39(i1), 1, 1999.

Giordano, M., Beardall, J. and Raven, J. A.: CO 2 concentrating mechanisms in algae: mechanisms, environmental modulation, and evolution, Annu. Rev. Plant Biol., 56, 99–131, 2005.

Gischler, E., Swart, P. K. and Lomando, A. J.: Stable isotopes of carbon and oxygen in modern sediments of carbonate platforms, barrier reefs, atolls and ramps: patterns and implications, Perspect. carbonate Geol. a Tribut. to career Robert Nathan Ginsbg., 61–74, 2009.

Haas, A. F., Nelson, C. E., Wegley Kelly, L., Carlson, C. A., Rohwer, F., Leichter, J. J., Wyatt, A. and Smith, J. E.: Effects of Coral Reef Benthic Primary Producers on Dissolved Organic Carbon and Microbial Activity, edited by R. K. F. Unsworth, PLoS One, 6(11), e27973, doi:10.1371/journal.pone.0027973, 2011.

Haas, A. F., Nelson, C. E., Rohwer, F., Wegley-Kelly, L., Quistad, S. D., Carlson, C. A., Leichter, J. J., Hatay, M. and Smith, J. E.: Influence of coral and algal exudates on microbially mediated reef metabolism, PeerJ, 2013(1), e108, doi:10.7717/peerj.108, 2013.

Haines, E. B. and Montague, C. L.: Food Sources of Estuarine Invertebrates Analyzed Using $^{13}C/^{12}C$ Ratios, Ecology, 60(1), 48–56, doi:10.2307/1936467, 1979.
Heikoop, J. M., Dunn, J. J., Risk, M. J., Tomascik, T., Schwarcz, H. P., Sandeman, I. M. and Sammarco, P. W.: $\delta^{15}N$ and $\delta^{13}C$ of coral tissue show significant inter-reef variation, Coral Reefs-Journal Int. Soc. Reef Stud., 19(2), 189–193, 2000.

Hemminga, M. A. and Mateo, M. A.: Stable carbon isotopes in seagrasses: variability in ratios and use in ecological studies, Mar. Ecol. Prog. Ser., 140, 285–298, 1996.
Jasper, J. P. and Hayes, J. M.: Reconstruction of Paleoceanic PCO 2 levels from carbon isotopic compositions of sedimentary biogenic components, in Carbon Cycling in the Glacial Ocean: Constraints on the Ocean's Role in Global Change, pp. 323–341, Springer., 1994.

Jokiel, P. L.: Jokiel's illustrated scientific guide to Kane 'ohe Bay, DOI, 10(13140), 1–2, 1991.

Kayanne, H., Hata, H., Kudo, S. and Yamano, H.: Seasonal and bleachinginduced changes in coral reef metabolism and CO_2 flux, Glob. Biogeochem. Cycles, 19, 2005.

Kekuewa, S. A. H.: Spatiotemporal Variability of Seawater Carbonate Chemistry in Diverse Coral Reef Environments in South East Asia and Australia, University of California San Diego., *in prep*.

Kennedy, E. V, Roelfsema, C. M., Lyons, M. B., Kovacs, E. M., Borrego-Acevedo, R., Roe, M., Phinn, S. R., Larsen, K., Murray, N. J., Yuwono, D. and others: Reef Cover, a coral reef classification for global habitat mapping from remote sensing, Sci. Data, 8(1), 196, 2021.

Koester, I., Quinlan, Z. A., Nothias, L.-F., White, M. E., Rabines, A., Petras, D., Brunson, J. K., Dührkop, K., Ludwig, M., Böcker, S. and others: Illuminating the dark metabolome of Pseudo-nitzschia--microbiome associations, Environ. Microbiol., 24(11), 5408–5424, 2022.

Koweek, D. A., Forden, A., Albright, R., Takeshita, Y., Mucciarone, D. A., Ninokawa, A. and Caldeira, K.: Carbon Isotopic Fractionation in Organic Matter Production Consistent With Benthic Community Composition Across a Coral Reef Flat, Front. Mar. Sci., 5, 520, doi:10.3389/fmars.2018.00520, 2019.

Kroopnick, P. M.: The distribution of ^{13}C of ΣCO_2 in the world oceans, Deep Sea Res. Part A. Oceanogr. Res. Pap., 32(1), 57–84, 1985.

Lamb-Wozniak, K. A.: Nitrogen cycling on coral reefs: a stable isotopic investigation of nutrient dynamics within the Florida Keys coral reef tract, University of Miami., 2008.

Lamb, K. and Swart, P. K.: The carbon and nitrogen isotopic values of particulate organic material from the Florida Keys: A temporal and spatial study, Coral Reefs, 27(2), 351–362, doi:10.1007/s00338-007-0336-5, 2008.

Land, L. S., Lang, J. C. and Smith, B. N.: Preliminary observations on the carbon isotopic composition of some reef coral tissues and symbiotic zooxanthellae 1, Limnol. Oceanogr., 20(2), 283–287, 1975.

Laws, E. A., Popp, B. N., Bidigare, R. R., Kennicutt, M. C. and Macko, S. A.: Dependence of phytoplankton carbon isotopic composition on growth rate and $CO_{2\ (aq)}$: theoretical considerations and experimental results, Geochim. Cosmochim. Acta, 59(6), 1131–1138, 1995.

Libes, S.: Introduction to marine biogeochemistry, Academic Press., 2011.

Lowe, R. J., Falter, J. L., Monismith, S. G. and Atkinson, M. J.: A numerical study of circulation in a coastal reef-lagoon system, J. Geophys. Res., 114(C6), C06022, doi:10.1029/2008JC005081, 2009.

Lueker, T., Keeling, R., Bollenbacher, A., Walker, S., Morgan, E. and Brooks, M.: Calibration Methodology for the Scripps $^{13}C/^{12}C$ and $^{18}O/^{16}O$ stable Isotope program 1992-2018, 2020.

Mallon, J., Cyronak, T., Hall, E. R., Banaszak, A. T., Exton, D. A. and Bass, A. M.: Light-driven dynamics between calcification and production in functionally diverse coral reef calcifiers, Limnol. Oceanogr., 67(2), 434–449, 2022.

Maslin, M. A. and Thomas, E.: Balancing the deglacial global carbon budget: the hydrate factor, Quat. Sci. Rev., 22(15–17), 1729–1736, 2003.

McCabe, B.: The dynamics of ^{13}C in several New Zealand lakes, University of Waikato., 1985.

McNevin, D. B., Badger, M. R., Whitney, S. M., Von Caemmerer, S., Tcherkez, G. G. B. and Farquhar, G. D.: Differences in Carbon Isotope Discrimination of Three Variants of D-Ribulose-1, 5-bisphosphate Carboxylase/Oxygenase Reflect Differences in Their Catalytic Mechanisms, J. Biol. Chem., 282(49), 36068–36076, 2007.

Muehllehner, N., Langdon, C., Venti, A. and Kadko, D.: Dynamics of carbonate chemistry, production, and calcification of the Florida Reef Tract (2009--2010): Evidence for seasonal dissolution, Global Biogeochem. Cycles, 30(5), 661–688, 2016.

Needoba, J. A., Waser, N. A., Harrison, P. J. and Calvert, S. E.: Nitrogen isotope fractionation in 12 species of marine phytoplankton during growth on nitrate, Mar. Ecol. Prog. Ser., 255, 81–91, 2003.

Nelson, C. E., Alldredge, A. L., McCliment, E. A., Amaral-Zettler, L. A. and Carlson, C. A.: Depleted dissolved organic carbon and distinct bacterial communities in the water column of a rapid-flushing coral reef ecosystem, ISME J., 5(8), 1374–1387, doi:10.1038/ismej.2011.12, 2011.

O'Leary, M. H.: Carbon Isotopes in Photosynthesis, Bioscience, 38(5), 328–336, doi:10.2307/1310735, 1988.

Ostrom, P. H. and Fry, B.: Sources and cycling of organic matter within modern and prehistoric food webs, in Organic geochemistry, pp. 785–798, Springer., 1993.

Page, H. N., Courtney, T. A., De Carlo, E. H., Howins, N. M., Koester, I. and Andersson, A. J.: Spatiotemporal variability in seawater carbon chemistry for a coral reef flat in Kāneʻohe Bay, Hawaiʻi, Limnol. Oceanogr., 64(3), 913–934, doi:10.1002/lno.11084, 2019.

Park, R. and Epstein, S.: Metabolic fractionation of C13 \& C12 in plants, Plant Physiol., 36(2), 133, 1961.

Parker, P. L.: The biogeochemistry of the stable isotopes of carbon in a marine bay, Geochim. Cosmochim. Acta, 28(7), 1155–1164, 1964.

Poloczanska, E. S., Brown, C. J., Sydeman, W. J., Kiessling, W., Schoeman, D. S., Moore, P. J., Brander, K., Bruno, J. F., Buckley, L. B., Burrows, M. T. and others: Global imprint of climate change on marine life, Nat. Clim. Chang., 3(10), 919–925, 2013.

Popp, B. N., Takigiku, R., Hayes, J. M., Louda, J. W. and Baker, E. W.: The post-Paleozoic chronology and mechanism of ^{13}C depletion in primary marine organic matter, Am. J. Sci., 289(4), 436–454, 1989.

Popp, B. N., Laws, E. A., Bidigare, R. R., Dore, J. E., Hanson, K. L. and Wakeham, S. G.: Effect of phytoplankton cell geometry on carbon isotopic fractionation, Geochim. Cosmochim. Acta, 62(1), 69–77, 1998.

Rau, G. H., Froelich, P. N., Takahashi, T. and Des Marais, D. J.: Does sedimentary organic $\delta^{13}C$ record variations in Quaternary ocean [$CO_{2\ (aq)}$]?, Paleoceanography, 6(3), 335–347, 1991a.

Rau, G. H., Takahashi, T., Des Marais, D. J. and Sullivan, C. W.: Particulate organic matter $\delta^{13}C$ variations across the Drake Passage, J. Geophys. Res. Ocean., 96(C8), 15131–15135, 1991b.

Raven, J. A., Walker, D. I., Johnston, A. M., Handley, L. L. and Kübler, J. E.: Implications of ^{13}C natural abundance measurements for photosynthetic performance by marine macrophytes in their natural environment, Mar. Ecol. Prog. Ser., 123, 193–205, 1995.

Raven, J. A., Johnston, A. M., Kübler, J. E., Korb, R., McInroy, S. G., Handley, L. L., Scrimgeour, C. M., Walker, D. I., Beardall, J., Vanderklift, M. and others: Mechanistic interpretation of carbon isotope discrimination by marine macroalgae and seagrasses, Funct. Plant Biol., 29(3), 355–378, 2002.

Redfield, A. C.: The influence of organisms on the composition of seawater, sea, 2, 26–77, 1963.

Riebesell, U. and Wolf-Gladrow, D.: Growth limits on phytoplankton, Nature, 373, 28, 1995.

Rintoul, M. S., Courtney, T. A., Dohner, J. L., Giddings, S. N., Kekuewa, S. A. H., Mitarai, S., Monismith, S. G., Pezner, A. K. and Andersson, A. J.: The Effects of Light Intensity and Flow Speed on Biogeochemical Variability within a Fringing Coral Reef in Onna-son, Okinawa, Japan., J. Geophys. Res. Ocean., e2021JC018369, 2022.

Rodelli, M. R., Gearing, J. N., Gearing, P. J., Marshall, N. and Sasekumar, A.: Stable isotope ratio as a tracer of mangrove carbon in Malaysian ecosystems, Oecologia, 61(3), 326–333, doi:10.1007/BF00379629, 1984.

Roeske, C. A. and O'Leary, M. H.: Carbon isotope effects on enzyme-catalyzed carboxylation of ribulose bisphosphate, Biochemistry, 23(25), 6275–6284, 1984.

Sackett, W. M. and Thompson, R. R.: Isotopic organic carbon composition of recent continental derived clastic sediments of eastern Gulf Coast, Gulf of Mexico, Am. Assoc. Pet. Geol. Bull., 47(3), 525–528, 1963.

Sackett, W. M., Eckelmann, W. R., Bender, M. L. and Be, A. W. H.: Temperature dependence of carbon isotope composition in marine plankton and sediments, Science (80-.)., 148(3667), 235–237, doi:10.1126/science.148.3667.235, 1965.

Sampei, Y. and Matsumoto, E.: C/N ratios in a sediment core from Nakaumi Lagoon, southwest Japan—usefulness as an organic source indicator—, Geochem. J., 35(3), 189–205, 2001.

Sand-Jensen, K. A. J. and Gordon, D. M.: Differential ability of marine and freshwater macrophytes to utilize HCO 3-and CO 2, Mar. Biol., 80, 247–253, 1984.

Sarmiento, J. L.: Ocean biogeochemical dynamics, in Ocean Biogeochemical Dynamics, Princeton university press., 2013.

Sharkey, T. D. and Berry, J. A.: Carbon isotope fractionation of algae as influenced by an inducible CO_2 concentrating mechanism, Inorg. carbon uptake by Aquat. Photosynth. Org., 389–401, 1985.

Shultz, D. J. and Calder, J. A.: Organic carbon $^{13}C/^{12}C$ variations in estuarine sediments, Geochim. Cosmochim. Acta, 40(4), 381–385, doi:10.1016/0016-7037(76)90002-8, 1976.

Smith, B. N. and Epstein, S.: Biogeochemistry of the Stable Isotopes of Hydrogen and Carbon in Salt Marsh Biota, Plant Physiol., 46(5), 738–742, doi:10.1104/pp.46.5.738, 1970.

Smith, B. N. and Epstein, S.: Two categories of c/c ratios for higher plants., Plant Physiol., 47(3), 380–4, doi:10.1104/pp.47.3.380, 1971.

Smith, S. V. and Kroopnick, P.: Carbon-13 isotopic fractionation as a measure of aquatic metabolism, Nature, 294(5838), 252–253, doi:10.1038/294252a0, 1981.

Smith, S. V: Carbon Dioxide Dynamics: a Record of Organic Carbon Production, Respiration, and Calcification in the Eniwetok Reef Flat Community 1, Limnol. Oceanogr., 18(1), 106–120, 1973.

Smith, S. V, Kimmerer, W. J., Laws, E. A., Brock, R. E. and Walsh, T. W.: Kaneohe Bay sewage diversion experiment: perspectives on ecosystem responses to nutritional perturbation, 1981.

Smith, S. V, Schneider, R. C. and Tribble, G. W.: Carbon isotopic balance in coral reef ecosystems, in Proc 5th Int Coral Reef Symp, Tahiti, vol. 3, pp. 445–450., 1985.

Suzuki, A. and Kawahata, H.: Carbon budget of coral reef systems: an overview of observations in fringing reefs, barrier reefs and atolls in the Indo-Pacific regions, Tellus B Chem. Phys. Meteorol., 55(2), 428–444, doi:10.3402/tellusb.v55i2.16761, 2003.

Swart, P. K., Saied, A. and Lamb, K.: Temporal and spatial variation in the $\delta^{15}N$ and $\delta^{13}C$ of coral tissue and zooxanthellae in Montastraea faveolata collected from the Florida reef tract, Limnol. Oceanogr., 50(4), 1049–1058, 2005.

Thorp, J. H., Delong, M. D., Greenwood, K. S. and Casper, A. F.: Isotopic analysis of three food web theories in constricted and floodplain regions of a large river, Oecologia, 551–563, 1998.

Tuerena, R. E., Ganeshram, R. S., Humphreys, M. P., Browning, T. J., Bouman, H. and Piotrowski, A. P.: Isotopic fractionation of carbon during uptake by phytoplankton across the South Atlantic subtropical convergence, Biogeosciences, 16(18), 3621–3635, 2019.

Turner, J. V: Kinetic fractionation of carbon-13 during calcium carbonate precipitation, Geochim. Cosmochim. Acta, 46(7), 1183–1191, 1982.

U.S. Census Bureau: 2020 Census Results., 2020.

Vogel, J. C.: Fractionation of the Carbon Isotopes During Photosynthesis, in Fractionation of the Carbon Isotopes During Photosynthesis, pp. 5–29, Springer Berlin Heidelberg., 1980.

Vogel, J. C.: Variability of Carbon Isotope Fractionation during Photosynthesis, in Stable Isotopes and Plant Carbon-water Relations, pp. 29–46, Elsevier., 1993.

Volkman, J. K. and Tanoue, E.: Chemical and biological studies of particulate organic matter in the ocean, J. Oceanogr., 58, 265–279, 2002.

Watanabe, A., Kayanne, H., Hata, H., Kudo, S., Nozaki, K., Kato, K., Negishi, A., Ikeda, Y. and Yamano, H.: Analysis of the seawater CO_2 system in the barrier reef-lagoon system of Palau using total alkalinity-dissolved inorganic carbon diagrams, Limnol. Oceanogr., 51(4), 1614–1628, 2006.

Wilkes, E. B. and Pearson, A.: A general model for carbon isotopes in red-lineage phytoplankton: Interplay between unidirectional processes and fractionation by RubisCO, Geochim. Cosmochim. Acta, 265, 163–181, 2019.

Williams, P. M. and Gordon, L. I.: Carbon-13: carbon-12 ratios in dissolved and particulate organic matter in the sea, in Deep Sea Research and Oceanographic Abstracts, vol. 17, pp. 19–27., 1970.

Wissel, B., Gaçe, A. and Fry, B.: Tracing river influences on phytoplankton dynamics in two Louisiana estuaries, Ecology, 86(10), 2751–2762, 2005.

Yamamuro, M.: Importance of epiphytic cyanobacteria as food sources for heterotrophs in a tropical seagrass bed, Coral reefs, 18(3), 263–271, 1999.

Zanden, M. J. Vander and Rasmussen, J. B.: Variation in $\delta^{15}N$ and $\delta^{13}C$ trophic fractionation: implications for aquatic food web studies, Limnol. Oceanogr., 46(8), 2061–2066, 2001.

Ziegler, S. and Benner, R.: Dissolved organic carbon cycling in a subtropical seagrass-dominated lagoon, Mar. Ecol. Prog. Ser., 180, 149–160,

CHAPTER 3: Development of a high-precision seawater DIC analysis system

1 Introduction

Measurements of dissolved inorganic carbon (DIC) concentrations in seawater provide fundamental information about natural and anthropogenic processes acting on the ocean, such as rates of photosynthesis or long-term uptake of anthropogenic CO_2 (Peng et al., 1998). DIC concentrations in the ocean span the range of ~1900–2400 μmol kg^{-1}, and changes in DIC concentrations due to biogeochemical processes can differ depending on the spatial and temporal scales. In shallow and productive coastal ecosystems, such as coral reefs, DIC concentrations can oscillate by as much as ± 200 μmol kg^{-1} over a diel period (Koweek et al., 2015), while anthropogenic CO_2 uptake in Pacific surface waters has been estimated to increase DIC on the order of tenths to a couple of μmol kg^{-1} yr^{-1} (Keeling et al., 2004; Kouketsu et al., 2013).

Seawater DIC can currently be measured through one of several techniques. Most common are coulometric (Johnson et al., 1993), non-dispersive infrared (Goyet and Snover, 1993; Kaltin et al., 2005), photometric (Stoll et al., 2001), and spectroscopic (Bandstra et al., 2006; Bass et al., 2012b, 2012a; Huang et al., 2013) methods, which achieve repeatability between ±1.5-3 μmol kg^{-1}. At present, the most precise DIC measurements (± 0.5 μmol kg^{-1}) are accomplished via manometry, where a seawater sample is acidified to convert all DIC to CO_2 gas, the gas is extracted and isolated, and then DIC is calculated from an equation of state for CO_2 using information about the pressure, temperature, and volume of the isolated gas sample (Lueker et al., 1998). This technique, which is currently employed by the Scripps CO_2 group to make ocean time-series measurements (Karl and Lukas, 1996; Michaels and Knap, 1996) is highly labor- and time-intensive. Extraction of CO_2 gas from the sample requires ~60-90

minutes of hands-on time, followed by a processing time on a similar order in a custom manometric device. The equipment needed for such extractions is custom-built and not available for commercial purchase. Further, a high level of technical skill is required to perform these measurements.

Here we present a method for measuring seawater DIC concentrations that achieves a repeatability on the order of 0.5 μmol kg^{-1}, needs minimal hands-on time after startup, and can be automated to run multiple samples in series. This method involves the removal of CO_2 from an acidified seawater by flowing the sample through a reverse-flow contactor, which comprises a gas-permeable membrane with a CO_2-free carrier gas flowing outside the membrane in the opposite direction. The carrier gas then flows to a cavity ringdown spectrometer to quantify CO_2 concentration. By repeatedly switching the seawater flow between sample and reference, the method allows precise comparison of sample and reference. This method was verified using certified reference materials and running samples from the Bermuda Atlantic Time Series (BATS) station that were also measured in duplicate via manometry. This method is still under development to achieve improved repeatability on measurements and also has the potential to be combined with a system to concurrently measure total alkalinity (TA) (Li et al., 2013) or be interfaced to a quantum cascade laser (QCLS) multi-pass system for stable isotope analysis of dissolved inorganic carbon (δ^{13}C-DIC).

2 Methods

Our “contactor system” method centers on a gas-permeable membrane “contactor,” with a carrier gas and acidified seawater flowing on opposing sides of the

membrane to strip and deliver seawater DIC in the form of CO_2 to a gas analyzer for quantification of DIC of the sample. The schematic of the contactor system is shown in Figure 3.1.

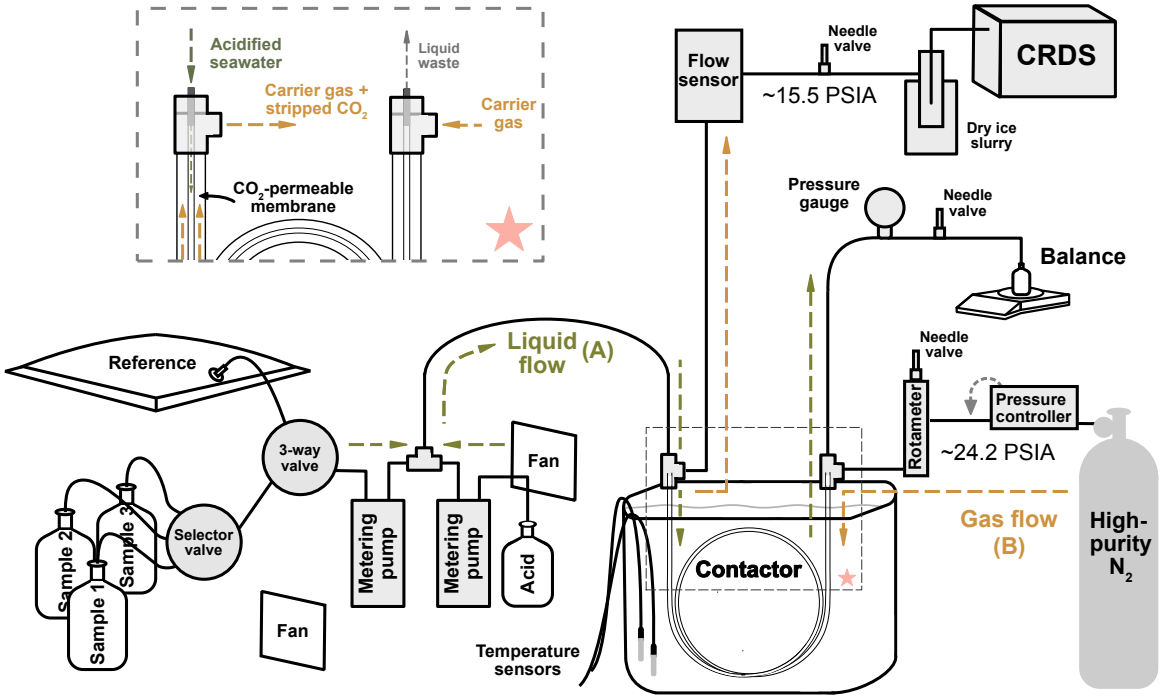

Figure 3.1 Schematic of continuous-flow DIC measurement "contactor system." The overall system can be divided into two flows: (A) liquid flow (direction shown with dashed green lines) and (B) gas flow (direction shown with dashed orange lines). Gas is flowed into the system from a high-purity nitrogen tank (bottom right), with two pressure controllers (one just downstream of the cylinder, the other just upstream of the CRDS) regulating the flow rate. The dashed-line inset box (marked with a pink star) is enlarged and re-illustrated in the upper left corner of the schematic (marked with a larger pink star).

2.1 Membrane "contactor"

The removal of inorganic carbon from seawater is achieved by flowing the liquid sample through the CO_2-permeable membrane "contactor." The contactor consists of thin-walled Teflon AF 2400 tubing (119 cm in length, 0.73 mm OD, 0.61 mm ID, 0.64 μm

wall, Biogeneral, San Diego, CA), which is highly permeable to CO_2 gas, housed in 0.63 cm OD, 0.39 cm ID Pyrex glass tubing. Acidified seawater flows through the Teflon AF 2400, with a CO_2-free carrier gas (high-purity N_2) stream flowing outside the Teflon tubing in the opposite direction. CO_2 (and CH_4) gas diffuses across the Teflon membrane into the carrier gas stream towards the CRDS. The glass tubing of the contactor was melted into a coil shape (length 119.5 cm, diameter ~25 cm) so that the contactor can sit in a water bath for short-term temperature stabilization. Temperature sensors record the water bath temperature. The Teflon AF 2400 portion of the liquid line is connected to the Hastelloy C lines using Loctite 7649 primer and Loctite UK-05FL polyisocyanate urethane adhesive (www.loctiteproducts.com).

After passing through the contactor, the N_2 – CO_2 gas mixture flows to a cavity-ringdown spectrometer (CRDS) (Picarro G2301 Gas Concentration Analyzer, www.picarro.com). The CRDS makes simultaneous measurements of CO_2, CH_4, and water vapor, and new data for each species is available every 2-3 seconds. A dry ice-ethanol slurry trap is installed downstream of the contactor before the gas stream reaches the CRDS to prevent liquid from entering the analyzer should either of the Teflon-Hastelloy connections of the contactor fail.

2.2 Liquid flow path

The seawater is alternately sourced from seawater reference or from one of several samples using a three-way valve and a selector valve (valves and configuration further described in Section 2.4). The seawater flow rate (0.27 mL min^{-1}) is set by a VICI M6 positive displacement pump (volume precision <0.5% coefficient of variation at a

delivered volume of 125 μL). A second identical pump flows 85% phosphoric acid at 0.03 mL min^{-1} from a glass bottle via PEEK tubing. Self-heating of pumps (and any potential impacts on pump performance) is mitigated by two fans directed towards the pumps. The seawater and acid streams exit the pumps via Hastelloy C tubing of equal lengths and join at a Valco Hastelloy C tee (www.vici.com). The acidified mixture flows through a length of Hastelloy C tubing (52 cm at 0.3 mL min^{-1}) to promote diffusive mixing between the acid and seawater components. The Hastelloy C and PEEK tubing constituting the liquid flow path have identical dimensions of 1/16" OD (0.16 cm) and 0.03" ID (0.076 cm). A needle valve near the waste port of the water line is used to adjust the backpressure in the water line. The pressure immediately upstream of the needle valve is measured using a 0-5 PSIG diaphragm-type pressure gauge (www.measureman.com) attached to a gauge guard (Plast-O-Matic GGMEB1-PP Gauge Guard, www.plastomatic.com). The pressure at this point is kept between the 1-2.5 PSIG range, which we found was helpful to mitigate bubble formation in the liquid line, which causes aberrations in the CO_2 signal.

2.3 Gas flow path

The high-purity N_2 carrier gas is delivered via a high-pressure cylinder containing compressed dry air with a pressure regulator metering the flow. The carrier gas passes through the interstice of the contactor, stripping CO_2 from the acidified seawater across the permeable membrane, and finally flows to the CRDS analyzer. Before reaching the gas analyzer terminus, the gas flow passes through four points of regulation: 1. a pressure transducer (100-PSIA MKS 850B Baratron Pressure Transducer;

www.mksinst.com) and control valve (and MKS Type 248 Control Valve; www.mksinst.com) immediately downstream of the cylinder, 2. a needle valve attached to a Cole-Parmer correlated variable area flowmeter (Cole-Parmer correlated variable area flowmeter; www.coleparmer.com, PMR1-010647) downstream of 1., 3. a needle valve downstream of the contactor, and 4. the CRDS, the destination of the gas flow, which maintains a nearly constant pressure of 140 ± 0.024 torr in the instrument cavity. Voltages from the pressure transducer are converted to digital signals and are recorded. Gas flow is also monitored and recorded by a mass flow meter (Alicat Scientific M Series: Mass Flow Meter, 200 sccm, www.alicat.com) downstream of the contactor and upstream of 3. Volume flow recorded by the mass flow meter, which is dependent on temperature, generally falls between 55.5 and 56 standard cubic centimeters per minute (sccm). The volume of the gas interstice is roughly between 30 and 40 cm^3.

2.4 Sample-reference comparison

For precise comparison between sample and reference material, seawater samples are alternated for analysis with a seawater standard at 7.5-minute intervals. This interval was chosen as the shortest time interval at which the CO_2 signal sufficiently stabilizes after sample sweepout. As a first step in the data reduction, we process CRDS signals to compute normalized differences in per mil (‰) units. We begin with the expression for the CRDS signal χ_{CO2} (the raw reported CO_2 signal on the analyzer):

$$\chi_{CO2} = e * \left(\frac{F_w}{F_g}\right) * DIC_{V,sample} \quad (1)$$

where *e* is the percent efficiency of the contactor, F_w is the volumetric flow of the sample in L min^{-1} (not including acid flow), F_g is the gas flow in µmol min^{-1}, and DIC_V is the DIC concentration of the sample in µmol L^{-1}. As the pump establishes a nominally constant volumetric (rather than mass) flow, the CRDS signal is expected to scale with DIC in volumetric rather than mass units.

We compare the signals of a sample and a reference according to

$$\delta(\mathcal{X}_{CO2}) = \left(\frac{\mathcal{X}_{CO2,sample}}{\mathcal{X}_{CO2,reference}} - 1\right) * 1{,}000 \quad (2)$$

where $\mathcal{X}_{CO2}$ is the mole fraction of CO_2 as recorded by the CRDS. We combine Equations 1 and 2 to yield:

$$\delta(DIC_{V,sample}) = \left(\frac{DIC_{V,sample}}{DIC_{V,reference}} - 1\right) * 1000 \quad (3)$$

Finally, $\delta(DIC_{V,sample})$ can be converted to DIC reported as a volume concentration (µmol L^{-1}) using the expression ‰ according to:

$$DIC_{V,sample} = a * \delta + DIC_{V,reference} \quad (4)$$

in which *a* is empirically derived and $DIC_{V,reference}$ is the DIC concentration in volume units of the reference material. We hereafter differentiate DIC in volume units from DIC in mass units using the abbreviations DIC_V and DIC_M, respectively. These are related according to $DIC_v = \rho\ DIC_M$ where ρ is seawater density.

The liquid metering pumps deliver at a constant volume both sample and reference. Temperature influences the mass delivered by the pumps and therefore the resulting $\delta(\mathcal{X}_{CO2})$ values. However, because the temperature effects on the sample and standard are very similar, $\delta(\mathcal{X}_{CO2})$ is largely independent of the pump temperature. We

thus treat $\delta(\mathcal{X}_{CO2})$ as valid for DIC measured in μmol L^{-1} of seawater at a reference temperature of 20 ˚C (rather than the pump temperature).

Sample and reference are alternately pulled by a metering pump, with switching between sample and reference enabled by a Norgren Kloehn V6 Syringe pump (used as a changeover valve with the syringe removed, www.norgren.com). The syringe pump is connected to the sample and standard via separate 16-cm lines of Hastelloy C tubing (1/16” ID). Two-piece 1/16” PEEK fingertight fittings (www.idex-hs.com) connect the tubing to the syringe pump.

2.5 Seawater sample and reference materials

As a reference we use local seawater (DIC = 2016.1 μmol kg^{-1}, TA = 2222.1 μmol kg^{-1}, Sal = 33.3 ppt; “JDCS-BagD" in Table 3.1) stored in a 10L Cali-5-Bond multi-layer foil sampling bag (www.calibrated.com) to mitigate the formation of a gaseous headspace. The seawater was poisoned with 200 μL saturated $HgCl_2$ solution per 1L seawater following (Dickson et al., 2007) and was passed through combusted 47mm GF/F filters during filling. We also begin and end each run with analysis of a “low DIC” bag (“JDCS-BagC” in Table 3.1), which consists of poisoned water certified reference material diluted with DI water to which salt has been added proportionately to maintain the seawater’s original salinity. For calibration of the contactor system, we used a combination of seawater sample bottles collected from the Bermuda Station S site and seawater collected off the Scripps Pier in La Jolla, CA.

Table 3.1 Seawater sample and reference materials used in the study. “Use” refers to their function relating to calibration of the contactor system.

Name	Description	Use	DIC_M (μmol kg^{-1})	DIC_V (μmol L^{-1})	TA (μmol kg^{-1})	pCO_2 at 20˚C (μatm)	Salinity (ppt)
WHW-BagA	Filled May 2018 from Scripps Pier faucet, currently sulfuric smell. 7L when received	Reference	2279.1	2333.5	2253.2 (Dec 1, 2022) 2266.1 (Feb 1, 2023)	2539.4 (Dec 1, 2022) 2302.8 (Feb 1, 2023)	33.8
WHW-BagB	Filled May 2018 from Scripps Pier faucet, currently sulfuric smell. 3L when received	Sample	N/A	N/A	N/A	N/A	N/A
JDCS-BagC	Waste CRM plus DI and NaCl	“Low-DIC” Sample	1932.2	1977.6	1968.3	1357.6	33.4
JDCS-BagD	Filtered Scripps Pier water	Reference	2016.1	2063.4	2222.1	512.2	33.3
BERM	Bermuda station samples	Sample	2048.0 – 2097.9	2096.3 – 2152.8	2358.0 – 2405.1	~328 – 342	36.3 – 36.8
CRM	Dickson Certified Reference Material, Batch #201	DIC calibration	2048.2	2096.3	2207.6	643	33.3

2.6 Independent measurement of DIC, TA, and salinity

DIC, TA, and salinity of seawater samples from Bermuda and reference materials (Table 3.1) were independently quantified. Samples were analyzed for DIC content via vacuum-line gas extraction, in which samples are acidified and the released CO_2 gas is isolated using a liquid nitrogen trap and stored in glass break-seal tubes, followed by manometric analysis, in which volume, pressure and temperature are measured to convert the liquid sample volume to number of moles of CO_2 gas (Lueker et al., 1998). The method requires ~60 mL of sample in a specialized pipette for DIC analysis. Aliquots were transferred from bags to the pipette using a syringe, while seawater samples in bottles could be directly transferred to the pipettes by pressurizing the bottle

headspace. Bermuda samples were vacuum extracted on the same day that they were run on the contactor system; the samples were first opened to remove the aliquot for vacuum extraction before being connected to the contactor system. Bottles that were analyzed were resealed and stored for TA and salinity analysis within one week. TA was analyzed using an open-cell titration with coulometrically-analyzed hydrochloric acid (Dickson et al., 2003). Salinity was measured relative to IAPSO Standard Seawater using a Guildline Autosal Model 8400 conductive salinometer.

2.7 Sample selection

The system allows for analysis of multiple seawater samples in sequence. Switching between samples is achieved via an 8-position Model C25Z VICI Flow-through Flowpath Stream Selector (www.vici.com). The stream selector contains 17 ports: eight inlet ports, eight individual outlet ports, and one common outlet port. Each inlet port on the selector valve has a corresponding outlet port such that an inlet port is directly connected to its corresponding outlet when the inlet is not actively selected for analysis. Each unselected outlet port is connected to PEEK tubing terminating in a plastic stopcock; sample is flowed through each of the ports' outlet tubing and stoppered before running so that no air sits in the unselected ports' flow paths. Sample bottles are stoppered with rubber plugs with two small openings, one for the tubing line and the other for letting air in to fill the headspace as sample is drawn.

3 Results and Discussion

3.1 Illustration of system performance

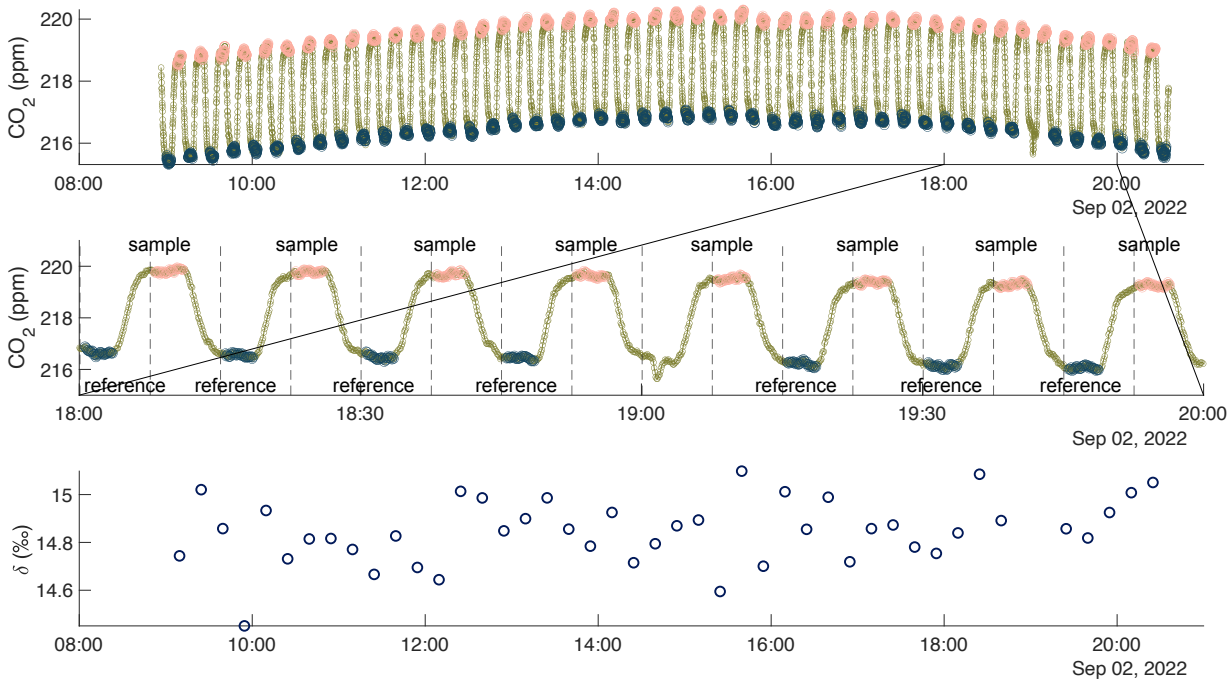

Figure 3.2 Contactor system CO_2 signal output (top and middle panels) and subsequent δ values (bottom panel) when running a bag containing seawater (WHW-BagB) against a seawater working reference (WHW-BagA). Integrated data for calculating δ (Equation 2) are highlighted in pink (sample) and dark blue (reference) and are separated by data that is masked out to avoid transitions. A magnified view of the sample-reference comparisons is shown in the middle panel. Vertical dashed lines in the middle panel mark the time at which the valve controlling seawater input to the system switches between sample and reference. A signal aberration assumed to have originated from a bubble formed in the liquid line appears just after 19:00 and is excluded from the δ calculations. We use the color map batlow (Crameri, 2021) in this study to prevent visual distortion of the data and to make this work accessible to readers with differing color vision (Crameri et al., 2020).

Figure 3.2 shows the response of the CRDS analyzer to 7.5-minute switching between sample and reference. After each switch, the signal remains stable for around 3.5 minutes before the CRDS signal shows any response. The new signal begins to stabilize after ~7.5 minutes. Here we integrate the signal in the 8-to-11-minute window

for calculating δ values (Figure 3.3), an interval over which the signal has largely stabilized but prior to the arrival of the next transition. This windowing leads to at most very small scale contraction due to incomplete sample-reference sweepout, as discussed in Section 3.3. We accept this contraction as a tradeoff with introducing additional drift in the CRDS signal resulting from a longer switching timescale. These switches are repeated to yield a collection of estimates of δ by comparing the sample and reference signals (Figure 3.2c).

Prior to calculating δ values, the CRDS signal is filtered by removing jogs that contain signal aberrations arising from bubbles (deviations of > 0.75 ppm from the mean). We then filter δ values in a single pass by excluding those that are greater than 2 standard deviations away from the mean of δ for the given sample.

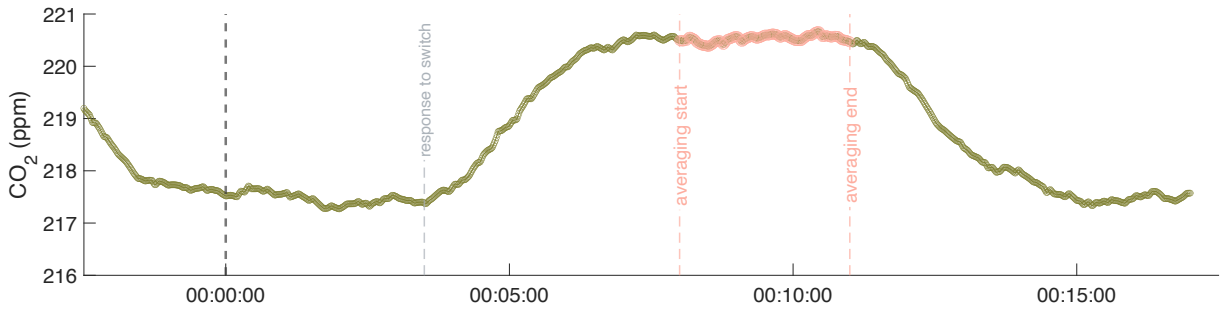

Figure 3.3 Illustration of the timing of data that is averaged with respect to the time of switching. The switch is marked with a vertical grey dashed line at time = 0.

A measure of short-term precision is provided by the spread in values of δ for a given sample-reference pair. On September 2, 2022 (Figure 3.2), the precision achieved in δ is ± 0.135 ‰ for a single measurement (1 SD). The precision of measurements for the eight runs performed between August 26, 2022 and September 8, 2022 is on average ± 0.16 ‰ for a single measurement. The level of measurement

precision declined slightly but steadily between September 8, 2022 and March 2023 (e.g., Figure 3.5, Figure 3.14).

3.2 Zero enrichment

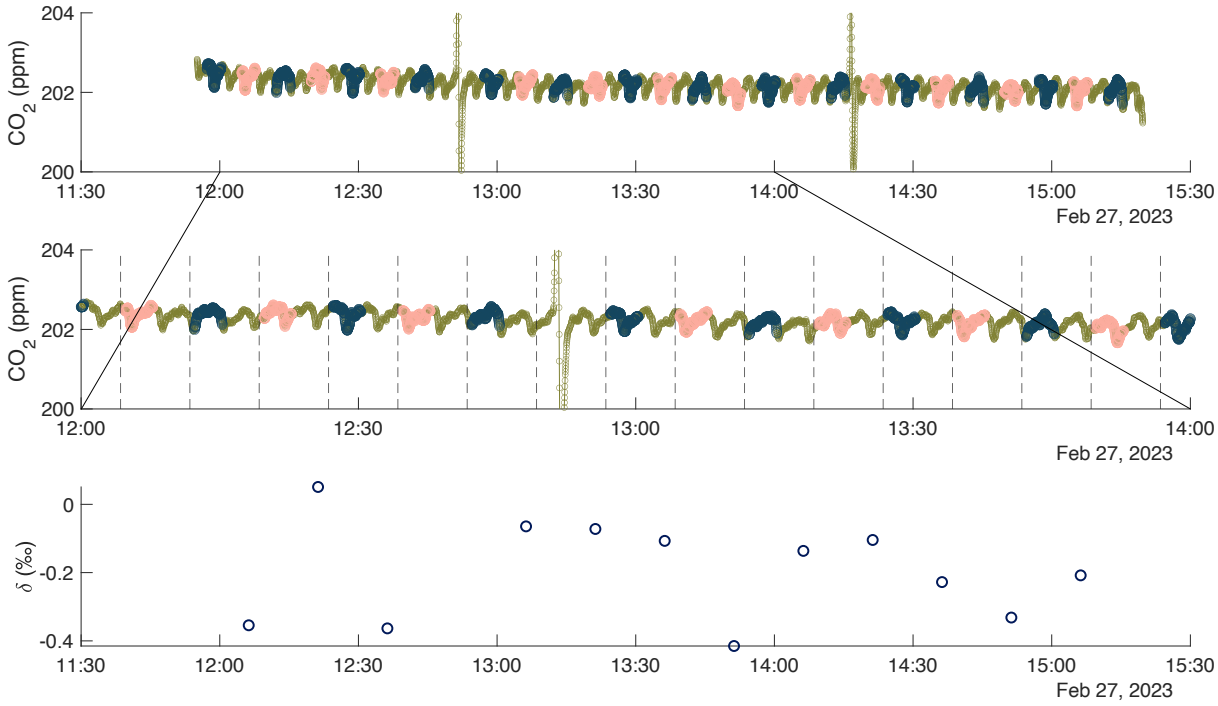

Figure 3.4 Same as Figure 3.2, but for a zero-enrichment run, in which sample and reference inlets are connected to the same source. CRDS signal impacted by bubbles (12:50, 14:35) is excluded from the calculation of δ. The dominant high frequency fluctuations apparent in the signal are related to liquid handling pump performance (discussed in Section 4.4.2).

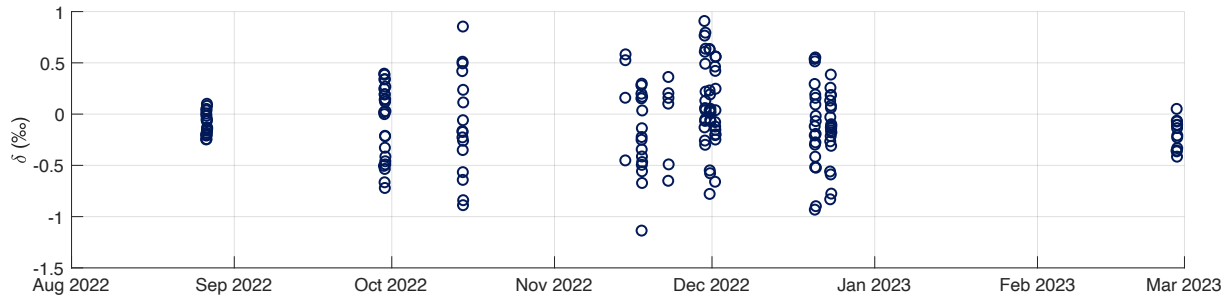

Figure 3.5 Values of δ (Equation 2) for zero enrichment runs between August 2022 and March 2023.

Runs were also carried out to calculate the “zero enrichment”, i.e., the apparent δ value when running the same seawater sample on both the sample and reference lines. These runs were carried out by connecting the sample and reference lines to a stainless-steel tee at the outlet of a seawater bag. Zero enrichment runs were performed on August 26, September 29, October 14, November 14, November 17, November 22, November 29, November 30, December 1, December 20, December 23, 2022 and on February 27, 2023. Sample output from February 27, 2023 is shown in Figure 3.4, and the calculated δ values across all runs are shown in Figure 3.5.

On average, the calculated zero enrichment δ values show a -0.06 ± 0.4 ‰ (1 SD) offset that is stable over time (Table 3.2). When aggregating δ values across days in which zero-enrichment was tested, the mean δ differs significantly from 0 (mean = -0.115, SD = 0.395, Student’s t-test (77) = -2.574, p = 0.0120). However, for a given day, the δ of zero enrichment is not significantly different from zero, and because the mean zero enrichment is relatively small, we do not use the zero-enrichment data to produce a correction factor. Oscillations appearing in Figure 3.4 are thought to originate from instability in the liquid handling pumps (discussed further in Section 4.4.2) and are not related to switching between sample and reference (marked with vertical dashed lines).

Table 3.2 Statistics of zero enrichment runs between August 26, 2022 and February 27, 2023. Differences in standard deviation between days are thought to arise from signal distortion by bubbles and oscillations in the pump delivery.

Date	n(δ)	Mean (‰)	Standard deviation (‰)	Standard error (‰)
August 26, 2022	19	-0.11	0.13	0.03
September 29, 2022	24	-0.11	0.4	0.08
October 14, 2022	16	-0.1	0.51	0.13
November 14, 2022	4	0.2	0.48	0.24
November 17, 2022	16	-0.15	0.5	0.12
November 22, 2022	6	-0.05	0.41	0.17
November 29, 2022	15	0.26	0.41	0.11
November 30, 2022	13	-0.02	0.42	0.12
December 1, 2022	13	0.05	0.37	0.1
December 20, 2022	19	-0.18	0.53	0.12
December 23, 2022	21	-0.11	0.36	0.08
February 27, 2023	12	-0.19	0.15	0.04

3.3 Calibration

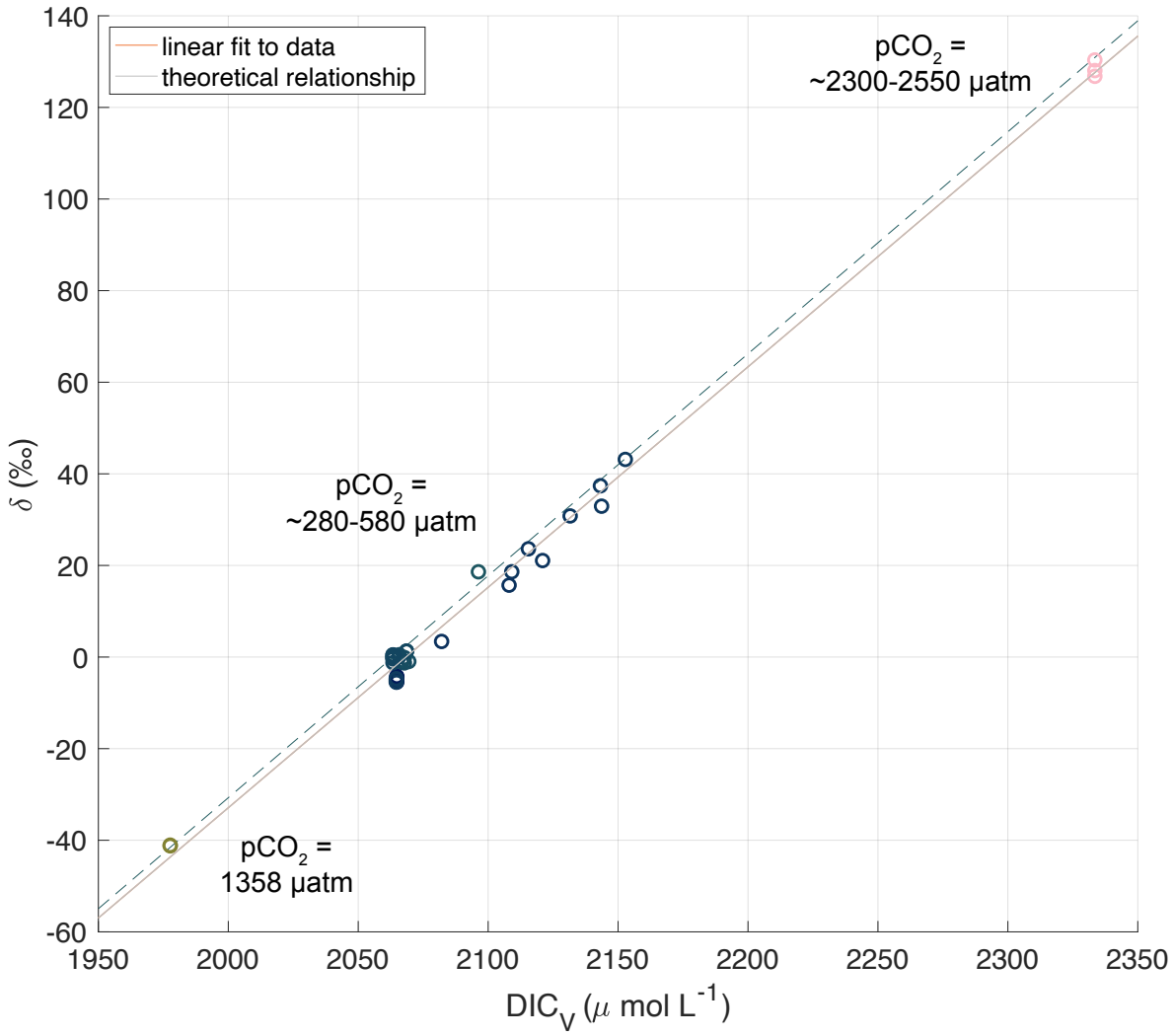

Figure 3.6 Measured δ referenced to seawater from JDCS-BagD vs. DIC_V of analyzed seawater samples. The solid line is the least squares linear fit to the data while the dashed line represents the theoretical relationship between DIC_V and δ based on Equation 3. Points are colored by and labeled with pCO_2 values.

To calibrate the contactor system, we ran seawater samples with known DIC_V quantities against one of two references (WHW-BagA between August 26, 2022 and February 5, 2023, JDCS-BagD between February 7, 2023 and March 2, 2023) (samples and references described in Table 3.1). These two references were also run against

one another on February 25, 2023 to derive a conversion for samples measured against WHW-BagA to being referenced against JDCS-BagD (such that JDCS-BagD becomes the zero value across all runs). Results are shown in Figure 3.6.

We computed two lines through the data, the first being a linear least squares fit and the second being a line that runs through the DICv of the reference and δ = 0 but has a slope defined by Equation 3, in which we replace $\mathcal{X}_{CO2}$ with DIC_V. The comparison of these two slopes provides a measure of the scale contraction, which estimates the degree by which the response variable under- (or over-) realize the "true" response. This comparison suggests that the scale contraction amounts to 0.68%, i.e., our observed response is 0.68% lower than the theoretical response. This scale contraction reflects the degree to which the CRDS signals are under-realized in the 7.5-minute switching scheme used here, suggesting that 7.5 minutes allows the CRDS signal to come very close to its full potential value.

The residuals in δ relative to the regression fit have a residual standard error of ± 2.5 ‰, suggesting an external precision of ± 5 μmol kg^{-1} for a seawater sample with DIC_M of 2000 μmol kg^{-1}. This precision is worse than was expected from short-term reproducibility suggested from the results prior to September 8, 2022 (Figure 3.2). Possible limitations to the performance of the contactor system are discussed in Section 4.

3.4 Contactor CO_2-removal efficiency

We estimate the efficiency *e* of CO_2 removal from the seawater stream (Equation 1) using a test that is based on the assumption that the system achieves 100%

efficiency at very low seawater flow rates. We varied the flow rate of seawater across 55 flow rates spanning 0.05 mL min^{-1} to 0.6 mL min^{-1}. As shown in Figure 3.7a, the CO_2 signal increases quasi-linearly with the flow at low flows, but the slope decreases towards higher flows. We interpret the deviation from an initial linear slope as reflecting a loss of efficiency in CO_2 extraction as the seawater spends progressively less time in the contactor at higher flow rates.

To resolve the initial linear slope, we fit a linear regression to the data at flow rates of <0.15 mL min^{-1} (Figure 3.7), with a point at zero flow, zero signal included in the fit. At 0.3 mL min^{-1} flow, the estimated extraction efficiencies are 95.6%, 94.5%, and 92.1% on October 1, February 17, and February 19, respectively. The February 19 efficiency test used a higher proportion of phosphoric acid (9:2 seawater to acid ratio, compared to the 9:1 ratio otherwise used throughout the study). The lower efficiency on February 19 is not understood but may be related to slower diffusion of CO_2 in concentrated acid leading to slower escape of CO_2 from the core of the contactor. Because *e* cancels in the ratio $X_{CO2,reference}/X_{CO2,reference}$ in Equation 2, a precise knowledge of *e* is not relevant for calibrating the system. Nevertheless, high efficiency is desirable, both to reduce sensitivity to temperature fluctuations or any factors which might alter the efficiency and to obtain higher CO_2 signals on the CRDS. Potential causes of below-100% efficiency are discussed in Section 4.2 and Section 4.4.4.

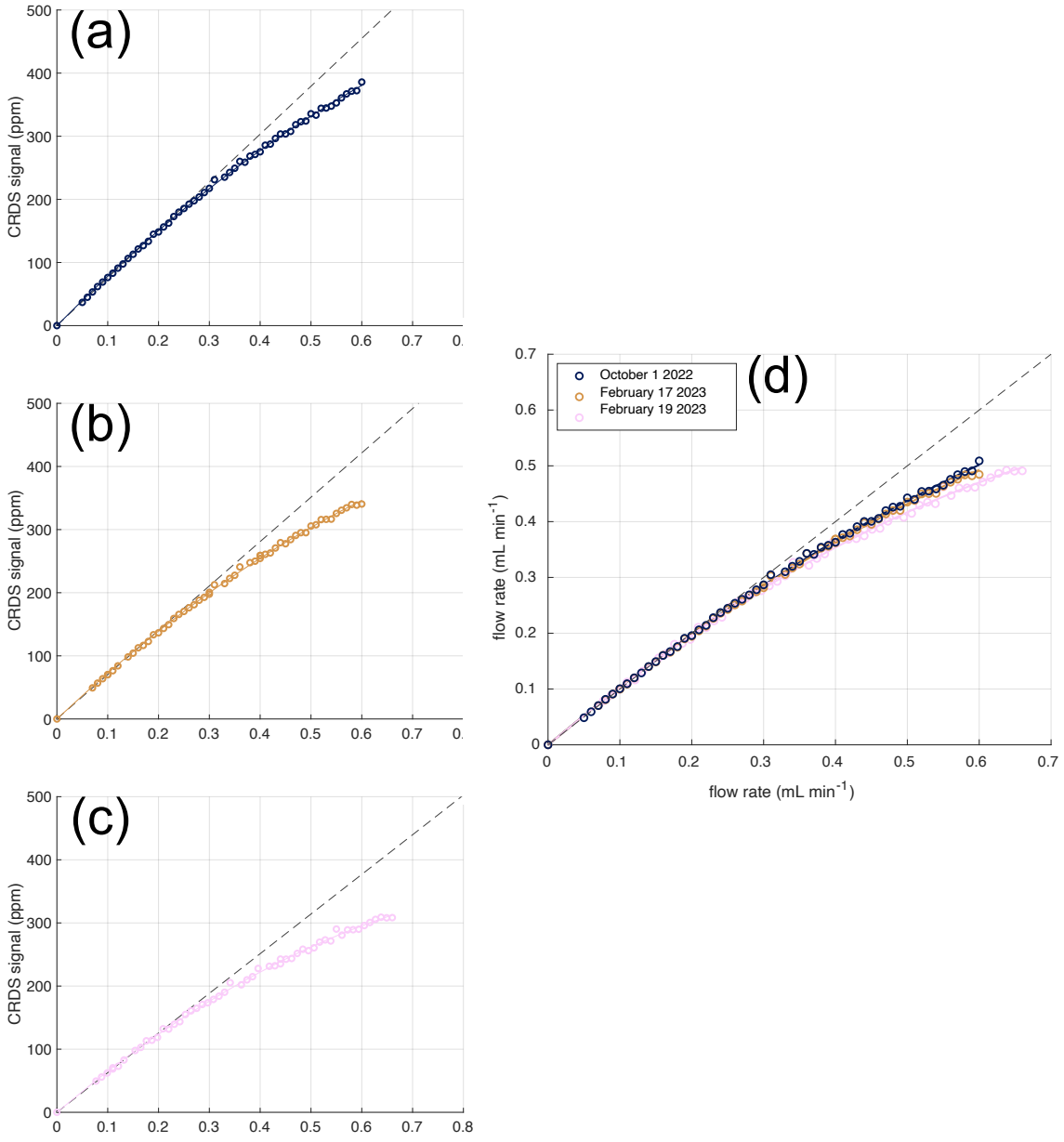

Figure 3.7 Illustration of CO_2 removal efficiency on three days (normalized to slope = 1 and overlaid in panel (d)) and the relationship between CRDS CO_2 signal and liquid flow rate through the system on October 1, 2022 (a), February 17, 2023 (b) and February 19, 2023 (c). A line is fit to estimate the rate of change at low flow rates, which is taken as the CO_2 signal at 100% CO_2 extraction efficiency. A parabolic fit to the data that is forced through the origin is also shown, which is used for interpolation. The data and parabolic fits are normalized to their respective slopes at low flow and plotted together in (d). The dashed line in panel (d) represents the assumed signal at 100% extraction, and the proportions of the curves to that line represents the efficiency achieved at a given flow rate. The seawater and acid were flowed at a proportion of 9:1 on October 1, 2022 and February 17, 2023, and 9:2 on February 19, 2023.

3.5 Impacts of differences in sample salinity

To test if the residuals of the data to the calibration (Figure 3.6) could be explained by salinity differences, we prepared samples with a range of salinities but with only small variations in DIC and TA (Table 3.3). These samples were prepared using 500 mL glass bottles filled with seawater from a single carboy containing seawater collected off the Scripps pier poisoned with $HgCl_2$. Seawater was siphoned from the carboy into an Erlenmeyer flask, into which NaCl was added. Two bottles were then filled from the Erlenmeyer flask. This process was repeated five times with different quantities of NaCl additions. All 10 bottles were analyzed in the contactor system over two days, with each bottle analyzed for salinity and alkalinity after analysis on the contactor system. Two bottles were also independently analyzed for DIC_V via manometry on the same day that they were analyzed using the contactor system. DIC_V for all other bottles were assigned as the average DIC_V between the two samples that were analyzed manometrically.

We found that samples having a lesser salinity relative to the reference tended to yield δ values that fall below the linear regression fit to all δ values (Figure 3.8), though the relationship is weak. This relationship suggests a need for additional calibrations for seawater samples at different salinities to better resolve this potential effect.

Table 3.3 Seawater bottles used for salinity calibration. The seawater was collected at Scripps pier and manipulated via NaCl additions. Bottles were created in duplicate, which are listed together in each row. Salinity and alkalinity for bottles listed first in each table cell were analyzed independently after being run on the contactor system. Only two of the 10 bottles (JDCS-Sa-20 and JDCS-Sa-26) were independently analyzed for DIC content. DIC values marked with asterisks were calculated as the average of the two analyzed bottles. pCO_2 is calculated using the independently-measured DIC and TA values.

Name	Salinity (ppt)	DIC_M ($\mu mol\ kg^{-1}$)	DIC_V ($\mu mol\ L^{-1}$)	TA ($\mu mol\ kg^{-1}$)	pCO_2 at 20˚C (µatm)
JDCS-Sa-26 JDCS-Sa-21	33.3	2021.2	2068.6	2221.1	491.0
JDCS-Sa-27 JDCS-Sa-22	34.52	2016.6*	2065.8*	2217.4	502.4
JDCS-Sa-23 JDCS-Sa-28	35.82	2016.6*	2067.8*	2214.0	528.1
JDCS-Sa-24 JDCS-Sa-29	36.92	2016.6*	2069.5*	2211.5	549.7
JDCS-Sa-20 JDCS-Sa-25	38.3	2012.0	2066.9	2208.6	562.1

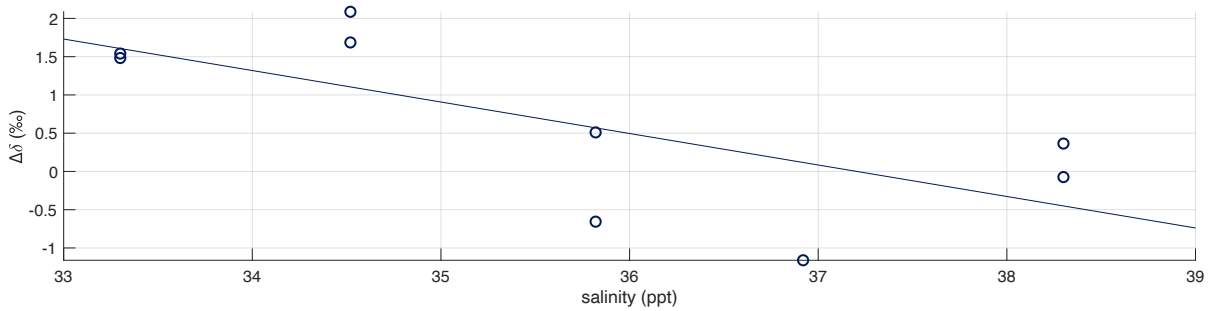

Figure 3.8 The difference between measured δ values and δ via the linear regression against DIC_V (Figure 3.6), denoted ∆δ, plotted against the salinity of a given sample.

3.6 Impacts of differences in sample TA

Table 3.4 Bagged standards used for assessment of contactor system on sample TA. The seawater was collected at Scripps pier and manipulated via additions of NaOH, DI water, or HCl (see Description column). All pCO_2 values are calculated at 20 ˚C.

Name	Description	Use	DIC_M (μmol kg^{-1})	DIC_V (μmol L^{-1})	TA (μmol kg^{-1})	pCO_2 at 20˚ C (μ_{atm})	Salinity (ppt)
JDCS-TA-B1	Filtered pier water plus NaOH	TA calibration (high TA)	2017.4	2064.8	2881.7	62.9	33.3
JDCS-TA-B2	Filtered pier water plus DI water	TA calibration (control)	2017.3	2064.6	2268.6	384.4	33.3
JDCS-TA-B3	Filtered pier water plus HCl	TA calibration (low TA)	2004.7	2051.7	1614.6	12176.7	33.3

To isolate any effects of differences in TA on δ, we analyzed seawater from three bags with differing TA (Table 3.4). Each bag of seawater contained the same source seawater, which was passed through combusted 47mm GF/F filters during filling. A small volume of 85% HCl solution was injected into one of the bags and 22% NaOH solution into another. A small volume of DI water was injected into the bag that received no acid or base. These additions also changed pCO_2 in the samples, with the low TA bag having a high pCO_2 of ~ 12247 ppm. These runs were carried out against the reference (JDCS-BagD) which has a pCO_2 of 486 μatm.

We found that δ values calculated for the low TA sample fell below the regression line in Figure 3.6. Examining the switching data, the signal appears to overshoot the higher DIC reading and undershoot the lower DIC reading (Figure 3.9) specifically when running the low-TA sample. We hypothesize that polymeric components of the liquid line upstream of the contactor absorb and desorb CO_2 according to concentration gradients, such that in the presence of a high pCO_2 sample,

CO_2 is absorbed into the polymers and is released when the flowed seawater is switched to a lower pCO_2 sample. The lines themselves are made from Hastelloy, but the Kloehn valve and M6 pumps both contain polymeric components. Their location in the line exposes them to the initial pCO_2 of the sample and reference as the Kloehn valve switches back and forth. This could explain the CO_2 depletion (and signal undershoot) of the lower DIC, higher pCO_2 sample as CO_2 is absorbed into the polymers before stabilizing, and the CO_2 overload (and signal overshoot) in the higher DIC, lower pCO_2 reference sample as CO_2 is released from the polymer into the liquid stream again before stabilizing.

Rather than resolving a true sensitivity to TA, these tests suggest a limitation of the current configuration of the system. Even though the 7.5-minute switching cycle appears sufficiently rapid to achieve ~100% replacement of sample and reference within the contactor, it appears insufficient to condition the lines to changes in initial variations in pCO_2 between sample and reference. Despite this limitation, we nevertheless processed the jogs with the normal windowing to yield δ values. With the over- and undershoots in the CRDA signal arising from pCO_2 differences between the sample and reference, using the same sample-reference switching scheme to calculate δ would result in the absolute value of δ being artificially large (large difference in CRDA signal between sample and reference), with the overshoot integrated into the reference signal and undershoot integrated into the sample signal. Similarly, we expect a sample with higher DIC_V and higher pCO_2 than the reference to have an artificially small positive δ as the CRDA signals converge with the addition of CO_2 to the lower-DIC_V reference

signal, resulting in these δ again falling below the fitted and theoretical δ-DIC_V curves. These relationships are detailed in Table 3.5.

We note that the CRDS signal appears to respond more quickly to switches when running the JDCS-TA-B1 and JDCS-TA-B2 bags against JDCS-BagD (Figure 3.9, response of ~60 seconds compared to the standard 3.5 minutes). Because using the standard integrating scheme includes data from the sweepout in this scenario, we reduce the amount of data averaged from 8 to 11 minutes post-switch to 8 to 8.5 minutes post-switch. The faster response time for these samples has yet to be explained.

Table 3.5 Impacts of differences in sample and reference pCO_2 on CRDS CO_2 signal and subsequent calculation of δ.

Sample DIC_V	**Sample pCO_2**	**Impact on signal**		**Expected signal**	**Actual signal**	**Above or below fit in Figure 3.6**
Higher	Higher	Sample signal loses CO_2, reference signal gains CO_2	Signals converge	Positive δ	Positive δ with smaller absolute value (less positive)	Below
Lower	Higher	Sample signal loses CO_2, reference signal gains CO_2	Signals diverge	Negative δ	Negative δ with larger absolute value (less positive)	Below
Higher	Lower	Sample signal gains CO_2, reference signal loses CO_2	Signals diverge	Positive δ	Positive δ with larger absolute value (more positive)	Above
Lower	Lower	Sample signal gains CO_2, reference signal loses CO_2	Signals converge	Negative δ	Negative δ with smaller absolute value (more positive)	Above

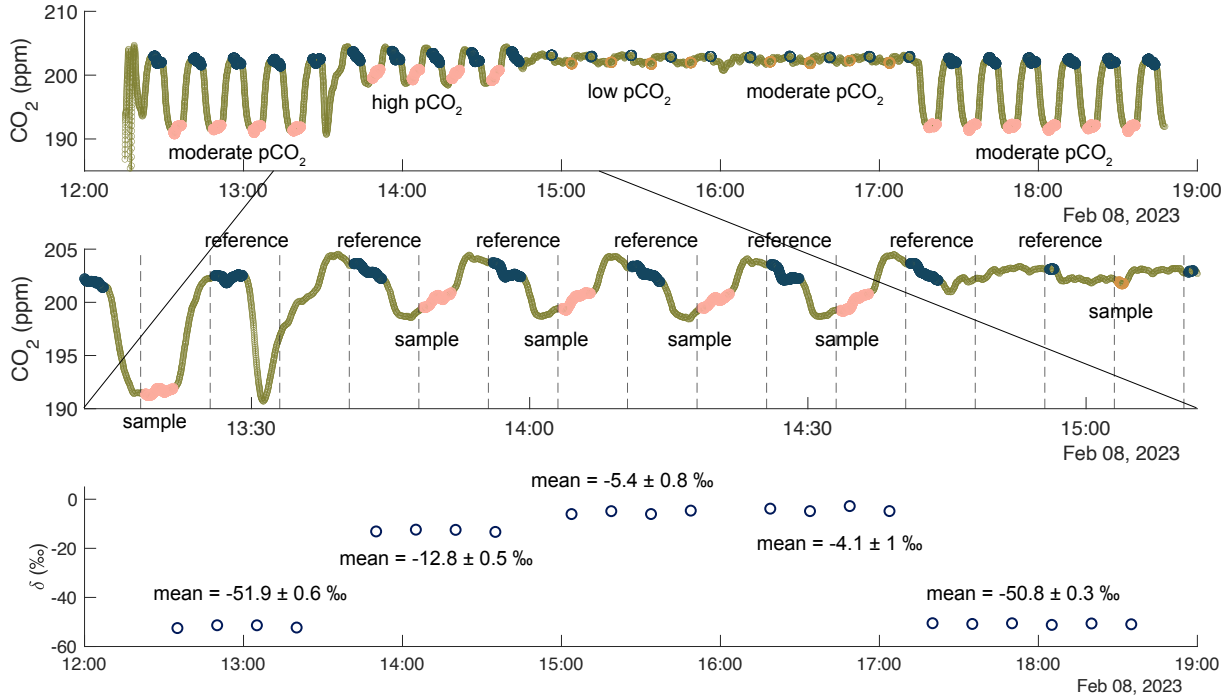

Figure 3.9 Same as Figure 3.2, for referencing a moderate-pCO_2 low-DIC sample (JDCS-BagC, 12:15 – 13:30), a high-pCO_2 sample moderate-DIC sample (*JDCS-TA-B3, 13:30 – 14:15)*, a low-pCO_2 moderate-DIC sample (JDCS-TA-B1, 14:15 – 16:00), a moderate-pCO_2 moderate-DIC sample (JDCS-TA-B2, 16:00 – 17:15), and again the same moderate-pCO_2 low-DIC sample (JDCS-BagC, 17:15 – 18:45) against a reference (JDCS-BagD). The middle panel shows the over- and under-shooting of the signals of the sample (pink) and reference (blue) for the high-pCO_2 sample. For JDCS-TA-B1 and JDCS-TA-B2, the response of the system to a change in input occurs faster than for the other samples (60 seconds vs. 210 seconds), so a shorter timeframe (30 seconds vs. 180 seconds) of data is integrated in the calculation of δ. This data is marked in orange.

4 Further Discussion

4.1 Effects of water line pressure on δ

We tested the effects of increasing and decreasing the pressure of the water lines both upstream and downstream of the liquid handling pumps on δ. This was achieved by raising and lowering the seawater inputs to the pumps (upstream) and opening and closing the water line needle valve (downstream). The water line pressure

upstream of the pumps did not appear to affect δ (Figure 3.10). The CRDS CO_2 signal was sensitive to changes in pressure and decreased at higher pressure downstream of the pumps. Water line flow data collected by the balance downstream of the contactor indicated that the flow rate changed according to changes in water line pressure, thus we attribute the pressure dependence of the CRDS signal to the pumps' backpressure sensitivity. However, the signals for both sample and reference were impacted equally such that the δ values remained consistent across pressures. We thus show that changing the pressure in the water lines in either location does not significantly impact δ values.

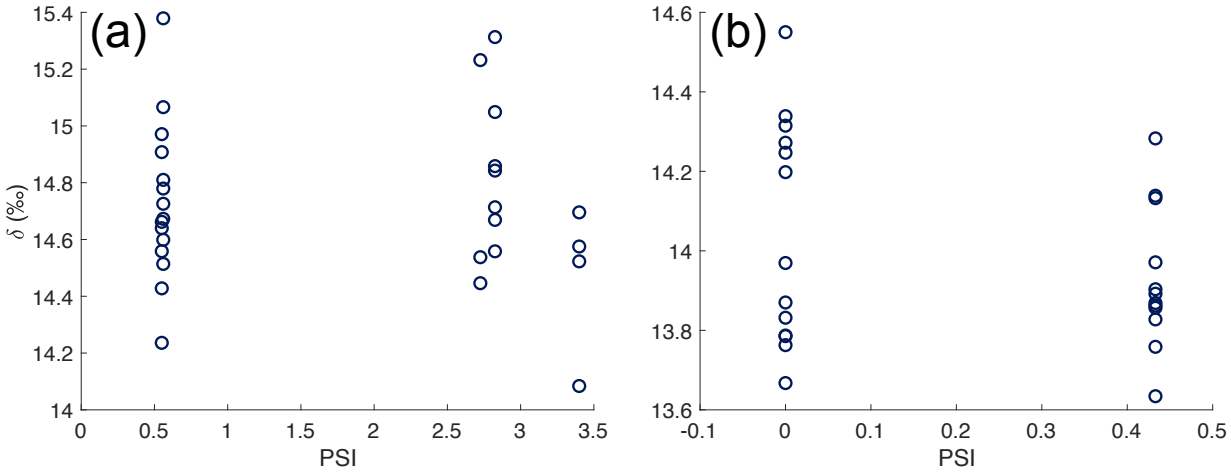

Figure 3.10 Relationship between inlet water pressure measured on September 13, 2022 δ (a) and between pressure of the water line downstream of the pumps as measured by a pressure gauge (see Figure 3.1) and δ measured on October 6, 2022 (b).

4.2 Kinetics of mixing and hydration steps

Here we discuss aspects the chemical kinetics governing the system behavior. Complete acidification of the sample before reaching the contactor is dependent on the

timescale of the acidification reaction and the timescale of diffusive mixing of acid in seawater in relation to the liquid transit time in the mixing line.

Of the chemical steps involved in the seawater acidification reactions, the slowest is the conversion of bicarbonate and H^+ ions to CO_2 and H_2O (called the dehydration reaction), which ultimately determines the speed of the overall conversion of dissolved inorganic carbon species to CO_2 (Zeebe and Wolf-Gladrow, 2001). Acidifying the seawater with 85% H_3PO_4 in a 9:1 ratio results in a solution of pH ≈ 2. Using a pH of 2, the timescale of decay in the conversion from HCO_3^- to CO_2 can be calculated using the rate constant 2.66 * 10^{-4} kg mol^{-1} sec^{-1} (Johnson, 1982; Zeebe and Wolf-Gladrow, 2001) The e-folding time for this reaction to approach equilibrium is 2.1*10^{-2} seconds, which is much shorter than the transit time of the seawater sample through the line of Hastelloy before reaching the contactor:

$$T_{transit} = \frac{L}{volume\ flow} * \pi r^2 = \frac{154\ cm}{0.3\ mL\ min^{-1}} * \pi * (0.038\ cm)^2 = 2.33 \text{ minutes}$$

where L (length) and r (radius) are dimensions of the Hastelloy tubing. Thus, even the slowest reaction will not limit the conversion and extraction of CO_2. The line of Hastelloy upstream of the contactor also serves the purpose of increasing the physical interaction between the acid and seawater before the mixture reaches the contactor membrane. The magnitude of interaction is in part governed by the diffusivity of phosphoric acid in water. We use 85% phosphoric acid in a 1:9 ratio with seawater so that the resulting phosphoric acid percentage becomes 8.5%. We use the diffusivity for 8.5% phosphoric acid at 25.15 ˚C of 7.8*10^{-6} cm^2 sec^{-1} (Lang et al., 2014) to calculate the diffusion timescale with the expression:

$$T = \frac{r^2}{D}$$

where *r* is the radius of the tubing and D is the diffusivity. Thus, for a tubing radius of 0.038 cm, the timescale of diffusion becomes:

$$T = \frac{(0.038\ cm)^2}{7.8 * 10^{-6} cm^2\ \mathrm{sec}^{-1}} = 185.13\ \mathrm{seconds} = 3.09\ \mathrm{minutes}$$

Though the diffusion timescale is longer than the transit time (ratio of diffusion time to transit time = 1.32), the flows converge abruptly at a tee just downstream of the pumps. Assuming that mixing of the seawater and acid is achieved only through molecular diffusion, we conclude that the 2.33-minute transit time of the solution through the Hastelloy line before reaching the contactor is insufficient time for the solution to mix. Nevertheless, this appears not to be a major issue because of the apparently high efficiency of CO_2 extraction in the contactor (Section 3.4).

4.3 Impact of dissolution of gas into water line

The bulk flow of carrier gas (N_2) into the CRDA can in principle be modulated by gain or loss of N_2 and O_2 from the liquid via diffusion through the contactor. To show that this effect is small we take the solubility of N_2 gas into seawater with a salinity of 35.5 ppt at 20˚C to be 554.51 μmol kg^{-1} (Weiss 1970). For a water stream of 0.27 mL min^{-1} (assuming a seawater density of 1.02 kg L^{-1}), 0.15 μmol of N_2 gas at this solubility can dissolve into the water flow per minute. An N_2 gas stream of 56 sccm is equivalent to a flow of 0.0025 mol min^{-1} at STP. Dividing the rate of dissolution of N_2 gas into the seawater stream by the flow rate of the N_2 gas yields a ratio of 6.1 * 10^{-5}, meaning that complete dissolution of N_2 gas into the liquid stream (clearly an extreme scenario) could

impact a CO_2 signal of 200 ppm by a negligible 200 ppm * 6.1 * 10^{-5} = 0.0122 ppm. For a seawater sample with a typical dissolved oxygen concentration of 243.75 µmol L^{-1} (7.8 mg L^{-1}), assuming that 100% of dissolved oxygen is extracted into the carrier gas, 0.066 µmol O_2 is added to the carrier gas per minute. This O_2 gas adds a volume of 0.0015 mL min^{-1} to the 56 sccm carrier gas flow (not including the volume from extracted CO_2), resulting in a 0.0027% increase in the gas flow rate, causing a change in the CO_2 signal of a negligible 200 * 2.7 * 10^{-5} = 0.0054 ppm.

We consider instrument noise in the CRDS gas analyzer as having a negligible contribution to overall system measurement uncertainty. For data averaged over 7.5 minutes, instrument precision is estimated at $10^{-2.9}$ ppm via an Allan Deviation plot published by Picarro for the G2301 analyzer. A 10-fold deterioration in instrument precision would increase this value to $10^{-1.9}$ ppm, which is negligible in scale compared to other sources of noise (e.g., pump oscillations (discussed in Section 4.4.2)).

4.4 Limitations to performance

4.4.1 Stability of bagged references

We elected to use the multi-layer foil sampling bags to store seawater references assuming that the absence of a gaseous headspace would reduce drift in the reference DIC. Our data nevertheless show clear indicators of drift in the DIC in the bags. The first indicator is based on looking closely at a possible time dependence of the relationship between δ (referenced against JDCS-BagD) shown in Figure 3.11 and DICv as inferred from the contactor system using Equation 3. Figure 3.11 shows a ~2.4 µmol L^{-1} $month^{-1}$ rise in the mismatch between the DIC_V values obtained using the contactor system

versus the expected DIC_V values based on Equation 3. This drift suggests a small but clear upward drift in DIC_V of the JDCS-BagD reference, and may explain residuals from the linear fits in Figure 3.6. Because Figure 3.6 shows bottle samples, which were measured independently on the day that they were run on the contactor system, referenced against JDCS-BagD, the trend in Figure 3.11 is likely a relatively accurate representation of the drift in this reference.

The second indicator is based on looking at changes in δ values between pairs of bags (i.e., when using one as the reference for the other). The drift in δ when running the “low DIC” bag (JDCS-BagC) used throughout runs in 2023 against JDCS-BagD as reference is particularly large (0.8 ‰ day^{-1}, Figure 3.13). The drift in δ when running WHW-BagA against WHW-BagB (Figure 3.12) amounts to roughly -0.02 ‰ day^{-1}, which is surprisingly low considering the strong smell and changing alkalinity of WHW-BagA (suggesting bacterial respiration occurring in the water contained), but it is possible that the bags, which both were filled from the same source at the same time and had strong smells, were drifting concurrently. Because JDCS-BagC was referenced against JDCS-BagD, which appears to have been drifting towards higher DIC, it is possible that the drift in δ shown in Figure 3.13 underestimates the actual drift in DIC in JDCS-BagC. Drift in the reference reduces the overall precision at which the measurement system can be calibrated by increasing the uncertainty of intercomparison of δ values calculated from different days.

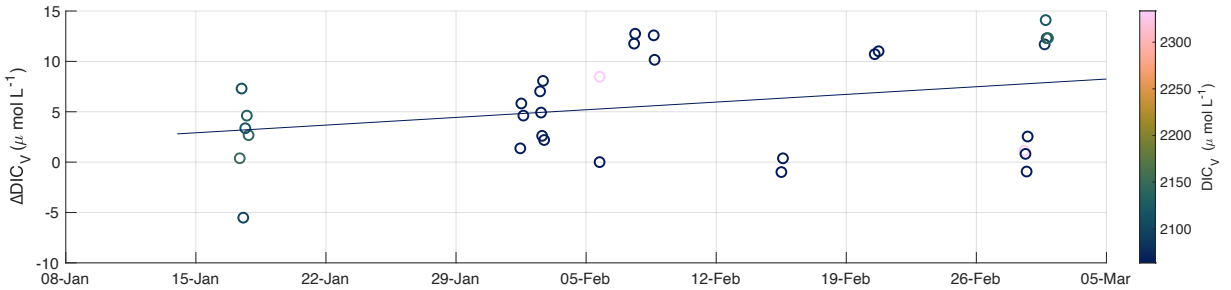

Figure 3.11 Mismatch between measured and theoretical values of DIC_V over time for all data points shown in Figure 3.6 (slope = 0.08 µmol L^{-1} day^{-1}, referenced against JDCS-BagD). Datapoints are colored by DIC_V of the given sample.

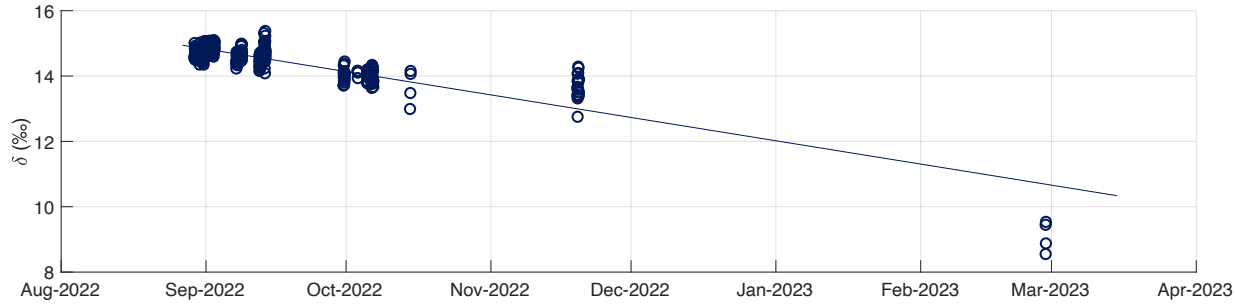

Figure 3.12 Values of δ for WHW-BagB referenced against WHW-BagA between August 29, 2022 and February 27, 2023 (slope = -0.02 ‰ day^{-1}).

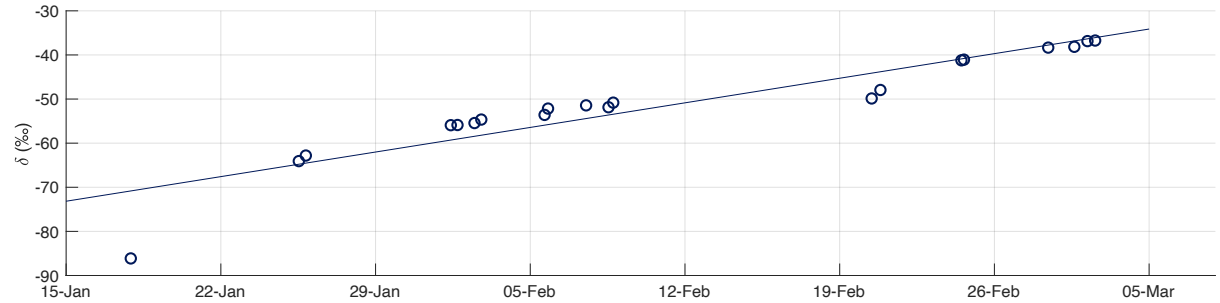

Figure 3.13 Values of δ JDCS-BagC (“low DIC bag”) when referenced against JDCS-BagD between January 17, 2023 and March 2, 2023 (slope = 0.8 ‰ day^{-1}).

4.4.2 Stability of pumps

The stability of the CRDA CO_2 signal is in part dependent on the stability of liquid delivery rate by the two pumps flowing seawater and acid. While the liquid delivery appears to be stable on timescales of > 5 minutes (as measured through liquid outflow data collected on a balance (Figure 3.1)), oscillatory patterns in the CRDA signal are detectable with a period of ~2-3 minutes (Figure 3.15). We attribute these oscillations to variations in liquid handling pumps because (1) the oscillation period is highly consistent within a day's run (between 2 and 2.75 minutes depending on the day, with a standard deviation of < 1 second), suggesting an electronic source, (2) the amplitude of the oscillations has been shown to rise when the water line pressure downstream of the pump increases, and (3) the oscillation amplitude rises when the water line pressure upstream of the pumps decreases. The second and third factors both affect the pressure gradient experienced at the pumps, increasing the strain on the pumps.

The amplitude of the high-frequency oscillations in the CRDA signal, while in part dependent on the pressure gradients at the pumps, has also appeared to increase overall over the past six months (Figures 3.14). Comparing actual volume delivery (after accounting for density differences between seawater and 85% phosphoric acid) to the prescribed volume delivery also suggests a longer-term decline in performance, with the actual volume delivery equaling 99% of the prescribed delivery in October 2022 and declining to 90% in February 2023 (Figure 3.14). Finally, mass flow data as recorded by balance measurements shows that when compared to flow rate changes on October 1, 2022, the change in actual flow rate on February 17, 2023 responds much more slowly to a change in prescribed flow rate in February 2023 (Figure 3.16).

The oscillations cause inconsistencies in the integrated CO_2 signals for sample and reference that decrease the precision of the resulting δ values. This issue is apparent in the decreased precision of data collected in later months.

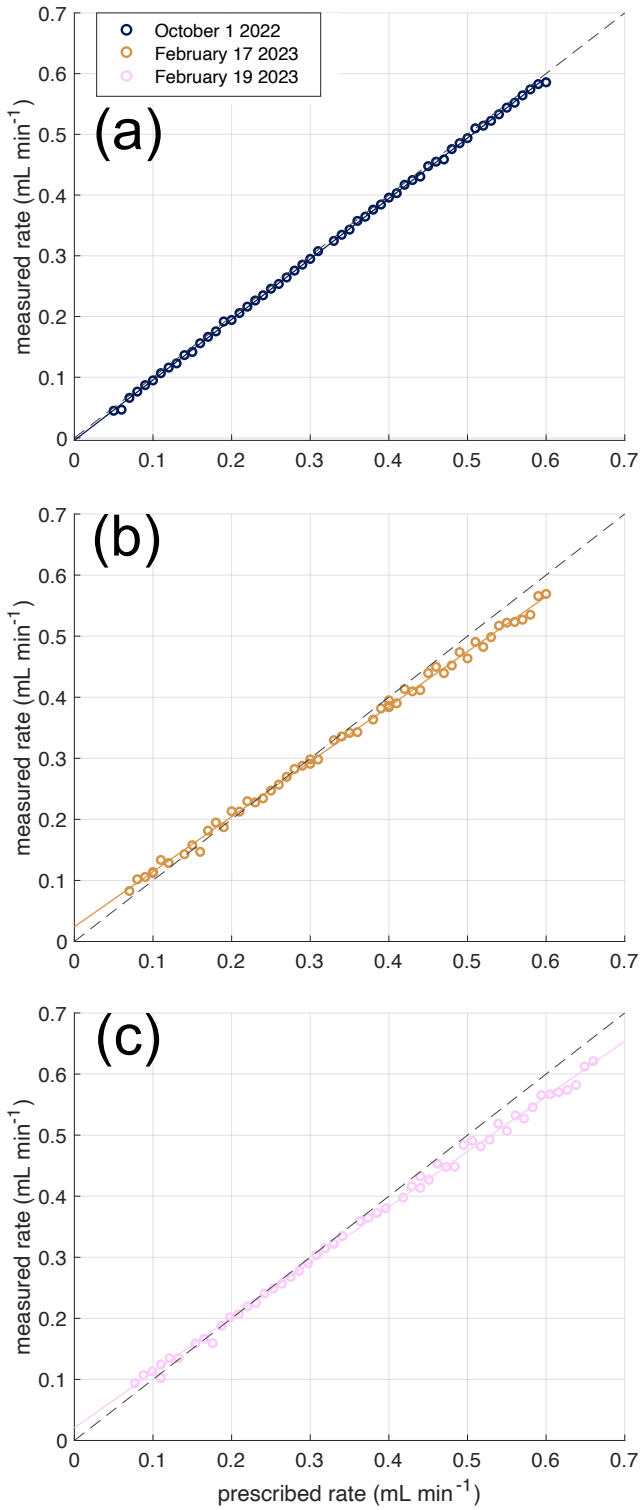

Figure 3.14 Relationship between prescribed pump rates (flow rate as set by computer) and measured liquid flow rate through monitoring changes in mass output for October 1 (a), February 17 (b) and February 19 (c). Seawater and acid are flowed at a proportion of 9:1 on October 1, 2022 and February 17, 2023, and 9:2 on February 19, 2023.

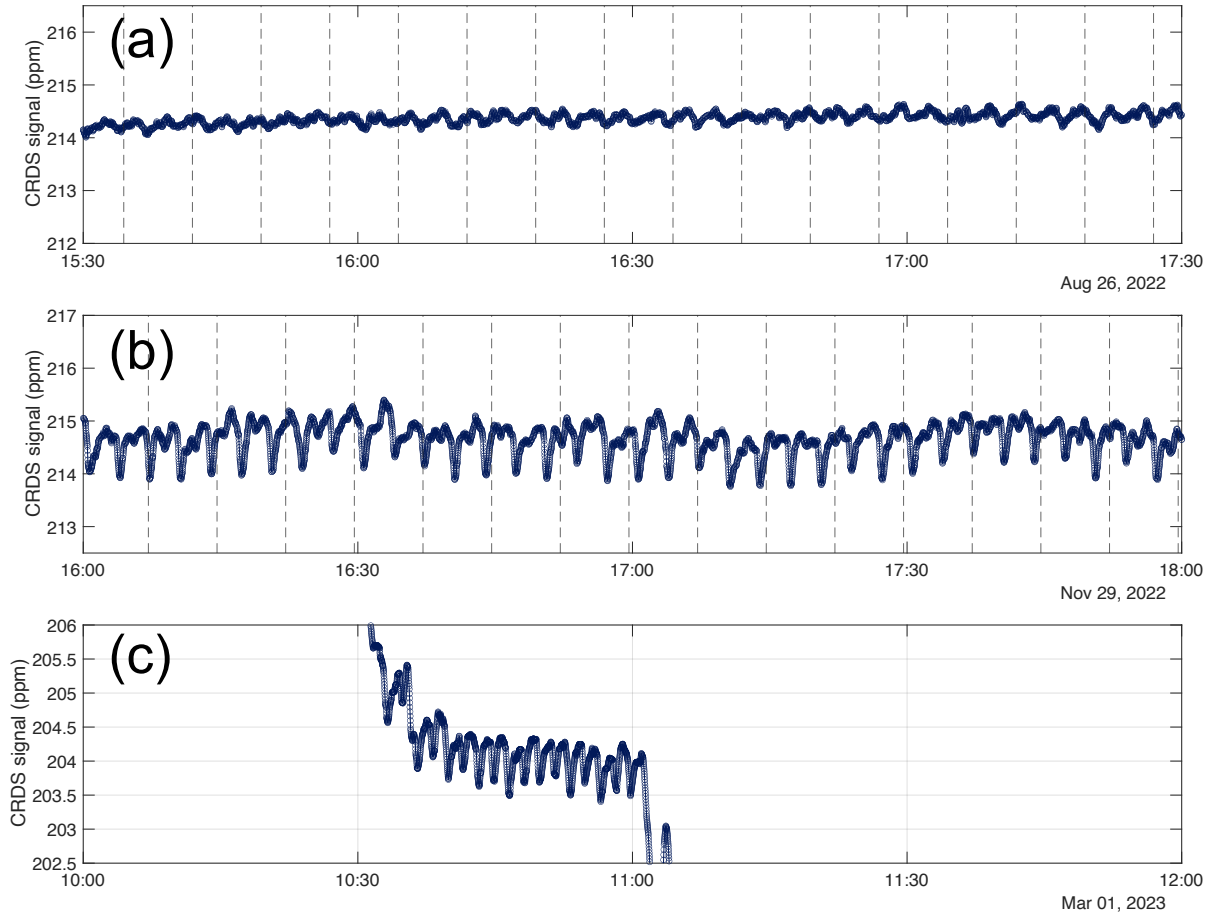

Figure 3.15 Illustration of high-frequency oscillations in the CRDS CO_2 signal. Data in (a) and (b) were collected during zero enrichment runs (switch times are marked with vertical dashed lines) and data in (c) was collected when seawater was connected directly to the pump with no switching.

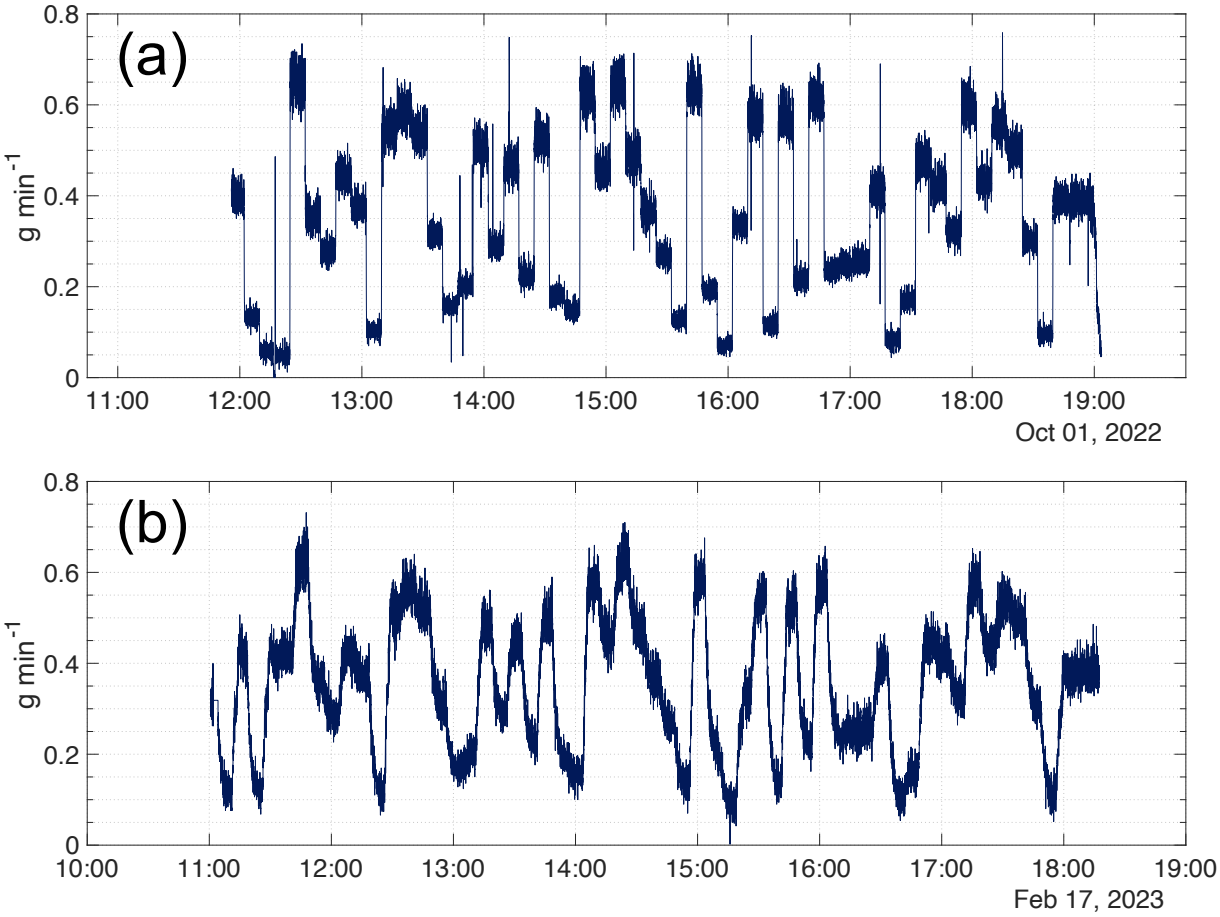

Figure 3.16 Liquid flow rate through system approximated by rate of seawater effluent onto balance during runs on October 1, 2022 (a) and February 17, 2023 (b) when prescribed seawater pump rates were changed rapidly according to the same regimen (regimen used for estimating contactor efficiency).

4.4.3 Stability of gas flow

Another source of instability in the system is the gas flow, which is sensitive in the current configuration to temperature changes in the needle valves that determine the gas flow rate. We found through experiments in which the needle valve was heated that the rising temperature was correlated with reduced gas flow rate. From a rough estimation, we found that an increase in temperature of 0.1 ˚C changes pressure by 0.86% and flow by 1%, which altered the CO_2 signal by 1%. However, this relationship

is not linear and appears to depend on other factors. While δ values are independent of gas flow rate if the flow remains stable across analysis of both sample and reference in the δ determination, the temperature of the gas flow cannot be controlled and may vary over the course of the day and may unevenly impact analyses of sample and reference, decreasing the precision of the δ measurements.

4.4.4 Limited sample-membrane interfacing

The contactor strips CO_2 from water at the membrane wall where the water touches the membrane surface, whereas water at the core of the membrane tubing loses CO_2 only by diffusion. The time scale for CO_2 to diffuse from the center to the wall is thus relevant to the contactor efficiency. The transit time of the solution in the contactor is:

$$T_{transit} = \frac{L}{volume\ flow} * \pi r^2 = \frac{118\ cm}{0.3\ mL\ min^{-1}} * \pi * (0.0305\ cm)^2 = 1.15 \text{ minutes}$$

Taking a diffusivity of CO_2 in seawater of $2 * 10^{-5}$ cm^{-2} sec^{-1} (Park and Choi, 2020) yields a characteristic timescale of diffusion as a function of the membrane radius:

$$T = \frac{r^2}{D} = \frac{(0.038)^2}{2 * 10^{-5}} = 3.1 \text{ minutes}$$

such that the ratio of diffusion time to transit time = 2.7. In early experiments, we attempted to address this issue in the past by inserting a wire into the contactor membrane to eliminate a center core of seawater, but the liquid handling pumps were not able to work against the added resistance. We choose to leave the membrane as is and accept that the possible incomplete contact of seawater with the membrane contributes more to a reduction in extraction efficiency and overall precision.

4.4.5 Bubbles

Thanks to the transparency of the glass housing for the contactor, we have been able to visually detect the transit of air bubbles through the length of the contactor. These bubbles are followed by aberrations in the CRDA signal (Figure 3.17), with small bubbles resulting in small jumps of ~1% of the signal (either up or down in CO_2) lasting 1-2 minutes, and large bubbles resulting in high amplitude, short period and tight sinusoid (deep decline followed by large spike) of ~7-15% (the drop having a greater amplitude), then a slow decline to the original signal level, the whole process lasting as long as 7 minutes. These data are selected for elimination from δ calculations by eye, and δ are thereafter filtered to remove any values > 2 SD from the mean, which can catch CRDA signals impacted by smaller bubbles or residual anomalies from larger bubbles.

We found it possible to limit bubble formation by increasing the pressure of throughout the lines downstream of the pumps by adjusting the needle valve upstream of the balance in Figure 3.1. This action reliably reduces bubble formation but carries the risk of increasing the water line pressure to a degree that induces higher oscillations in the CRDA signal originating from the liquid handling pump. Higher water pressure also increases the risk of failure of the glued Hastelloy-Teflon connections fail due to too-high pressure in the water line.

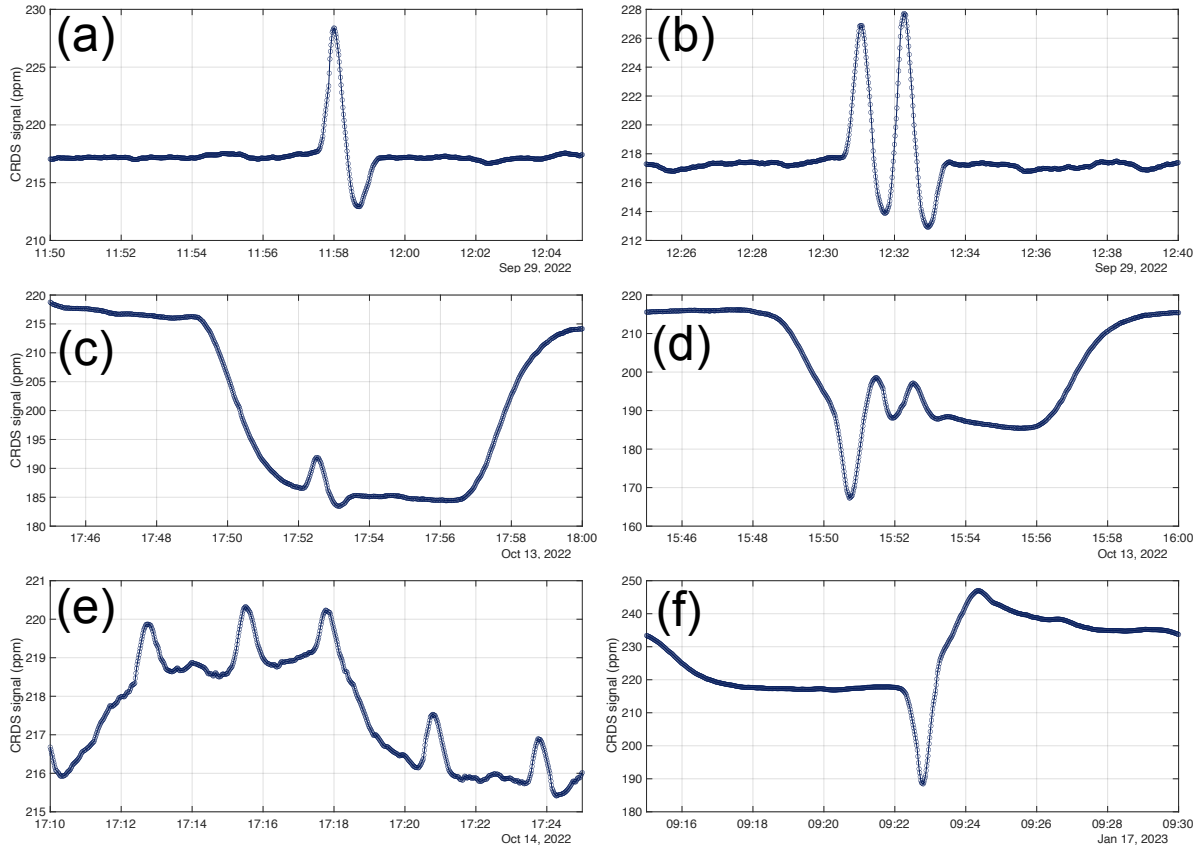

Figure 3.17 Examples of signal aberrations arising from the formation of bubbles in the liquid line (a-e) or introduction of air into the liquid line (f).

4.4.6 Retention of CO_2 in polymers

We have shown through analyzing samples with high pCO_2 relative to the reference that the system is sensitive to and retains a memory of such pCO_2 differences, which impacts calculations of δ. We attribute this “memory” to the presence of polymers in the wetted materials of the Kloehn valve and M6 pump, which are sequentially exposed to sample and reference during switching. Further, the VICI valve also contains polymer wetted materials, and any switching between samples using the VICI valve is also subject to issues of CO_2 absorption and desorption. A significant limitation to the existing setup is that the time required for CO_2 dissolved in these

elastomers to equilibrate with water is equal to or longer than the 7.5-minute switching period between sample and reference. Though it is possible to integrate a shorter, stabilized segment of CRDA signal to avoid including the over- and undershoots in calculating δ, averaging less data increases the influence of oscillatory noise in the CRDA signal and decreases the precision in δ. Extending the switching timescale between sample and reference from 7.5 minutes increases the influence of longer-term drift into the δ calculations, also reducing precision in δ.

5 Summary of recommendations for continued development

We have demonstrated the system's capability of achieving high measurement precision via the low standard deviation of δ across all zero-enrichment runs (± 0.38 ‰),) and in earlier sample runs (e.g., September 2, 2022 (1 SD = ± 0.135 ‰), Section 3.1). However, obstacles to achieving this level of precision reliably in measuring samples clearly persist.

Though already high, CO_2 removal efficiency by the contactor can be further increased by including a physical mechanism for mixing in the line upstream of the contactor and/or extending the length of the contactor membrane.

Engineering an improved setup for storage of reference material will improve measurement repeatability. Assuming the drift in the bagged seawater DIC arises from CO_2 exchange with the ambient atmosphere, drift could possibly be mitigated by placing the bags inside larger vessels of water of roughly equivalent DIC content. Alternatively, the bags could be used instead as bladders for glass bottles of seawater material;

removal of seawater from the bottle causes the bag to expand to fill the depleted headspace such that the seawater in the bottle has no exposure to ambient air.

Improving measurement repeatability likely also involves replacing the liquid handling pumps with a more stable liquid delivery system, such as one that relies on pressure gradients that are established via another means (e.g., upstream gas pressure or diaphragm). Like addressing the liquid flow stability, improving gas flow control can also increase stability in the CRDS signal.

To ensure full contact of seawater CO_2 with the membrane wall, rebuilding the contactor with a longer length of Teflon AF-2400 membrane may mitigate the issue of incomplete interfacing of CO_2 in the solution with the membrane.

Regarding samples with a very different pCO_2 from the reference material, the measurement repeatability may be improved by replacing the sample-reference switching hardware with hardware that lacks polymers, such as the glass capillary open split interface commonly used for sample and reference delivery to mass spectrometers. This change may also shorten the overall system response time. The feasibility of this option is not explored in this work.

Nevertheless, we have shown that this system is able to be calibrated and has potential to make high-precision measurements of DIC in seawater requiring limited sample volume and hands-on time.

Acknowledgements

Thank you to Guy Emanuele for your troubleshooting support and insights, Daniela Nestory for always agreeing to run alkalinity and salinity analyses, and George Anderson for ensuring I had access to the supplies I needed. A massive thank you is also owed to the members of the Scripps CO_2 and O_2 groups and Ross Beaudette for helping me through countless obstacles during the development of this method. Chapter 3 contains unpublished material coauthored with Keeling, R.F., Lueker, T.L., Paplawsky, W., Brooks, M., and Andersson, A.J. The dissertation author was the primary researcher and author of this paper.

References

Bandstra, L., Hales, B. and Takahashi, T.: High-frequency measurements of total CO_2: Method development and first oceanographic observations, Mar. Chem., 100(1–2), 24–38, doi:10.1016/J.MARCHEM.2005.10.009, 2006.

Bass, A. M., Bird, M. I., Morrison, M. J. and Gordon, J.: CADICA: Continuous Automated Dissolved Inorganic Carbon Analyzer with application to aquatic carbon cycle science, Limnol. Oceanogr. Methods, 10(1), 10–19, 2012a.

Bass, A. M., Bird, M. I., Munksgaard, N. C. and Wurster, C. M.: ISO-CADICA: Isotopic—continuous, automated dissolved inorganic carbon analyser, Rapid Commun. Mass Spectrom., 26(6), 639–644, 2012b.

Dickson, A. G., Afghan, J. D. and Anderson, G. C.: Reference materials for oceanic CO_2 analysis: a method for the certification of total alkalinity, Mar. Chem., 80(2–3), 185–197, 2003.

Dickson, A. G., Sabine, C. L. and Christian, J. R.: Guide to best practices for ocean CO_2 measurements., North Pacific Marine Science Organization., 2007.

Goyet, C. and Snover, A. K.: High-accuracy measurements of total dissolved inorganic carbon in the ocean: comparison of alternate detection methods, Mar. Chem., 44(2–4), 235–242, doi:10.1016/0304-4203(93)90205-3, 1993.

Huang, K., Cassar, N., Wanninkhof, R. and Bender, M.: An isotope dilution method for high-frequency measurements of dissolved inorganic carbon concentration in the surface ocean, Limnol. Oceanogr. Methods, 11(11), 572–583, 2013.

Johnson, K. M., Wills, K. D., Butler, D. B., Johnson, W. K. and Wong, C. S.: Coulometric total carbon dioxide analysis for marine studies: maximizing the performance of an automated gas extraction system and coulometric detector, Mar. Chem., 44(2–4), 167–187, doi:10.1016/0304-4203(93)90201-X, 1993.

Johnson, K. S.: Carbon dioxide hydration and dehydration kinetics in seawater, Limnol. Oceanogr., 27(5), 849–855, 1982.

Kaltin, S., Haraldsson, C. and Anderson, L. G.: A rapid method for determination of total dissolved inorganic carbon in seawater with high accuracy and precision, Mar. Chem., 96(1–2), 53–60, doi:10.1016/j.marchem.2004.10.005, 2005.

Karl, D. M. and Lukas, R.: The Hawaii Ocean Time-series (HOT) program: Background, rationale and field implementation, Deep. Res. Part II Top. Stud. Oceanogr., 43(2–3), 129–156, doi:10.1016/0967-0645(96)00005-7, 1996.

Keeling, C. D., Brix, H. and Gruber, N.: Seasonal and long-term dynamics of the upper ocean carbon cycle at Station ALOHA near Hawaii, Global Biogeochem. Cycles, 18(4), 2004.

Kouketsu, S., Murata, A. and Doi, T.: Decadal changes in dissolved inorganic carbon in the Pacific Ocean, Global Biogeochem. Cycles, 27(1), 65–76, doi:10.1029/2012GB004413, 2013.

Koweek, D. A., Dunbar, R. B., Monismith, S. G., Mucciarone, D. A., Woodson, C. B. and Samuel, L.: High-resolution physical and biogeochemical variability from a shallow back reef on Ofu, American Samoa: An end-member perspective, Coral Reefs, 34(3), 979–991, 2015.

Lang, S., Kazdal, T. J., Kühl, F. and Hampe, M. J.: Diffusion coefficients and VLE data of aqueous phosphoric acid, J. Chem. Thermodyn., 68, 75–81, 2014.

Li, Q., Wang, F., Wang, Z. A., Yuan, D., Dai, M., Chen, J., Dai, J. and Hoering, K. A.: Automated spectrophotometric analyzer for rapid single-point titration of seawater total alkalinity, Environ. Sci. Technol., 47(19), 11139–11146, doi:10.1021/es402421a, 2013.

Lueker, T. J., Keeling, C. D., Guenther, P. R., Wahlen, M. and Mook, W. G.: Inorganic Carbon Variations in Surface Ocean Water near Bermuda, 1998.

Michaels, A. F. and Knap, A. H.: Overview of the U.S. JGOFS Bermuda Atlantic Time-series study and the hydrostation S program, Deep. Res. Part II Top. Stud. Oceanogr., 43(2–3), 157–198, doi:10.1016/0967-0645(96)00004-5, 1996.

Park, E.-Y. and Choi, J.: The Performance of Low-Pressure Seawater as a CO_2 Solvent in Underwater Air-Independent Propulsion Systems, J. Mar. Sci. Eng., 8(1), 22, 2020.

Peng, T. H., Wanninkhof, R., Bullister, J. L., Feely, R. A. and Takahashi, T.: Quantification of decadal anthropogenic CO_2 uptake in the ocean based on dissolved inorganic carbon measurements, Nature, 396(6711), 560–563, doi:10.1038/25103, 1998.

Stoll, M. H. C., Bakker, K., Nobbe, G. H. and Haese, R. R.: Continuous-flow analysis of dissolved inorganic carbon content in seawater, Anal. Chem., 73(17), 4111–4116, doi:10.1021/ac010303r, 2001.

Zeebe, R. E. and Wolf-Gladrow, D.: CO_2 in seawater: equilibrium, kinetics, isotopes, Gulf Professional Publishing., 2001.